AN OPTIMIZED SUPERFERRIC WIGGLER DESIGN FOR THE INTERNATIONAL LINEAR COLLIDER DAMPING RINGS

A Dissertation

Presented to the Faculty of the Graduate School

of Cornell University

in Partial Fulfillment of the Requirements for the Degree of

Doctor of Philosophy

by

Jeremy Todd Urban

January 2007

AN OPTIMIZED SUPERFERRIC WIGGLER DESIGN FOR THE INTERNATIONAL LINEAR COLLIDER DAMPING RINGS

Jeremy Todd Urban, Ph.D.

Cornell University 2007

Experimental and simulation-based analyses of the superferric wigglers operating in the Cornell Electron Storage Ring (CESR) have provided significant practical experience with a wiggler-dominated accelerator. A modified version of the CESR wiggler will be discussed and shown to meet all physics performance specifications for the International Linear Collider (ILC) damping rings. Results from optimizations of the parameters of this wiggler will also be discussed and shown to both maintain the physics performance and additionally provide modifications that reduce the wiggler's cost and engineering risk. The conceptual design and simulated performance of the superferric ILC-optimized CESR-c (SIOC) wiggler will be presented, leading to a recommendation of the SIOC wiggler as the baseline ILC damping wiggler.

BIOGRAPHICAL SKETCH

Jeremy Todd Urban was born October 7th, 1980 in Woodbridge, Virginia to Russell and Gayle Urban, joining Sean and soon to be followed by Lance. With three boys in the house, physics lessons were learned early and often as objects in motion definitely stayed in motion and entropy always increased. Formally, physics study began for Jeremy at Woodbridge Senior High School in a combined junior year Physics I/AP Physics course. Informally, physics study began on the water with a lever and a fulcrum as a member of the Woodbridge Senior High School rowing team in the fall of 1993. Throughout his early exposure to physics, Jeremy enjoyed using physics to understand how the world worked and wanted to learn more about physics in college.

Jeremy graduated from Woodbridge Senior High School in 1998 after which he moved to Lewisburg, Pennsylvania to attend Bucknell University. There, his academic major was in physics, his academic minor was in mathematics, and his unofficial second major was in rowing. A deeper appreciation of physics was cultivated at Bucknell University thanks to excellent teachers who taught Jeremy about the elegance and complexity of physics and guided him into enlightening summer research opportunities at the Fermi National Accelerator Laboratory and the Indiana University Cyclotron Facility. These summers were Jeremy's first experiences with particle accelerators and with physics research. Intrigued with both, he was prompted to continue his study of accelerator physics and physics research in graduate school.

Jeremy graduated magna cum laude and Phi Beta Kappa from Bucknell University in 2002, and continued northward to Cornell University in Ithaca, New York. At Cornell University, Jeremy joined the accelerator physics group of the

Laboratory for Elementary Particle Physics in June of 2002 and participated in a number of interesting research projects and stimulating research collaborations which led to his completion of his Ph.D. in December 2006.

This dissertation is dedicated to my eternally supportive parents

who helped me to become the person that I am today,

and to the memory of Professor Joseph T. Rogers.

ACKNOWLEDGEMENTS

One of the things that I love about accelerator physics is that it is extremely collaborative. Thus, I have many people to thank!

First and foremost I would like to acknowledge the assistance and guidance of Gerry Dugan, my research advisor, without whom this research would not have culminated in a dissertation. Gerry taught me much about wigglers and the International Linear Collider during our collaborative and friendly discussions. In his high-level position within the international collaboration, Gerry afforded my research considerable exposure and attention which made me even more excited to achieve my results.

I would also like to thank the other members of my Ph.D. committee, Henry Tye and Dave Rubin, for guiding me through the trials and tribulations of earning a Ph.D. from Cornell University.

Joe Rogers was my research advisor for my first two years at Cornell. Though our time together was not long, he was an excellent advisor and friend. He will be remembered.

The physics community at Wilson Lab was an extremely valuable resource to me as a graduate student finding my way in accelerator research. David Sagan and Mark Palmer were extremely helpful every single time I came to either of them with a question. I would like to thank them for their patience, assistance, and friendship while I was at Cornell. Jim Crittenden deserves enormous thanks for his early and ongoing assistance with my wiggler simulations that contributed to my quick ramp-up time on this project and a rapid conclusion.

Other excellent minds at Wilson Lab that aided me and have my thanks are Georg Hoffstaetter, Maury Tigner, Lawrence Gibbons, Dave Rice, Bob Meller,

Sasha Temnykh, Mike Billing, Gerry Codner, Yulin Li, Eric Smith, and Karl Smolenski.

Rich Helms, Jeff Smith, and I were officemates for over four years which gave us lots of time for entertaining and stimulating discussions of particle accelerators, the field of physics, webpages, and whatever else we could think of to distract us from our work. I would like to thank them for taking time out of their research to help me with mine and for being my allies during the sometimes challenging journey that is graduate school.

I feel honored to have been a member of the truly international International Linear Collider collaboration and to have worked with the extremely skilled scientists who will make this machine a success. I would like to thank the dynamic team that taught me about linear collider physics on the beach in Santa Barbara: Nick Walker, Peter Tenenbaum, Andy Wolski, and Andrei Seryi.

As my wiggler research progressed, the International Linear Collider Damping Ring community gave me lots of valuable feedback and ideas for further avenues of research development. For that, I would like to thank Andy Wolski again (he cannot be thanked enough), Yunhai Cai, Marco Venturini, Alex Dragt, Chad Mitchell, Louis Emery, Aimin Xiao, Yukiyoshi Ohnishi, and all the rest of our damping ring group.

It was hard, but I did find time for the world outside of physics while at Cornell. For showing me a good time when I was not in the lab I would like to thank my friends Joe, Scott, Andy, Ben, Tom, and John. The Ithaca Dragon Boat Club also played an important role while I lived in Ithaca so they get acknowledged, even though without them I would have graduated six months earlier.

I would not have earned a Ph.D. in physics were it not for three specific per-

sonality traits. For fostering my affinity for hard work and my creative abilities I would like to thank my parents. For my competitive nature, all credit goes to my brothers–and my best friend Peter. For showing me how each of those traits are useful in physics I would like to thank all of the physics teachers I have ever had from Woodbridge High to Bucknell to Cornell, especially my friend and mentor at Bucknell, Sally Koutsoliotas.

Finally, I would like to thank Jennifer for her love and support, which manifested itself when I had to take a break from my research as well as when I could not.

TABLE OF CONTENTS

1 Introduction **1**
1.1 Outline 2

2 Particle Accelerator Physics **4**
2.1 The Elements Of Particle Accelerators 4
2.1.1 Magnets 5
2.1.2 Electromagnetic Cavities 8
2.2 What Are Particle Accelerators? 9
2.3 Technical View 10
2.3.1 Locating the Beam 11
2.3.2 Variable Definitions 12
2.4 Physics Examples 19
2.4.1 Radiation 19
2.4.2 Magnet Nonlinearities 24
2.4.3 Beam Interactions 25
2.5 Accelerators in Elementary Particle Physics 27

3 The International Linear Collider **31**
3.1 Overall Design 31
3.1.1 Energy and Particle Species 33
3.1.2 Why A Linear Machine? 33
3.1.3 Luminosity 35
3.2 Description of Operation 37
3.2.1 Operational Challenges 38
3.3 Principles of Design 40

4 The ILC Damping Rings **42**
4.1 Description of Operation 43
4.1.1 Challenges Arising From Collective Effects 44
4.1.2 Challenges Arising From The Bunch Compressor 45
4.1.3 Challenges Arising From The Main Linac 45
4.2 Acceptance 46
4.3 Damping Rates 47
4.4 The TESLA Damping Ring 50
4.5 The Baseline ILC Damping Ring 52
4.5.1 Further Research and Development Requirements 56

5 Wiggler Magnet Fundamentals **57**
5.1 What are Wigglers? 58
5.1.1 Particle Trajectory 59
5.1.2 Undulators and Wigglers 60
5.2 Wiggler Nonlinearities 62

5.2.1 Idealized Nonlinearities 62
5.2.2 Realistic Nonlinearities 66
5.3 Uses in Damping Rings 70
5.4 Wiggler Simulation Techniques 73
5.4.1 Particle Tracking 74
5.4.2 Generating the Magnetic Field 77
5.4.3 Fitting the Magnetic Field 79
5.4.4 Dynamic Aperture and Frequency Map Simulations 82

6 Existing Wiggler Designs **88**
6.1 TESLA Permanent Magnet Wiggler 88
6.1.1 Principles of Design 89
6.1.2 Simulated Performance in ILC 91
6.1.3 TESLA Wiggler Conclusions 94
6.2 CESR-c Superferric Wiggler 95
6.2.1 Principles of Design 98
6.2.2 Experimental Performance in CESR 101
6.2.3 Simulated Performance in ILC 105
6.2.4 CESR-c Wiggler Conclusions 110
6.3 ILC Wiggler Technology Decision 110
6.4 Baseline ILC Damping Ring 112

7 ILC-Optimized Wiggler Design **116**
7.1 Optimization Goals 116
7.2 Motivation 117
7.2.1 Construction 118
7.2.2 Radiation Load 119
7.2.3 Vacuum Chamber 120
7.2.4 Cryogenics 120
7.3 Optimization Methods 122
7.3.1 Details of the Magnet Model 122
7.4 Pole Width 124
7.5 Pole Gap 126
7.6 Peak Field and Length 128
7.7 Magnet Period 131
7.8 Optimization Conclusions 135

8 ILC-Optimized Wiggler Performance **137**
8.1 Dynamic Aperture 138
8.2 Frequency Map Analysis 141
8.3 Multipole Field Errors 144
8.4 Performance Conclusions 146
8.5 Next Steps 148

9 Conclusions **150**
9.1 The ILC Damping Wiggler . . . 150
9.2 The ILC-Optimized Wiggler . . . 151
9.3 Recommendations . . . 152

A Wiggler Field-Fitting Benchmark **154**

B Damping Ring Configuration Study **160**

Bibliography **172**

LIST OF TABLES

2.1 Magnet multipoles and their effect on the motion of the beam . . . 5

3.1 Parameters in the ILC 32
3.2 Beam parameters in the SLC and ILC 33

4.1 Target emittance values in the ILC 43
4.2 Target beam parameters of the ILC damping ring 44
4.3 Target beam parameters of the TESLA damping ring 51
4.4 The ILC damping ring configuration study lattices 53
4.5 Target beam parameters of the baseline ILC damping ring 55

6.1 Parameters of the TESLA wiggler 90
6.2 TESLA lattice parameters using the TESLA wiggler 94
6.3 Parameters of the CESR-c wiggler 96
6.4 Parameters of the modified CESR-c wiggler 107
6.5 TESLA lattice parameters using the modified CESR-c wiggler . . . 109
6.6 OCS v2.0 lattice parameters using the modified CESR-c wiggler . . 113

7.1 Required currents for the pole gap optimization 128
7.2 Target beam parameters of the ILC damping ring 129
7.3 Resulting lattice parameters for the peak field and length optimization 130
7.4 Resulting lattice parameters for the period optimization 133
7.5 Parameters of the superferric ILC-optimized CESR-c wiggler . . . 135

8.1 OCS v2.0 lattice parameters using the superferric ILC-optimized CESR-c wiggler 137

9.1 Summary of parameters of the candidate ILC wigglers 152

LIST OF FIGURES

2.1 Net horizontal and vertical focusing magnet cell 7
2.2 The local reference system in the particle accelerator 11
2.3 Illustration of the beam size 13
2.4 Tune plane resonances 15
2.5 Illustration of the beam emittance 17
2.6 Illustration of the physical and dynamic apertures 18
2.7 Diagram of radiation damping 22

3.1 Site layout of the International Linear Collider 31
3.2 Components of a basic linear collider 37

4.1 Damping the beam to equilibrium 48
4.2 Site layout of the TESLA damping ring 50
4.3 Dynamic aperture of the TESLA damping ring 52
4.4 Site layout of the baseline ILC damping ring 54

5.1 A wiggler magnet 59
5.2 Illustration of inherent vertical wiggler nonlinearity 63
5.3 Vertical nonlinearities with vertical beam position 66
5.4 Vertical nonlinearities with wiggler period 67
5.5 Quadratic roll-off of vertical wiggler field 68
5.6 Horizontal nonlinearities with horizontal beam position 69
5.7 Horizontal nonlinearities with pole width 70
5.8 Comparison of wiggler tracking models 78
5.9 Wiggler poles in Radia 79
5.10 Wiggler field fit residuals 82

6.1 The TESLA wiggler 89
6.2 Magnetic field of the TESLA wiggler 90
6.3 Dynamic aperture of the TESLA wiggler in the TESLA ring 92
6.4 Frequency map analysis of the TESLA wiggler in the TESLA ring 93
6.5 The CESR-c wiggler 97
6.6 End poles of the CESR-c wiggler 97
6.7 Magnetic field of the CESR-c wiggler 98
6.8 Magnetic field deviation of the CESR-c wiggler 99
6.9 Support structure of the CESR-c wiggler 100
6.10 Coil curvature and pole cutouts of the CESR-c wiggler 101
6.11 Experimental CESR-c wiggler tune shifts 1 104
6.12 Experimental CESR-c wiggler tune shifts 2 104
6.13 Field roll-off of the TESLA and CESR-c wigglers 106
6.14 Magnetic field and trajectory of the modified CESR-c wiggler . . . 107
6.15 Dynamic aperture of the modified CESR-c wiggler in the TESLA ring 108

6.16 Frequency map analysis of the modified CESR-c wiggler in the TESLA ring . . . 108
6.17 Dynamic aperture of the modified CESR-c wiggler in the OCS ring 111
6.18 Dynamic aperture of the modified CESR-c wiggler in later versions of the OCS ring . . . 114
6.19 Dynamic aperture, with multipole field errors, of the modified CESR-c wiggler in later versions of the OCS ring . . . 115

7.1 Variation of field roll-off with pole width . . . 124
7.2 Wiggler optimization: pole width 1 . . . 125
7.3 Wiggler optimization: pole width 2 . . . 126
7.4 Variation of field roll-off with pole gap . . . 127
7.5 Wiggler optimization: pole gap . . . 127
7.6 Wiggler optimization: peak field and length . . . 130
7.7 Wiggler optimization: period 1 . . . 132
7.8 Wiggler optimization: period 2 . . . 132
7.9 Wiggler optimization: period 3 . . . 133

8.1 Dynamic aperture results for the SIOC wiggler . . . 139
8.2 Off-energy dynamic aperture results for full nonlinear SIOC wiggler model . . . 140
8.3 Energy aperture results for the SIOC wiggler . . . 140
8.4 Tune shift versus amplitude results for the SIOC wiggler . . . 141
8.5a Frequency map analysis result in tune-space for linear SIOC wiggler model . . . 142
8.5b Frequency map analysis result in physical-space for linear SIOC wiggler model . . . 143
8.6a Frequency map analysis result in tune-space for ideal nonlinear SIOC wiggler model . . . 144
8.6b Frequency map analysis result in physical-space for ideal nonlinear SIOC wiggler model . . . 145
8.7a Frequency map analysis result in tune-space for full nonlinear SIOC wiggler model . . . 146
8.7b Frequency map analysis result in physical-space for full nonlinear SIOC wiggler model . . . 147
8.8 Dynamic aperture results, with multipole field errors, for the SIOC wiggler . . . 147
8.9 Off-energy dynamic aperture results, with multipole field errors, for the SIOC wiggler . . . 148

A.1 Wiggler benchmarking study: single-mode Taylor map . . . 156
A.2 Wiggler benchmarking study: multi-mode Taylor map . . . 158
A.3 Wiggler benchmarking study: multi-mode dynamic aperture . . . 159

B.1a Damping ring configuration study: dynamic aperture 1 . . . 162

B.1b Damping ring configuration study: dynamic aperture 2 163
B.2a Damping ring configuration study: dynamic aperture with multipole field errors 1 164
B.2b Damping ring configuration study: dynamic aperture with multipole field errors 2 165
B.3a Damping ring configuration study: dynamic aperture with multipole field errors 3 166
B.3b Damping ring configuration study: dynamic aperture with multipole field errors 4 167
B.4a Damping ring configuration study: frequency map analysis 1 168
B.4b Damping ring configuration study: frequency map analysis 2 169
B.5a Damping ring configuration study: frequency map analysis 3 170
B.5b Damping ring configuration study: frequency map analysis 4 171

Chapter 1

Introduction

The International Linear Collider is a proposed energy frontier particle accelerator that will further the world's understanding of the fundamental nature of space, time, matter, and energy. The International Linear Collider (ILC) will unlock these secrets through collisions of bunches containing billions of electrons and positrons, at energies between 500 and 1,000 GeV, over 14,000 times per second. The potential for this machine to reveal new elementary particles, fundamental forces, or even entirely new paradigms of physics is great. However, the challenge of designing and operating this 500 GeV electron-positron collider is perhaps greater still.

The challenge of the ILC lies in its shape. The ILC will be a straight-line collider which presents obstacles to its design and operation that have not existed for the predominantly circular colliders built thus far. One clear design requirement unique to the ILC is to identify where there is room for a 25-mile straight-line particle accelerator.

Even before the site of the ILC is chosen, physicists will be faced with many more important questions, including, "How can we maximize our chances of finding new particles or forces with this accelerator?" Finding new particles or forces with the ILC will require getting individual electrons and positrons to collide and the probability of doing this is increased by squeezing the electron and positron beams tightly. Thus, the answer to increasing the chances of finding new physics lies in squeezing, or damping, the particle beams as tightly as possible, and this is where the damping rings enter the ILC.

The damping rings are circular accelerators through which the electrons and positrons travel before being accelerated by the straight-line accelerator which gives the linear collider its name. As the electrons and positrons circulate in the damping rings they emit synchrotron radiation which takes energy away from the beam causing the beam to be damped down to the desired smaller size. Unfortunately, the radiation emission inherent with a circular accelerator can be slow and as a result, the beams have to circulate in the damping ring for thousands of turns before the beams will be damped to a small enough size. To minimize this delay, the International Linear Collider will use dedicated accelerator components to speed along the radiation emission process.

The primary accelerator component used for speeding up synchrotron radiation production in the damping rings is the wiggler magnet. Unfortunately, wiggler magnets present their own challenges to the operation of the ILC damping rings. Wigglers produce very strong and rapidly alternating magnetic fields which can disrupt stable beam trajectories. The interplay between the wiggler's beneficial synchrotron radiation production and its damaging impact on the beam trajectory means that wigglers must be precisely designed to work best in the ILC, which leads to the motivation for this dissertation.

1.1 Outline

This dissertation begins with a description of the International Linear Collider's operation to further motivate the need for damping wigglers. The physics principles of a wiggler magnet will be explained along with the challenges it presents to the successful operation of the damping rings.

The conceptual design of an optimized International Linear Collider damping wiggler will be derived through the combination of a proposed permanent magnet wiggler and an existing superconducting magnet wiggler. This dissertation concludes with the results, achieved through computer simulations, of the optimized damping wiggler's successful operation in the International Linear Collider damping ring.

Chapter 2

Particle Accelerator Physics

Particle accelerators are scientific instruments used by a variety of scientists including physicists, chemists, biologists, and engineers, for a number of different purposes including producing new particles, studying radiation effects, probing elemental composition, and killing malignant cells. Despite their wide range of application, all particle accelerators serve the same fundamental purpose of accelerating beams of charged particles to a higher energy. How high an energy the accelerator should achieve or the type of particle that should be accelerated are questions that depend on an accelerator's specific application, but the basic goal of bringing a large number of very small particles to a higher energy is the same in all accelerators.

2.1 The Elements Of Particle Accelerators

Particle accelerators range in size from meters to kilometers and include table-top devices as well as some of the largest and most complex electromechanical devices ever created. At their core, particle accelerators consist of a sequence of electromagnetic devices through which a beam of charged particles passes. These individual electromagnetic devices are designed to accelerate the particle beam to a desired energy, or range of energies, while steering it in the direction it needs to go in as tight a package as the application requires.

There are many different types of electromagnetic devices in particle accelerators, but the forces they exert on the particle beam are all given by the Lorentz

Table 2.1: Magnet multipoles and their effect on the motion of the beam.

Multipole	$\mathbf{B_y(x, y = 0)} \propto$	**Effect**
Dipole	B_1	Steering
Quadrupole	$B_2 \cdot x$	Focusing
Sextupole	$B_3 \cdot x^2$	Energy-dependent compensation
Octupole	$B_4 \cdot x^3$	Field error compensation

force law:

$$\mathbf{F} = q(\mathbf{E} + \mathbf{v} \times \mathbf{B}), \tag{2.1}$$

where $\mathbf{F}$ is the force on the particle, q and $\mathbf{v}$ are the charge and velocity of the particle, and $\mathbf{E}$ and $\mathbf{B}$ are the electric and magnetic fields from the given electromagnetic device. Given a source of $\mathbf{E}$ and $\mathbf{B}$ fields, charged particles will experience a force that will guide them on a specific path through the particle accelerator. To determine the trajectory of this path and whether or not it will lead to a useful beam, the shape and strength of the electromagnetic guide fields must be understood. In a particle accelerator, the two most common sources of guide fields are magnets and electromagnetic cavities.

2.1.1 Magnets

Magnets are critical components of particle accelerators as their magnetic fields are what steer the charged particles through the accelerator. Depending on the number of poles that make up the magnet, the shape of the magnetic field can be altered to steer the particles in different ways (see Table 2.1).

Dipole Magnets

Dipole magnets consist of just two poles, a north pole and a south pole that are placed above and below the center of the particle path. This configuration of magnetic poles produces a vertical magnetic field that is uniform over the region of the beam and will bend the particle beam horizontally. For relativistic particles, this bend in trajectory has a radius equal to:

$$R = \rho = \frac{E}{qcB}, \tag{2.2}$$

where E is the particle's energy, c is the speed of light, and B is the strength of the uniform dipole field. Thus, the energy of the beam and strength of the dipoles set the circumference of a circular particle accelerator.

Quadrupole Magnets

A quadrupole magnet possesses two north poles and two south poles arranged in equally spaced pairs around the center of the particle path and produces a magnetic field that depends on position. The magnetic field of a quadrupole magnet is shaped in such a way that it exerts a restoring force on particles that are offset from center. Particles above center will be pushed downwards and particles below center will move upwards, back to the center of the magnetic field. Thus, quadrupole magnets are used to focus the beam of particles into tight bunches.

This description is slightly complicated by the fact that a quadrupole can only focus in one plane at a time. With no current or electric field in the center of the quadrupole field-region, Maxwell's equations require that the curl of the magnetic field be zero, $\nabla \times \mathbf{B} = 0$. So a quadrupole whose field lines are arranged to steer a vertically offset particle back to center automatically has field lines which steer

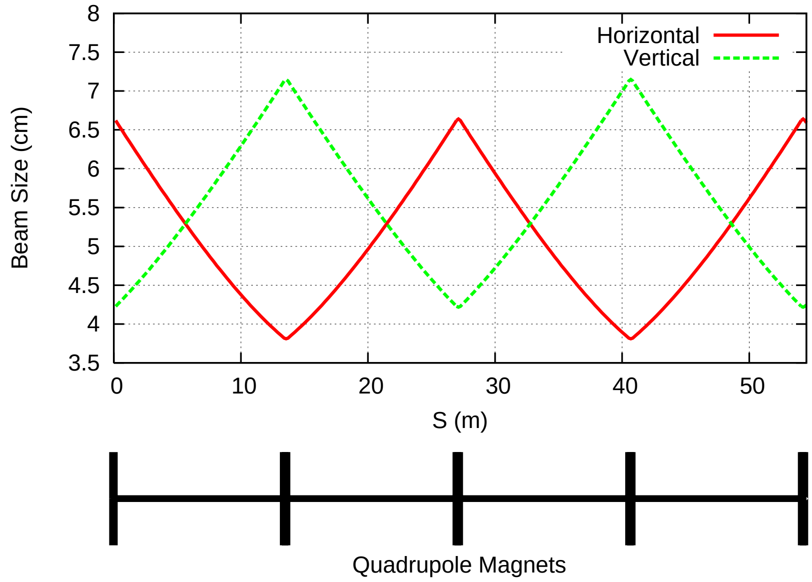

Figure 2.1: Net horizontal and vertical focusing produced by a series of alternating focusing and defocusing quadrupole magnets. In this example, the beam size was calculated using $\epsilon_{x,y} = 1\,\mathrm{m} \cdot \mathrm{rad}$ for a lattice with $\beta_{x,max} = 44\,\mathrm{m}$ and $\beta_{y,max} = 51\,\mathrm{m}$.

a horizontally offset particle away from center.

To overcome this limitation, the fields of more than one quadrupole magnet are combined to produce a focusing force in both planes. As with the combination of a convex and concave lens in optics, a vertically-focusing/horizontally-defocusing quadrupole can be combined with a vertically-defocusing/horizontally-focusing quadrupole (rotated 90° relative to the first) to produce a net focusing force in both planes (see Figure 2.1). This effect is called strong-focusing and is utilized in the majority of current day particle accelerators.

Higher Order Magnets

Magnets with more than four poles are also common in accelerators. Sextupole magnets have three north-pole/south-pole pairs and produce fields that depend on the square of the particle's displacement from the center of the guide field. This results in fields that change with horizontal and vertical position in the magnet, coupling the horizontal and vertical motion of the beam. Additionally, sextupole focusing can be used in combination with quadrupole focusing to modify the focusing of the beam based on its energy. The particles in an accelerator can have a range of energies and this can cause the quadrupoles to focus each particle by a different amount. If sextupoles are placed in a region of the accelerator where the particle trajectories depend on energy, then they will produce the precise amount of focusing on the beam to counteract the energy dependent focusing of the quadrupoles; therefore sextupoles are commonly found adjacent to quadrupoles to provide this compensation.

Octupoles have four magnet pairs and produce fields that depend on the cube of the particle's displacement, thus the strength of octupole-focusing does not grow linearly with the particle's amplitude. Particles at different amplitudes will be strongly focused or defocused by an octupole and cannot be directly refocused with extra quadrupoles. The usefulness of octupoles comes when errors in the construction of the hundreds of quadrupoles in an accelerator produce fields with octupole-like dependencies and a few octupole magnets can be used to correct these undesirable field errors.

2.1.2 Electromagnetic Cavities

Like magnets, electromagnetic cavities are critical in particle accelerators, as their electric fields are what accelerate the charged particles. Electromagnetic cavities are metal structures that the beam travels through and which, when struck with electromagnetic energy, produce oscillating electric and magnetic fields. The cavities are shaped in such a way that the dominant mode of oscillation produces an electric field which is longitudinal and peaks on the centerline of the accelerator, thus producing a field which will accelerate the beam of particles.

Since the accelerating fields are oscillating, particles will receive a different gain in energy depending on the phase of the electromagnetic oscillation as they move through the cavity. The energy gain of a particle from one cavity is given by:

$$\Delta E = qV_{max}\sin(\Psi_0), \tag{2.3}$$

where V_{max} is the maximum voltage of the cavity and Ψ_0 is the phase of the field oscillation when the particle passes through the cavity. The field oscillates at radio frequencies so that it can be precisely timed to optimally accelerate each group of particles every time they pass through the cavity; thus, these electromagnetic cavities are called RF cavities.

2.2 What Are Particle Accelerators?

The simplest example of a particle accelerator is a single RF cavity that accelerates a group of particles to a higher energy. However, the particles would not be in a useful state after passing through just one RF cavity. One problem is that the group of particles would be diffuse and would grow more as it drifts beyond the RF cavity. To solve this problem, a pair of focusing and defocusing quadrupoles can be combined with the RF cavity to form a cell. This cell accepts a beam of particles and outputs it at a higher energy and with a tighter focus than initially accepted.

However, a particle accelerator made of just one RF cavity and two quadrupoles is still not very useful because experimental physicists frequently want much higher energies than the field that just one RF cavity can provide. To overcome this challenge either more RF cavities can be used or the beam can pass through the single RF cavity multiple times. Both of these solutions are commonly used; the first is called a linear accelerator and the second is called a circular accelerator.

A linear accelerator, or linac, is a sequence of accelerating cavities and focusing magnet cells that the beam passes all the way through once. This sequence of cells is called a lattice. The beam exits such a linac lattice tightly focused and at an energy proportional to the number of RF cavities. In a circular accelerator, or ring, the beam revolves around the lattice many times, traveling through a repeating sequence of dipoles, focusing and defocusing quadrupoles, and accelerating cavities. A circular accelerator is essentially a linear accelerator with enough dipoles to bend the end of the accelerator back around to its front so that the beam can pass through the cavities repeatedly, gaining energy each time.

2.3 Technical View

In either a linear or a circular accelerator, individual particles travel through the lattice in grouped bunches that follow each other, one after another, in a train of bunches. A sequence of bunch trains forms a beam of high energy particles.

A particle accelerator is designed to control the bulk behavior of the beam. For example, quadrupoles keep the overall size and spread of the particle beam small by limiting the maximum amplitude of particle trajectories. This allows accelerator operators to not worry about the exact trajectory an individual particle takes through the lattice. In this way, the behavior of individual particles in the accelerator is averaged over and the entire ensemble of particles is described by the beam's average position, momentum, and energy.

The energy and momentum of each of the particles are averaged to give the

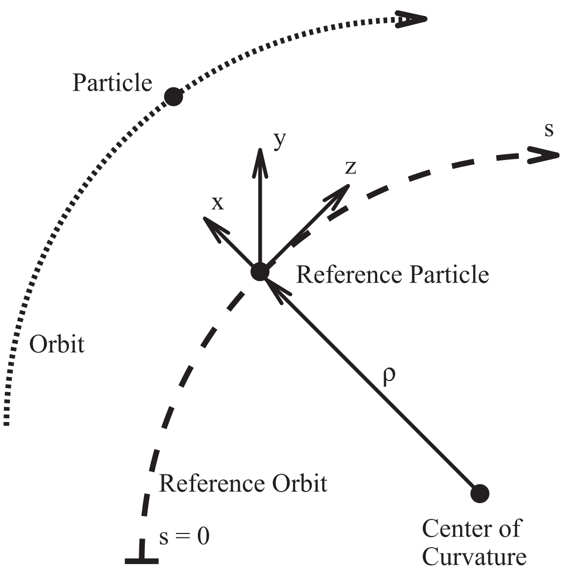

Figure 2.2: The local reference system in the particle accelerator. Particle positions are given as displacements from a reference particle at the center of the guide fields.

beam's average energy and momentum, E_0 and P_0. The average position of the particles in the beam is represented by a reference particle, which for many accelerators remains horizontally and vertically centered in the field region. The longitudinal position of the reference particle is given by s, which is zero at the start of the lattice and increases in the direction of particle motion (see Figure 2.2).

2.3.1 Locating the Beam

When analyzing the dynamical performance of an accelerator the local position of a particle needs to be known in order to determine its exact trajectory through the magnets and cavities. The local coordinates of a particle are measured relative to the reference particle in the center of the bunch. As seen in Figure 2.2, horizontally, x increases at larger radii in a ring; vertically, y increases upward from center; and longitudinally, z increases as particles move ahead of the center of the bunch, in the direction of increasing s.

As the beam moves around the accelerator, in addition to the position of circulating particles changing, their angle of trajectory changes as well. The horizontal and vertical angle of the trajectory is equal to the slope of the particle's path relative to the beam direction, $x' = dx/ds$ and $y' = dy/ds$. When the particle is traveling at the speed of light in the direction of increasing s, these transverse angles are very small and can be approximated by the ratio of the component momentum in that direction, $P_{x,y}$, to the average beam momentum, P_0. This ratio, $p_{x,y} = P_{x,y}/P_0$ in radians, is another useful way to describe the motion of individual particles in the accelerator.

The position and angle of a particle's trajectory is determined by the lattice of electric and magnetic elements in an accelerator. The forces these elements exert on the beam produce an oscillating trajectory, known as a betatron oscillation, around the reference orbit that can be represented by:

$$\begin{aligned} x(s) &= C\sqrt{\beta(s)}\cos\left(\psi(s)+\phi\right) \\ x'(s) &= -\frac{C}{\sqrt{\beta(s)}}[\alpha(s)\cos\left(\psi(s)+\phi\right)+\sin\left(\psi(s)+\phi\right)]. \end{aligned} \tag{2.4}$$

In these equations, the horizontal position and angle at a given s-coordinate are given by an amplitude, C, and phase, ϕ, that are specified by the particle's initial conditions, and by amplitude and phase functions, α, β, and ψ, that depend on the strength of the magnets in the accelerator and vary around the lattice.

2.3.2 Variable Definitions

When the trajectories of individual particles are averaged over, the total size of the particle beam is an important characteristic. The difference between the maximum and minimum position particles in each dimension gives the horizontal, vertical,

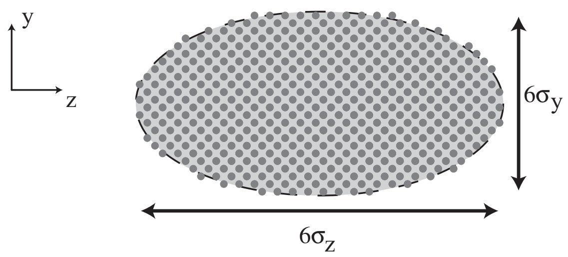

Figure 2.3: The physical size of the charged particle bunch in the vertical and longitudinal planes is $6\,\sigma_y$ and $6\,\sigma_z$.

and longitudinal sizes of the beam. If the particles are arranged in a Gaussian distribution in space, the beam size, or σ, corresponds to one standard deviation of the statistical distribution of particles in each dimension. For example, if the particles are in a Gaussian distribution longitudinally, then the total length of the beam–the size which includes 99.7 % of the particles–is $6{\times}\sigma_z$ (see Figure 2.3). The beam σ's depend on the β-function and therefore vary around the ring depending on the strength of the quadrupoles.

If we look at the σ's not around the lattice, but at a single s position, we will see that a well behaved beam has reached equilibrium and the beam distribution does not change from one revolution, or turn, in a circular accelerator to the next. In this equilibrium case, the beam in an electron accelerator can be well approximated with a Gaussian distribution of particles in position and angle in each dimension. A Gaussian beam is thus well described by its beam sizes.

Energy Spread

The beam's spread in energy is another important beam parameter and is considered specifically here. The beam has a certain average energy, E_0, but the individual electrons that make up the beam are free to move independently. Depending on a particle's z coordinate, it will be at a different longitudinal position in the beam when it reaches the RF cavities than another particle,a particle will therefore arrive at a different phase of the accelerating wave than another particle. From Equation 2.3 it is clear that particles will gain a different amount of energy based on their distance from the center of the beam. Thus, the energy of each particle in the beam is slightly different from E_0 by ΔE allowing particles to be described by their fractional energy deviation, $\delta = \Delta E/E_0$. The distribution of energy deviations in the beam forms a spread in the total beam energy given by σ_δ.

Tunes

The change in phase of the betatron oscillation is another way that the bulk beam behavior is described in a circular accelerator. The difference in the betatron phase over one complete ring revolution is called the tune of an accelerator and is given by Q, where:

$$Q = \frac{\Delta\psi}{2\pi} = \frac{\psi(s+L) - \psi(s)}{2\pi}. \tag{2.5}$$

The tune gives the number of betatron oscillations a particle undergoes per revolution. In the transverse dimension these are called the betatron tunes, horizontal, Q_x, and vertical, Q_y, and longitudinally this is the synchrotron tune, Q_s. The betatron and synchrotron tunes are determined by the strength of the magnets and the cavities, which are set so that the accelerator will operate at a specific set of tunes that is called the ring's called the operating point

If the operating tunes of an accelerator are not chosen carefully, magnetic field errors can create a resonant build-up in the betatron oscillation that leads to particles loss. The simplest example of this resonance condition is if $Q_x = 1$, in this case a particle could experience a magnetic field error at the same betatron phase

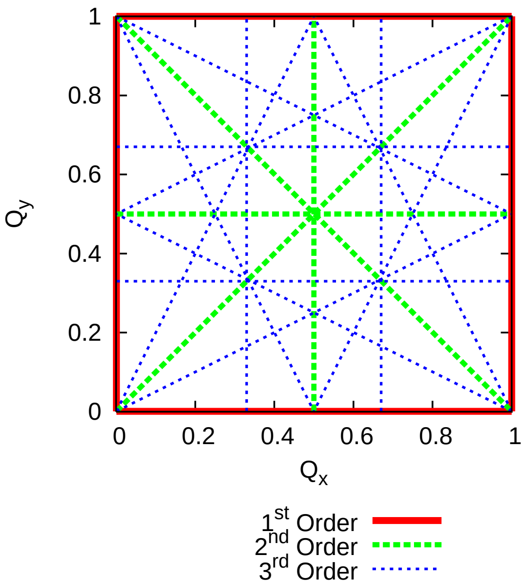

Figure 2.4: Tune plane with the 1st, 2nd, and 3rd order coupled transverse tune resonance lines shown.

on every turn. The kick corresponding to that field error would be in the same direction and would grow with each successive turn until the particle amplitude is large enough to hit an aperture and be lost [1]. Horizontally and vertically coupled resonances also exist between the betatron tunes if

$$mQ_x + nQ_y = p, \tag{2.6}$$

where m, n, and p are all integers. The strength of the tune resonances are given by the order which equals $|m| + |n|$.

Plotting the horizontal against the vertical tune gives a plane of possible operating conditions for the accelerator. In this tune plane, the coupled resonances are shown as intersecting lines of potentially damaging accelerator performance that accelerator operators learn to avoid (Figure 2.4).

Emittance

To gain further information about the distribution of particles in the beam, the position of every particle can be plotted in position-angle phase space. In phase space, the area of the particle distribution is an invariant in a conservative system and is called the beam emittance, ϵ, given by:

$$\epsilon_x = \sqrt{\langle x^2 \rangle \langle x'^2 \rangle - \langle xx' \rangle^2}. \tag{2.7}$$

The position and angle of individual particles change around the accelerator, but only in such a way that the area of the entire distribution is conserved. The emittance of the beam is defined for each dimension (for example plotting the horizontal position of each particle against its horizontal angle gives the horizontal emittance, or ϵ_x, see Figure 2.5). The emittance of the beam can change over time, but only through non-Hamiltonian processes, processes that add or remove energy. Non-Hamiltonian processes that the beam can undergo, resulting in an increase or decrease in emittance, include acceleration, radiation, and hitting a target or wall.

Acceleration is ubiquitous in particle accelerators, so the fact that an accelerating beam has a constantly changing emittance makes characterizing a beam based on its emittance less useful. To overcome this, a new variable is introduced, the normalized emittance, which is equal to $\gamma \times \epsilon$. Here, γ is the relativistic factor given by:

$$\gamma = \frac{1}{\sqrt{1 - \frac{v^2}{c^2}}}. \tag{2.8}$$

The normalized emittance is the normally defined emittance multiplied by γ which depends on the beam energy in the same way that the emittance does. Thus, as a particle beam is accelerated, its emittance (ϵ) decreases by a factor of γ, but its

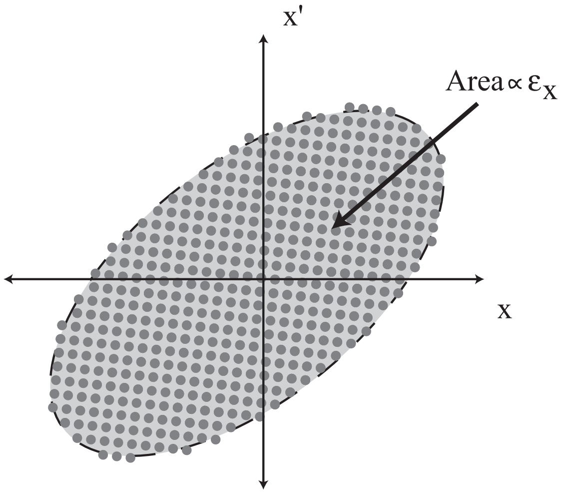

Figure 2.5: The horizontal beam emittance is related to the area the beam occupies in horizontal position-momentum phase space.

normalized emittance ($\gamma\epsilon$) remains constant.

Physical and Dynamic Apertures

As the beam of charged particles moves through a lattice of electric and magnetic elements, it is contained in a metal pipe, called the beam pipe. The beam pipe goes around the whole circumference of the ring or down the entire length of the linac and has a transverse opening on the order of a few inches. If an accelerated particle grows to a large enough amplitude to come in contact with the beam pipe (for example, when it hits a tune resonance), it will be scattered by the atoms in the metal pipe and become lost from the accelerated beam.

Thus, the physical beam pipe sets a limit on the maximum amplitude of a surviving particle and is called the physical aperture of an accelerator (see Figure 2.6). The physical aperture is typically smallest in sections of the lattice where the source of the magnetic or electric field needs to be very close to the center of the beam pipe and therefore, the beam pipe has to be very narrow. The physical

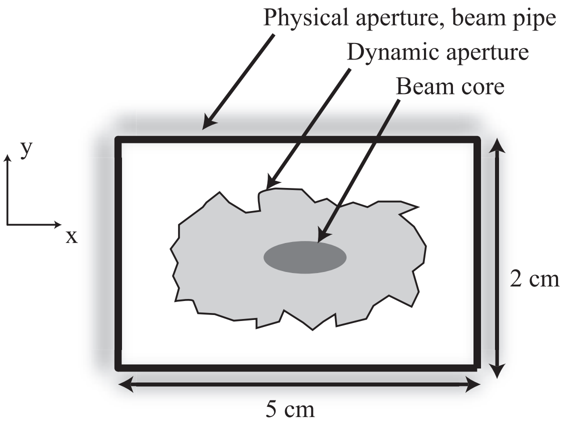

Figure 2.6: The physical and dynamic apertures. Particle trajectories are stable inside the dynamic aperture (the gray region) and unstable outside (the white region). A particle is lost when it hits the beam pipe.

aperture can also narrow around collimators which are located inside the beam pipe in order to protect sensitive magnets from intense radiation damage (see Section 2.4.1). It is these aperture-limiting locations in the ring which define the physical aperture and set the maximum beam sizes and emittances that can be safely accelerated without losing any particles.

The physical aperture is the actual point of beam loss in the accelerator but, in reality, particles traveling at smaller amplitudes cross a non-physical boundary where they start to grow uncontrollably until they hit the physical aperture. The boundary between a stable, stored particle trajectory and an unstable one that will grow very fast and be lost defines the dynamic aperture of the accelerator (see Figure 2.6). The dynamic aperture typically is a poorly defined, jagged boundary determined by the combination of all of the position-dependent magnetic field errors in the ring, which can resonate with the tune of the beam and drive particles to larger and larger amplitudes depending on their initial positions.

2.4 Physics Examples

Depending on its regime of operation, different physics phenomena dominate the performance of a particle accelerator at different times. When a realistic treatment of the physics is included, a beam's emittance can grow or shrink, its tune can vary, the beam can blow up and be lost on the physical aperture, or any number of other productive or unproductive results can occur. Three specific physics phenomena present in a typical particle accelerator are given below in an attempt, not to complicate the discussion, but to examine particle accelerators in a realistic manner.

2.4.1 Radiation

When charged particles accelerate they radiate, and particles bending through a circular accelerator are continuously accelerating and thus radiating. The emission of radiation from circulating particles was discovered at a synchrotron accelerator and because of this it is called synchrotron radiation. Synchrotron radiation comes in a range of frequencies from x-rays to infrared and can be useful for scientists performing x-ray crystallography or using other beam-imaging techniques. In fact, some circular accelerators are dedicated to the production of synchrotron radiation for use by physicists, chemists, biologists, and materials scientists; these accelerators are called light sources [1].

For other types of circular accelerators, synchrotron radiation can be a nuisance, as the emitted photons take away some of the beam's energy and momentum. The total beam energy lost due to radiation in one turn is determined by the energy of the beam and the strength of the magnetic field doing the bending. This can be combined to give [2]:

$$U_0 = \frac{q^2c^2}{2\pi} C_\gamma E_0^2 \oint B^2(s)\, ds, \tag{2.9}$$

the total beam energy radiated in one turn, where $C_\gamma = 8.8460 \times 10^{-5}\,\mathrm{m} \cdot \mathrm{GeV}^{-3}$, E_0 is the energy of the beam, and the magnetic field, B depends on s and must be integrated around the whole lattice. Plugging equation 2.2 into this expression gives:

$$U_0 = \frac{C_\gamma}{2\pi} E_0^4 I_2, \tag{2.10}$$

where:

$$I_2 = \oint \frac{1}{\rho^2}\, ds. \tag{2.11}$$

The radiated energy loss is cast in this form to pull out the variable I_2 which is the second of five integrals of fundamental lattice parameters, such as the bending radius, that can be used to describe the important impacts synchrotron radiation has on the beam. Thus, by increasing the energy of the beam, increasing the strength of the dipoles, or equivalently reducing the circumference of the accelerator, more energy is lost per turn. However, the effects of synchrotron radiation are more than simply lowering the energy of the particle beam, and it is these effects which will be discussed further.

Quantum Excitation

Another consequence of synchrotron radiation comes from the fact that photons are quantum mechanical entities. The timing and energy of emitted photons is random, so each particle loses a slightly different amount of energy when it radiates. Since the magnets in accelerators produce different forces for particles at different energies, the trajectory of a particle through an accelerator depends on its energy. The dispersion of the accelerator measures the energy dependent nature of the trajectory, so a region with zero dispersion produces the same trajectory for particles of all energies. The biggest source of dispersion in accelerators is the large number of horizontal dipole magnets which bend particles through an angle that depends on their energies.

If synchrotron radiation is emitted in a region of the accelerator where the dispersion is non-zero, then the trajectory of the beam will change after the emission of radiation. Horizontal dispersion coming from the bending magnets can result in the horizontal beam size, horizontal emittance, and energy spread increasing after the emission of radiation from the entire distribution of particles. Because of the quantum generated growth of the beam emittance, this phenomenon is called quantum excitation and has a larger effect when the radiation is emitted in a region of the accelerator with significant dispersion [3].

Since the bending magnets in accelerators are typically only horizontal, quantum excitation affects the vertical dimension at a much smaller level. Excitation of the vertical emittance comes from the fact that the radiation emitted by an electron as it bends through the horizontal plane is emitted into the vertical plane as well. This is because radiation is emitted into a cone that points in the forward direction and opens into the x and y-planes with an opening angle of $1/\gamma$. This quantum mechanically driven process sets the minimum vertical emittance achievable, but this minimum is extremely small and often can be taken as essentially zero.

Radiation Damping

Since the goal of a particle accelerator is to raise the beam to a desired energy, the energy lost to synchrotron radiation will have to be restored with the RF

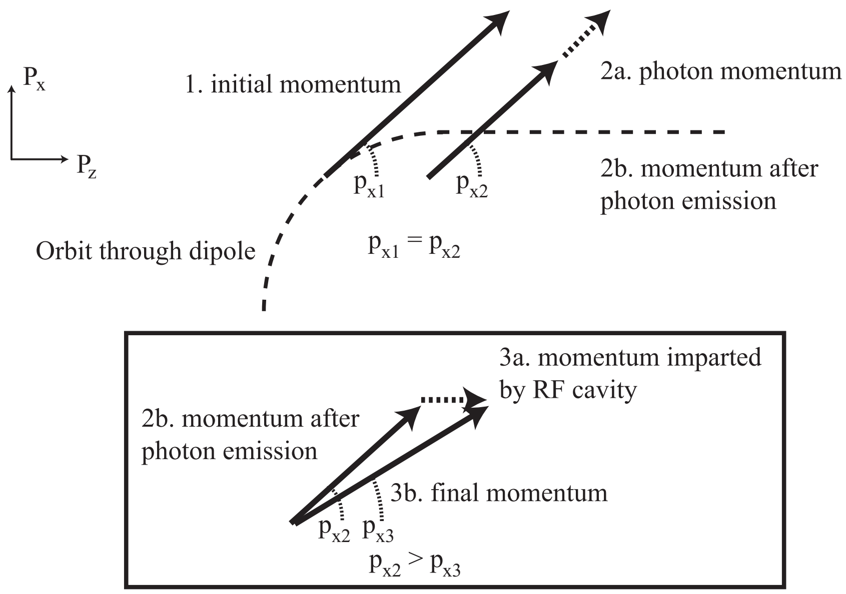

Figure 2.7: Schematic diagram of the reduction in horizontal and longitudinal momentum coming from photon emission in a dipole followed by energy gain, in the form of longitudinal momentum, in a RF cavity.

cavities. The interplay of the emission of radiation in a dipole and the gain in energy from an RF cavity is another important physical phenomenon, as it can change the beam emittance. When an electron travels on a curved path through a dipole and emits a photon, the photon travels tangentially to the path of the electron, with momentum in the tangential direction. For example, if the electron is traveling around a horizontal curve in the $+z$ and $+x$ direction, the photon will have momentum $+p_z$ and $+p_x$, while the electron's momentum will change by $-p_z$ and $-p_x$ (see Figure 2.7).

The energy of the electron will be restored as soon as it passes through the next RF cavity, but since the cavity uses a longitudinal electric field to accelerate the electron it will regain all of its energy in the form of $+p_z$. The result is that the particle's energy will be unchanged from before the emission of a photon to after passing through an RF cavity, but the ratio of P_x to P_z of the electron is reduced

($p_{x3} < p_{x2}$). This mechanism is called radiation damping since the emittance of the beam will be reduced, or damped, by the continual reduction in each electron's horizontal momentum. Since the vertical orbit of the particle is also undergoing betatron oscillations, the electron's momentum can also change by $-p_y$ after a photon is emitted, resulting in vertical emittance damping as well.

Radiation Equilibrium

Synchrotron radiation reduces the horizontal and vertical beam emittances through radiation damping and increases the horizontal beam emittance through quantum excitation. The balance of these two effects is reached after the beam radiates in a circular accelerator for thousands of turns. When these effects reach equilibrium, the horizontal beam emittance is given by the equation [2]:

$$\epsilon_{x,rad} = C_q \gamma^2 \frac{I_5}{\mathcal{J}_x I_2}, \tag{2.12}$$

where:

$$I_5 = \oint \frac{\mathcal{H}}{\rho^3}\, ds \tag{2.13}$$

and $C_q = 3.8319 \times 10^{-13}\,\mathrm{m}$. I_5 is another of the synchrotron radiation integrals and depends on the bending angle all the way around the accelerator and $\mathcal{H}$, which is a function of lattice parameters and is given by [2]:

$$\mathcal{H} = \gamma\eta^2 + 2\alpha\eta\eta' + \beta\eta'^2. \tag{2.14}$$

In this expression, η is the dispersion, the energy dependent trajectory through the accelerator, and η' is the slope of the dispersion. Likewise, $\mathcal{J}_x$ is a function of lattice parameters that includes the bending angle and the dispersion all the way around the accelerator.

If the accelerator does not couple the horizontal and vertical motion, then the vertical beam emittance will damp to zero because quantum excitation is so weak vertically that the radiation damping dominates the equilibration process. In reality, however, an operating accelerator may have skew quadrupole magnets (a quadrupole field rotated by $45\,^{\circ}$) or quadrupoles and sextupole magnets that produce skew errors due to a misalignment in position or rotation. These skew terms couple the horizontal and vertical planes together which means that the minimum vertical emittance is coupled to and determined by the minimum horizontal emittance. The coupling of the horizontal plane to the vertical plane can be made $0.5\,\%$ or smaller by tuning the accelerator to reduce and compensate for the skew errors.

From the preceding sections it is clear that the total effect synchrotron radiation has on the accelerated beam includes both radiation damping, quantum excitation, and transverse coupling. A description of this effect in terms of the accelerator lattice is clearly a complicated combination of the total amount of bending in the ring, magnet misalignments, the beam energy, and the ring's dispersion. These ideas will continue to be discussed throughout this dissertation.

2.4.2 Magnet Nonlinearities

Deviations from ideal magnetic fields are another physical reality that complicates the simplified picture of particle accelerators presented thus far. A dipole bends all particles in the beam by the same angle, with a uniform magnetic field. But a dipole only creates a uniform magnetic field near the center of the field region; when the beam is far from the center of the magnet the edges of the poles produce non-uniform fringe fields. If particles in the beam move to large displacements, they can sample the non-uniform dipole field which can cause the particles to hit the dynamic aperture.

Even in the center of the beam pipe, the dipole field will not be completely uniform if the faces of the two poles are not perfectly smooth or exactly parallel. Errors in the construction of a dipole magnet produce magnetic field errors that can deviate from an ideal dipole field in such a way that the dipole can produce a focusing field like that of a quadrupole. Additionally, errors in a dipole can produce a field with components coming from even higher order magnets than quadrupoles. These deviations are called the higher-order multipole field errors of a magnet.

Multipole field errors complicate the trajectory of a bunch of particles because they alter each particle differently. Some types of field errors in the lattice depend on the distance the particle is displaced from the center of the beam pipe and others depend on the energy of the particle. The cumulative effect of these errors can result in a shrinking of the dynamic aperture [1].

A small dynamic aperture is not desired for a high-performance accelerator so physicists attempt to design the lattice to mitigate these multipole field errors. This is done with additional magnets: quadrupoles can be used to correct the quadrupole-order multipole errors coming from the dipoles, sextupoles can be used to correct the sextupole-order errors on dipoles and quadrupoles, and so on. However, this correction method can be difficult and never completely eliminates all field errors, so higher-order multipole errors are still a critical challenge that must be overcome to achieve successful accelerator operation.

2.4.3 Beam Interactions

There are more electromagnetic sources in particle accelerators than just magnets and RF cavities. The beam itself is an electromagnetic source, a very large one in fact. Even though the charge of each particle is weak, because there are so many particles, the interaction of a beam with itself or with any other beams nearby can be strong enough to alter the trajectory and behavior of the beam. This type of interaction is called a collective effect since it involves all particles in the beam working together; examples include the beam-beam interaction, the fast ion instability, electron cloud, and space charge.

Space Charge

The electromagnetic repulsion of similarly charged particles can act within a single beam in a process called space charge [3]. Space charge involves both the electric and magnetic fields of a moving bunch of similarly charged particles. In this situation, the electric field produces a repulsive force and the magnetic field produces an attractive force. The question of whether or not space charge will blow-up the beam size becomes a question of which force is stronger. At high energies, the beam is traveling near the speed of light and the magnetic field's force balances the electric field's force. But at low energies, the velocity is smaller and the magnetic field's force becomes weaker than that of the electric field. Thus, when the particle beam is at low energy, space charge can be a potentially damaging phenomenon, especially when the beam size is already very small.

Beam-beam Interaction

The electromagnetic attraction of oppositely charged particles can act between two beams in a process called the beam-beam interaction [3]. In the case of electrons and positrons traveling in opposite directions in the same beam pipe, the beam-beam interaction works to pull the two beams together. This can be beneficial when you want the beams to collide and the beam-beam interaction enhances the collision. However, if you want the two beams to pass closely by each other without interacting, the beam-beam interaction can pull the two beams together and deviate their trajectories, resulting in shrinking dynamic aperture limits and particle loss.

Fast Ion Instability and Electron Cloud

There is another interaction involving the beam and any stray particles in the beam pipe that are attracted to the beam and become collected around and behind the beam. When a bunch of electrons passes a point in the accelerator, it can attract positively charged ions nearby which collect behind the electrons and form an ion cloud in the path of the next bunch of electrons. This is called the fast ion instability [3] because the ion cloud will cause the electron trajectories to become unstable very quickly, resulting in a blow up of the beam emittance if the ions are not removed.

For positrons, radiated photons hit the metal beam pipe wall and eject electrons which will be attracted to the positively-charged core of the positron beam. Again, the undesired particles (in this case the electrons) congregate in the center of the beam pipe and blow up the emittance of subsequent bunches because they can be excited and produce their own electromagnetic fields. Since, in this case the bothersome particles are electrons, this is called an electron cloud [3].

2.5 Accelerators in Elementary Particle Physics

The tools and examples given above can be used to understand and describe the operation of particle accelerators in general, regardless of their specific applications. But more detailed examinations of the design and performance of particle accelerators do depend on their specific applications. Some users of particle accelerators want beam sizes as small as possible, while other accelerator users might only care about the final beam energy and no other beam parameter matters for their needs. Thus, the examination of particle accelerators in this dissertation must focus on the specific application relevant here: high energy accelerators used for elementary particle physics experiments.

Elementary particle physics is a branch of physics that studies the fundamental building blocks of the universe and how they interact. The present paradigm of elementary particle physics sets the smallest subatomic particles as the indivisible electron, five related leptons, and six quarks. However, as elementary particle physicists sit at the start of the 21st century they are bound by the explorer's spirit of their predecessors, to ask "Are these twelve particles truly indivisible?"

Particle accelerators, and the physicists who construct and operate them, have been and will continue to be crucial to the hopes of elementary particle physicists to answer this question or to discover some other paradigm-altering particle or force. This is because of the famous equation set forth by Albert Einstein:

$$E = mc^2, \tag{2.15}$$

which says that a particle's energy, E, is related to its mass, m, by a factor of the speed of light squared. This means that if physicists can generate a tremendous amount of energy with a particle accelerator and somehow release that energy, it will transform into a particle of matter with mass as determined by Einstein's equation.

For the past century, particle accelerators have accelerated beams of particles like electrons, e^-, positrons, e^+, protons, p^+, and anti-protons, p^-, to high energy and then directed them into a target where the collision releases enough energy to create new elementary particles for discovery and study. The target used in these "particle collider" experiments can be either solid objects of matter (a block or sheet of some pure element) or another beam of the same or different species of particles coming from the opposite direction.

In a circular accelerator this can be as straightforward as sending the second beam through the same lattice, but in the opposite direction as the first beam, and steering them into collision when desired. In such an accelerator the beams collide at a specific s-coordinate called the interaction point, or IP. The energy released during collisions at the IP is equal to the total energy in the center of mass system and equals the sum of the energies of the two beam, $E_{total} = E_{COM} = E_{beam,1} + E_{beam,2}$.

Using a linear accelerator to create a high energy particle collider is a more challenging operation. That is because two linear accelerators must be pointed directly at each other so that the first beam exits its lattice at exactly the same time as the second beam exits from the other side and the two beams must then collide in the center.

For particle physicists to continuously search for unseen particles more massive than those already discovered, accelerator physicists must begin designing a new maximum energy accelerator before the accelerator that will replace the current energy frontier accelerator is even operational. Currently, the plan is for the next high energy accelerator to be a 0.5 TeV e^+e^- straight-line colliding accelerator called the International Linear Collider. The International Linear Collider will complement the p^+p^+ collisions at the Large Hadron Collider [3], which is a circular collider at 14 TeV that will, upon completion in 2007, supersede the currently operational energy frontier accelerator: the Tevatron [3], a 2 TeV p^+p^- circular collider. The International Linear Collider is the focus of this dissertation and will be covered in more detail in subsequent chapters.

Chapter 3

The International Linear Collider

The historical progression to higher energy particle accelerators has taken us to the next generation energy frontier machine, the International Linear Collider (ILC). The ILC will send a beam of electrons and a beam of positrons down two 10-mile linear accelerators that will accelerate them to an energy of 250 GeV and then collide them at a total energy of 500 GeV. The ILC is proposed to be constructed and operational sometime in the 2010's and is currently in the design phase as several research and development challenges still remain [4, 5].

3.1 Overall Design

The ILC is a 20 mile long complex of particle accelerators (see Figure 3.1). The entire ILC includes sources of electrons and positrons, components to manipulate the electron and positron beams, the main linear accelerator to raise the beam energy to 250 GeV, and final components that are used to efficiently collide the electron and positron beams coming from either side of the ILC.

Elementary particle physicists have specified the main features of the ILC's

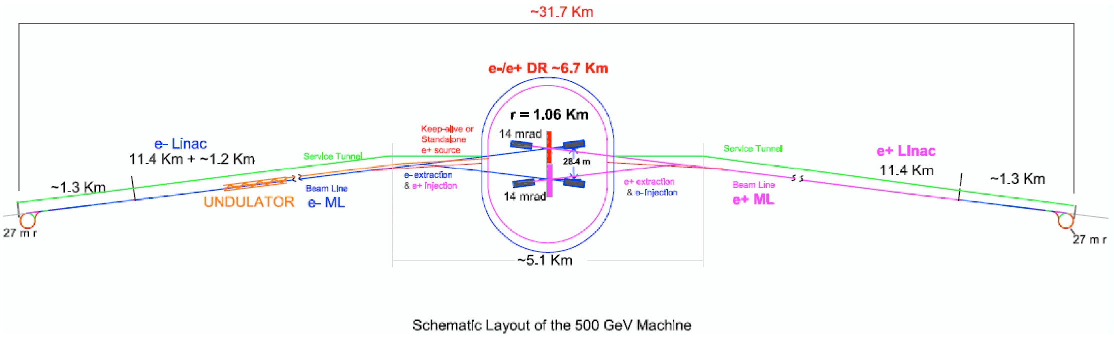

Figure 3.1: Site layout of the International Linear Collider.

Table 3.1: Beam parameters in the ILC.

Beam energy	250 GeV
Particles per bunch	2×10^{10}
Bunches per train	2820
Trains per second	5 Hz
$\gamma\epsilon_x$ at the IP	$10\,\mu\mathrm{m}\cdot\mathrm{rad}$
$\gamma\epsilon_y$ at the IP	$0.04\,\mu\mathrm{m}\cdot\mathrm{rad}$

design so that it will complement the physics that will be studied at the Large Hadron Collider (LHC) [6]. To produce collisions that would complement the research conducted at the LHC, the ILC must accelerate thousands of bunches each with billions of particles and collide them at extremely small emittances (see Table 3.1). However, complementing the LHC with the ILC will not be easy since a single-pass linear machine presents unique advantages and disadvantages as compared to a multi-turn circular accelerator.

The Stanford Linear Collider (SLC) [7] was a linear collider that operated during the 1990's but it differed in a number of respects from a full-fledged linear collider (see Table 3.2). Compared to the SLC, the ILC will accelerate beams 100 times more powerful, focus them 10 times more tightly, and achieve 10,000 times the collision rate. The challenges and risks increase greatly for a linear collider in this parameter range, thus the SLC can only be considered a proof-of-principle for the linear collider concept. As the first ever truly linear high energy collider, the ILC will forge new ground in advanced particle accelerator design and operation.

Table 3.2: Comparison of beam parameters in the SLC and ILC.

	SLC	**ILC**
E_{COM} (GeV)	100	500-1000
P_{beam} (MW)	0.04	5-20
σ_y at the IP (nm)	50-500	1-5
$\mathcal{L}$ ($10^{34}\,\mathrm{cm}^{-2}\mathrm{s}^{-1}$)	0.0003	2

3.1.1 Energy and Particle Species

Collisions of 250 GeV beams are theoretically predicted to be sufficient to either unveil the Higgs boson and supersymmetric particles or to restrict the possibility of their existence at this energy range. If the LHC has already found the Higgs boson and supersymmetric particles, or excluded their existence at this energy range by the time the ILC turns on, then the ILC will still be useful because it will use different particle species than the LHC. With electrons and positrons, the ILC will produce much cleaner collisions than the proton collisions at the LHC. This will allow physicists using the ILC to make measurements that will surpass the precision of those same potential measurements at the LHC [8].

3.1.2 Why A Linear Machine?

The motivation for using a linear instead of a circular accelerator in this energy range does not have as much to do with the advantage of a linear machine as it does the disadvantage of a circular machine, which–simply stated–is its cost.

To accelerate a beam to its target energy in a circular accelerator, RF cavities must replace the energy the beam loses during the emission of synchrotron radiation. At the energy range of previously built electron accelerators, the energy removed by photons emitted from a circular accelerator is minimal. But at high beam energies, replacing the lost energy is non-trivial because the amount of energy lost increases with the 4^{th} power of the beam energy. The power radiated by a beam of N particles with an energy corresponding to γ, bending in a curve of radius ρ is given by the following equation [1]:

$$P_{rad} = \frac{c}{6\pi\epsilon_0} N \frac{q^2}{\rho^2} \gamma^4. \tag{3.1}$$

This equation explains why radiation is not a factor in the operation of proton accelerators, because for electron and proton beams of the same energy, γ_{e-} is two thousand times larger than γ_{p+}.

This equation also suggests that at a very high electron energy, the amount of power radiated in a circular machine of reasonable size will be on the order of the total beam energy. Therefore, replacing this energy with the RF cavities will no longer be cost-effective. The largest circular electron machine ever built was the Large Electron Positron (LEP) ring at CERN which was a $E_{COM} = 180\,\text{GeV}$ e^-e^+ ring with a circumference of 27 km. Using Equation 3.1 on LEP, the synchrotron radiation power corresponds to an energy loss of 4 GeV on each turn, or 2 % of the total beam energy [9]. The cost of enough RF cavities to restore 4 GeV on each turn was not insignificant and would only become worse if LEP were upgraded to higher energies. Thus, LEP provided a practical upper limit to the energy of a circular electron accelerator. However, with a linear accelerator there is no synchrotron radiation and the excessive cost of overcoming the radiation losses can be avoided even at high energy. Thus, it is clear that any electron accelerator with a higher energy than LEP will have to be linear.

3.1.3 Luminosity

In addition to the total energy and species of the colliding particles, the ILC must meet another important output parameter to be useful to the experimentalists searching for the Higgs boson. Because of the extremely low probability of electrons and positrons interacting to produce a previously unobserved particle or phenomenon, maximizing the collision rate, or luminosity, will be critical for the discovery of any new particles. To discover the extremely rare particles physicists have not seen yet requires maximizing the beam energy, as well as the number of interactions, so that the low probability per interaction will still result in a measurably significant discovery.

The number of particles in each beam, how frequently the particles pass through the IP, and how densely the beam is packed all combine to define the luminosity. For Gaussian beams, the luminosity in a linear collider can be approximated by the following equation [1]:

$$\mathcal{L} = \frac{n_b N^2 f_{rep}}{4\pi\sigma_x\sigma_y} H_D, \tag{3.2}$$

where n_b is the number of bunches per train, N is the number of particles per bunch, f_{rep} is the number of trains per second, $\sigma_{x,y}$ are the horizontal and vertical beam sizes, and H_D is the beam-beam enhancement factor.

The total rate of physics events that take place inside the experimental detector is given by the number of interactions per second:

$$R = \mathcal{L}\sigma, \tag{3.3}$$

where $\mathcal{L}$ is determined by the performance of the particle accelerator and the cross-section, σ, is theoretically defined for each type of particle interaction. Both the instantaneous and the integrated luminosity (total $\mathcal{L}$ over the machine's lifetime) must be maximized in order to have a large event rate and a chance of discovering and studying a new elementary particle. In the hopes of discovering the Higgs boson, the ILC has been designed with a peak luminosity of $2 \times 10^{34}\,\mathrm{cm^{-2}s^{-1}}$, which will produce $500\,\mathrm{fb^{-1}}$ of integrated luminosity over four years of operation.

Given Equation (3.2), the beam sizes must be extremely small to produce such a high peak luminosity. In fact, to achieve the same luminosity in a linear collider as a circular collider, the beam sizes must be 10,000 times smaller in a linear collider. This is because the power loads in the main linac of a linear collider limit the repetition frequency to a few Hz, which is 10,000 times smaller than the revolution frequency of a circular collider [2].

The ILC, will achieve this luminosity by colliding 2820 bunches, each containing 2×10^{10} particles, five times per second. The beam-beam enhancement factor in the ILC will be about 2, so the beam sizes at the IP will have to be on the order of 1 nm vertically and 1 μm horizontally. This presents a problem because the particle source can only generate a beam with sizes on the order of 1 mm. Thus, the beam must be focused by a factor of 10^6 from particle creation to particle collision. Quadrupoles are a likely candidate to provide such a large factor of focusing; however, extremely strong quadrupoles cannot be used to focus a millimeter-sized beam down to nanometer-size because of the hourglass effect.

If the IP quadrupoles are so strong that the vertical β-function is shorter than σ_z, then the vertical beam size will vary over the length of the bunch. This is called the hourglass effect because of the hourglass or butterfly shaped distortion it causes in the $z - y$ distribution. If two hourglass-shaped beams were to collide at the IP they would not intersect completely and the luminosity would drop. To avoid this luminosity-limiting effect, the strength of the focusing magnets at the IP

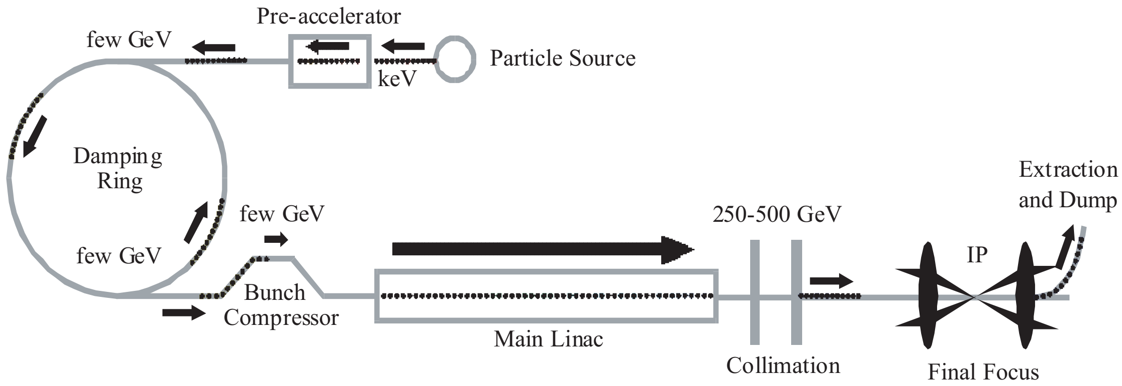

Figure 3.2: Schematic representation of the components of a basic linear collider.

must be small enough that $\beta_y \geq \sigma_z$. The bunch length at the IP will be 300 µm, so the quadrupoles at the IP cannot be strong enough to provide $\beta_y < 300\,\mu\text{m}$. This requires the ILC to keep the whole phase space of the beam small and not just use quadrupoles to focus the beam, which is essentially just trading off between the beam's spread and its divergence. Thus, small beam emittances are crucial for the ILC to achieve its design luminosity.

3.2 Description of Operation

The International Linear Collider is composed of a number of individual particle accelerators and accelerator components that the electrons and positrons pass through in sequence (see Figure 3.2). The first of these components is the source which creates the electron and positron beams in tight groups, or bunches, of particles. The newly created electrons and positrons leave the source and travel to the damping ring which makes the bunches useful for collision by reducing their size and optimizing their timing. Coming out of the damping ring, the bunches travel to the bunch compressor, which, like the damping ring, modifies the bunches to make them ideal for maximum $\mathcal{L}$ collisions, in this case by shrinking their length.

The main linear accelerator, or main linac, is next in the chain of accelerators and it is the longest part of the ILC; it is made up of 10 miles of repeating sections of RF cavities to accelerate the beams and quadrupoles to focus the beams. The two main linacs are the most crucial pieces of the entire ILC and drive many of the design considerations for the rest of the machine. For example, to minimize the power load on the RF cavities in the main linac, the entire ILC cannot cycle faster than five times per second. Therefore, to achieve the desired luminosity, every other component in the ILC must be designed to handle more particles per bunch, more bunches per train, and the stronger collective effects that come with such a high beam current.

The beam delivery and final focus systems are the last machine sections before the interaction point where the electrons and positrons meet and annihilate. The beam delivery system collimates the beam at its final energy before it passes into the final focus system where the beam is squeezed as tightly as possible without driving the hourglass effect just before it collides at the IP in the center of the experimental detector.

Going through each of the sections of the ILC to accelerate a beam of electrons to 250 GeV while creating and preserving the many beam parameters which ultimately produce the target collision luminosity is a challenging task. Doing it twice, the second time with positrons, is even more difficult.

3.2.1 Operational Challenges

The challenge of accelerating two useful beams to 250 GeV translates to very stringent target values for many parameters of the particle beams, and achieving these parameters means that each section of the ILC faces demanding performance requirements. For example, the energy spread of the beam must be kept small enough so that energy-dependent nonlinear effects in the damping ring or bunch compressor are not strong enough to blow up the beam. This means that the positron source must produce as many positrons as possible all at the same energy. In addition, achieving the precise bunch timing required to ensure collision at the IP demands that the elements that extract the beam from the damping rings turn on and off very quickly and cleanly.

As the beams continue through the ILC, they must maintain their very small emittances. This means that effects which can increase the emittance must be minimized otherwise they can build up over 10 miles of linac and push the emittances over the $\gamma\epsilon_x = 10\,\mu\mathrm{m}\cdot\mathrm{rad}$, $\gamma\epsilon_y = 0.04\,\mu\mathrm{m}\cdot\mathrm{rad}$ values required for a luminosity of $2\times10^{34}\,\mathrm{cm}^{-2}\mathrm{s}^{-1}$. Keeping the emittance low throughout the main linac means that the alignment of the quadrupoles and RF cavities in the linac must be extremely precise. In addition, after the main linac the beams must be kept focused so that any clouds of particles that drift outside the core of the beam do not travel all the way to the IP and damage the sensitive experimental detector. This requires collimators in the beam delivery system that are strong and durable enough to scrape away the large amplitude particles and also unobtrusive enough to not hinder the performance of the experimental detector.

To minimize the total amount of energy required to accelerate 2820 bunches of 2×10^{10} particles to 250 GeV, the RF cavities in the main linac will be made of niobium which becomes superconducting when cooled to 4.2 K. Superconducting niobium cavities allow the accelerator to efficiently transfer power to the electrons with minimal losses and so will save money on the total power bill of the accelerator.

Before the International Linear Collider was proposed as a superconducting linear accelerator, there was another collaboration that was proposing this same technology. Based at the German Electron Synchrotron, Deutsches Elektronen-Synchrotron (DESY), the TeV-Energy Superconducting Linear Accelerator (TESLA) collaboration also used superconducting niobium RF cavities [10]. Once the ILC collaboration was formed, efforts to construct TESLA ended, as did those of another proposed linear collider, the Next Linear Collider (NLC) [11]. The design of the ILC has been separate and distinct from that of TESLA; however, much of the knowledge and experience gained from designing TESLA, as well as the NLC, has been applied to producing a design of the ILC which minimizes its operational challenges.

3.3 Principles of Design

The design of the ILC is quite complex given the strict performance requirements on each individual component of the entire 20 mile accelerator. To optimize the design of the ILC, each piece must be studied as thoroughly as if it were its own particle accelerator. Since the ILC is a linear, single-pass machine, each component is most directly impacted by the component immediately preceding it and most directly impacts the component immediately following it. For example, the design of the main linac can be decoupled from other challenges by merely specifying the expected beam parameters coming from the bunch compressor preceding it and the goal beam parameters set by the beam delivery system following it.

This has been a complex and time-consuming process involving a collaboration of international scientists, professors, and students. The technical design of the ILC is currently being finalized by the international community as further studies reveal new problems and additional challenges to the ILC's successful design and operation [5]. Additionally, the specific details of design for the ILC are continually being modified in order to minimize the total cost. One way the ILC is being designed to minimize cost, as well as technical risk, is by using the knowledge and experience gained from the particle accelerators successfully operating all over the world, including concepts that were developed for TESLA.

The focus of the rest of this dissertation will be on the two damping rings in the ILC. At the conclusion of this dissertation, cost-optimized conceptual design will be proposed for one specific component of the ILC damping rings, the wigglers.

Chapter 4

The ILC Damping Rings

Synchrotron radiation is beneficial in circular colliders because the radiation damping process takes transverse momentum away from the beam, shrinking the horizontal and vertical beam emittances. The automatic generation of small emittance beams in circular colliders is crucial to the production of high luminosity collisions with small vertical and horizontal beam sizes as shown in Equation 3.2. However, since the luminosity benefit comes from bending, the ILC will not have any emittance damping without a dedicated circular accelerator in which the beams can be temporarily stored.

This is the purpose of the damping rings in the ILC. The damping rings, two several km circumference rings that store electrons and positrons separately at a few GeV, are the only circular accelerators in the entire ILC. The ILC damping rings are designed so that the synchrotron radiation processes damp the beam from a large injected emittance coming from the particle source to a small extracted emittance beam that travels to the IP.

As long as the damping rings are inserted into the low energy end of the ILC complex, the emitted synchrotron radiation will be more beneficial (by providing small emittance beams) than harmful (by raising the cost of the RF system). Assuming that the ILC components downstream of the damping ring can maintain the small emittance beams, then a low energy circular accelerator is a required component of a successful high energy linear collider.

Table 4.1: Target emittance values in the ILC.

	Horizontal	**Vertical**
$\gamma\epsilon$ at the positron source:	$0.01\,\mathrm{m}\cdot\mathrm{rad}$	$0.01\,\mathrm{m}\cdot\mathrm{rad}$
$\gamma\epsilon$ at extraction from the damping rings:	$8\,\mu\mathrm{m}\cdot\mathrm{rad}$	$0.02\,\mu\mathrm{m}\cdot\mathrm{rad}$
ϵ at extraction from the damping rings:	$0.80\,\mathrm{nm}\cdot\mathrm{rad}$	$2\,\mathrm{pm}\cdot\mathrm{rad}$
$\gamma\epsilon$ at the interaction point:	$10\,\mu\mathrm{m}\cdot\mathrm{rad}$	$0.04\,\mu\mathrm{m}\cdot\mathrm{rad}$

4.1 Description of Operation

The damping rings are circular accelerators that the electron and positron beams are stored in for a few thousand turns, long enough for synchrotron radiation damping to reduce the vertical beam emittance by a factor of 10^6. This factor is set by the demand for small emittance at the IP and the inability of the particle sources to generate a bunch of 20 billion particles with a small enough emittance (see Table 4.1).

The normalized vertical emittance generated at the positron source is $0.01\,\mathrm{m}\cdot\mathrm{rad}$ and the normalized vertical emittance required at the IP to generate $\mathcal{L} = 2 \times 10^{34}\,\mathrm{cm}^{-2}\mathrm{s}^{-1}$ is $0.04\,\mu\mathrm{m}\cdot\mathrm{rad}$. However, to provide $0.04\,\mu\mathrm{m}\cdot\mathrm{rad}$ at the IP, the damping rings actually need to achieve an emittance below that value to provide a safety margin that allows for $100\,\%$ emittance growth in the main linac. Thus, to achieve the target luminosity the damping rings will use radiation damping and very low transverse coupling to reduce the electron and positron beams to $\gamma\epsilon_x = 8\,\mu\mathrm{m}\cdot\mathrm{rad}$ and $\gamma\epsilon_y = 0.02\,\mu\mathrm{m}\cdot\mathrm{rad}$.

The challenge in achieving these small emittances is that the entire beam has to damp fast enough to allow the whole machine to cycle fives time per second.

Table 4.2: Target beam parameters of the ILC damping ring.

Pulse repetition rate, f_rep	5 Hz
Number of particles/bunch, N	2×10^{10}
Nominal number of bunches, n_b	2820
Maximum number of bunches	5640
Maximum injected emittance	$0.09\,\mathrm{m \cdot rad}$
Maximum injected energy deviation	$\pm 0.5\,\%$
Target extracted $\gamma\epsilon_x$	$8\,\mathrm{\mu m \cdot rad}$
Target extracted $\gamma\epsilon_y$	$0.02\,\mathrm{\mu m \cdot rad}$
Extracted rms bunch length, σ_z	6 mm
Extracted rms energy spread, σ_δ	$0.13\,\%$

That is 2820 bunches of 2×10^{10} particles per bunch being damped to µm-scale emittances every 200 ms. In addition, the damping rings must provide more beam parameters than just the emittances (see Table 4.2). All of the beam parameters in the damping rings have been specifically chosen to mitigate challenges coming from inside the damping ring (like collective effects, dynamic aperture, and radiation damping) and from the interface of the damping ring with other machine components (like the sources, bunch compressor, and main linac). The challenges which dictate the performance requirements of the damping rings will be given in the following sections.

4.1.1 Challenges Arising From Collective Effects

The beam current will be quite large, 400 mA, making the ILC damping rings susceptible to a number of collective effects. Electron cloud is a concern in the positron damping ring and the fast ion instability will cause problems in the electron damping ring. This is because both beam interactions could increase the beam emittances. Mitigating the emittance increases caused by these instabilities requires a large spacing between the bunches in the damping ring to give the electron and ion clouds time to dissipate before the next bunch arrives. Thus, the desire to avoid collective effects motivates designing a large circumference damping ring [12].

4.1.2 Challenges Arising From The Bunch Compressor

Another challenge to the operation of the damping ring arises when the quality of the damping ring's extracted beam is coupled with the performance of the bunch compressor. The damping rings need to output bunches that are short enough and small enough in energy spread that the bunch compressor can accept them. The bunch compressor is designed to accept a particle distribution long in longitudinal position ($\sigma_z = 6\,\mathrm{mm}$) and small in longitudinal spread ($\sigma_\delta = 0.15\,\%$). It will then manipulate the distribution and return a beam with a short bunch length ($\sigma_z = 300\,\mu\mathrm{m}$) and large energy spread ($\sigma_\delta = 1.5\,\%$). However, without a careful design, nonlinear dynamics and collective effects in the damping ring will increase the bunch length and energy spread, greatly increasing the costs and risks of the bunch compressor.

4.1.3 Challenges Arising From The Main Linac

The performance of the main linac also dictates parameter requirements in the damping ring. The main linac accelerates a train of 2820 bunches with 337 ns between each bunch. For that bunch train to fit as is in the damping ring would require a 285 km circumference ring. An alternative approach is to compress the bunch train in the damping ring by injecting and extracting bunches individually, as opposed to the whole train at once, thereby using the injection and extraction kickers to specify a bunch spacing below 337 ns in the damping ring.

The damping ring kickers are further challenged by the timing requirements in the ILC which require that bunches be extracted from the damping ring in a non-sequential order. This means that the extraction kicker must be at peak field to eject one bunch and at zero field to not disturb the very next bunch. Thus, the time the extraction kicker takes to rise to peak field and fall to zero sets the minimum spacing between bunches in the damping ring. So the smaller the circumference of the damping ring, the smaller the spacing between bunches, and the faster the extraction kicker must turn on. Conventional technology kickers can provide a 20 ns rise-time without too much risk; this would correspond to 2820 bunches fitting in a 17 km circumference ring. However, proven technologies have not advanced to a level where fast rise- and fall-time kickers are available that produce a field smooth enough to cleanly extract a bunch at the strength and rate required in the ILC damping ring. So like the collective effects, the technical challenge of the extraction kicker motivates a large circumference damping ring [12].

4.2 Acceptance

Like the bunch compressor and the main linac (which are sequentially after the damping ring), the particle source (which is sequentially before the damping ring) also constrains design requirements for the damping rings. This is because the damping rings need to be designed to accept and store as many particles as possible from the electron and positron sources. Equation 3.2 shows that the final collision luminosity depends directly on the total number of particles in the bunch, N. Thus, to maximize $\mathcal{L}$ the damping rings should not waste any of the particles coming from the source.

The ILC positron source will use synchrotron radiation photons to pair produce electrons and positrons, and discard the electrons eventually leaving a beam of only positrons. Unfortunately, this process will not produce a tight beam of positrons and consequently the initial positron emittance will be very large, $0.01\,\mathrm{m}\cdot\mathrm{rad}$.

Thus, the positron damping ring needs to have a large injection aperture to accept the entire large emittance positron beam. Though the electron beam emittance will not be as large as the positron beam when it is created, a large acceptance for the electron damping ring is also required to provide the maximum possible margin of error for operation of the ring. Without a large aperture electrons and positrons will be lost, which is bad for luminosity and also bad for the damping ring magnets that will get damaged by the radiation dose of the lost beam. Loss of positrons can happen on the dynamic or physical apertures, so both need to be large in the damping ring.

4.3 Damping Rates

In circular electron machines, synchrotron radiation damping and quantum excitation counteract each other, with damping decreasing and excitation increasing the beam emittance. The result is that the beam emittance is damped for many turns until the excitation becomes strong enough to balance the damping, and the two radiation processes equilibrate (see Figure 4.1). The final emittance a beam damps to depends on the source's injected emittance, ϵ_{inj}, and the lattice's

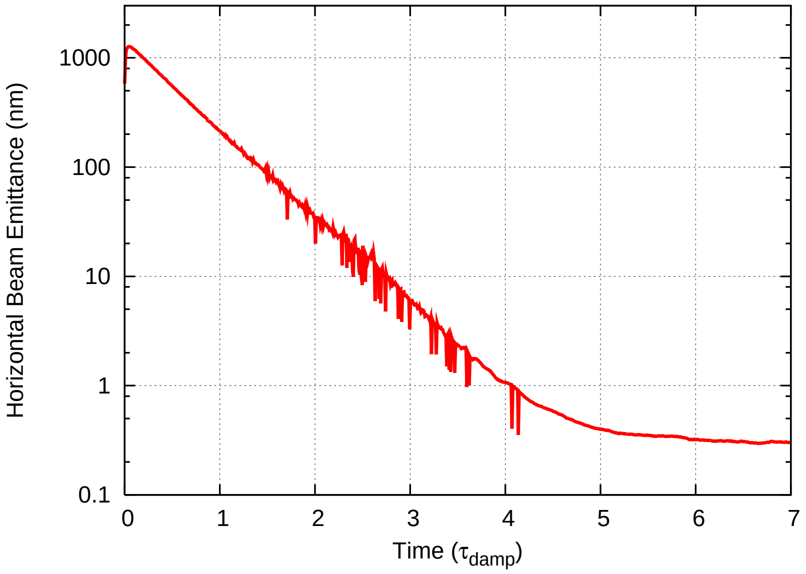

Figure 4.1: Reduction in beam emittance over time until radiation equilibrium is reached.

radiation equilibrium emittance, ϵ_{rad}, and is given by [2]:

$$\epsilon(t) = \epsilon_{inj} e^{-2t/\tau_{damp}} + \epsilon_{rad}(1 - e^{-2t/\tau_{damp}}). \tag{4.1}$$

Here, τ_{damp} is the damping time which is related to the energy of the beam and the total amount of bending in the ring, given by:

$$\tau_{damp} \propto \frac{1}{E^3 I_2}. \tag{4.2}$$

Thus, to damp the beam faster requires raising the beam energy or increasing the I_2 integral by bending the beam in a smaller radius, similar to increasing the energy loss per turn in Equation 2.9. Depending on the energy and circumference, τ_{damp} in electron accelerators ranges from 1,000 to 100,000 turns or more.

In the case of the ILC, the damping ring lattice is designed to produce a radiation equilibrium horizontal beam emittance of $\gamma\epsilon_x = 6\,\mu\mathrm{m}\cdot\mathrm{rad}$ and will be aligned precisely enough to minimize skew fields and keep the transverse coupling at about 0.3 % to achieve the desired extracted vertical emittance. Therefore, damping the vertical emittance from $\gamma\epsilon_y = 0.01\,\mathrm{m}\cdot\mathrm{rad}$ at the positron source to $\gamma\epsilon_y = 0.02\,\mu\mathrm{m}\cdot\mathrm{rad}$ at extraction from the damping ring means that, from Equation 4.1, each individual electron and positron must be stored in the damping ring for eight damping times. Given that the beams will only be stored in the damping rings for 200 ms, the damping rings must be designed with $\tau_{damp} = 25\,\mathrm{ms}$.

To achieve such a short damping time, the ILC damping rings need to have a lot of bending. This will generate the synchrotron radiation needed to allow the beam to emit enough energy per turn to damp quickly. The easiest way to do this is to have a very small circumference accelerator so that the radius of curvature goes down and the revolution time is shorter. But the intrabeam instabilities and extraction kicker requirements prohibit using a small circumference damping ring, therefore the damping ring must meet $\tau_{damp} = 25\,\mathrm{ms}$ with a large circumference ring [12].

This requires that the accelerator must be equipped with dedicated synchrotron radiation production components that increase the integral of $1/\rho^2$ without changing the overall circumference. A magnet that alternately bends the beam left and right will do exactly this, generate a lot of synchrotron radiation and not change the overall circumference or shape of the ring.

The wiggling trajectory of the beam through this type of magnet gives it its name–it is a wiggler magnet. Wigglers are inserted in particle accelerators specifically for the generation of a lot of synchrotron radiation. In the ILC damping rings, hundreds of meters of wiggler magnets will increase the amount of radiation damping and achieve $\tau_{damp} = 25\,\mathrm{ms}$ in a large circumference damping ring. Wiggler magnets are the focus of this dissertation and will be described more completely in the following chapter.

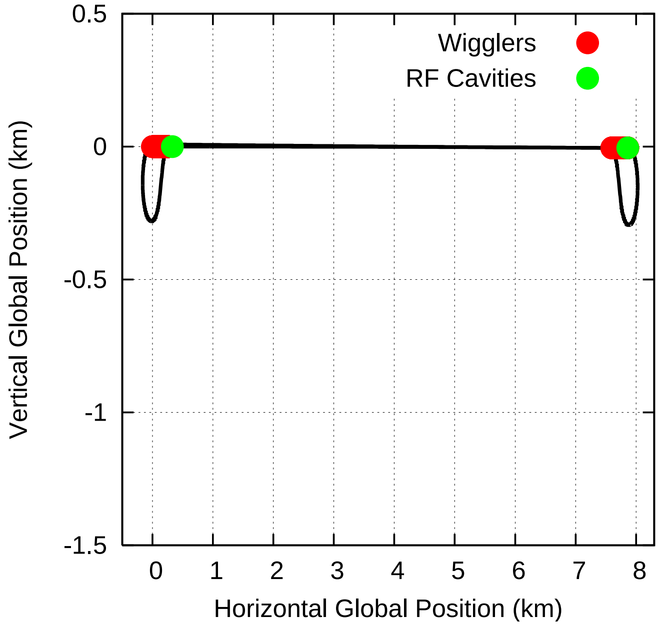

Figure 4.2: Site layout of the TESLA damping ring, showing the position of the wigglers and RF cavities and the dogbone-like shape.

4.4 The TESLA Damping Ring

When the collaboration was formed to design the International Linear Collider, the most complete damping ring design that met the majority of the ILC's requirements was the one from the TESLA linear collider. Because of this, initial studies of the ILC damping ring expanded on the experience and knowledge gained from the TESLA damping ring.

The TESLA ring was a proposed 5 GeV machine that was designed with 20 ns rise-time kickers, thus giving the TESLA damping rings a total circumference of 17 km [10]. To eliminate the need to dig 17 km of tunnel, the TESLA rings were designed in a dogbone-like shape with the majority of the perimeter of the ring being contained in the same tunnel as the main linac (see Figure 4.2). Additional parameters of the TESLA damping ring design are given in Table 4.3.

A N-fold symmetric accelerator lattice is one where the magnet cells repeat N

Table 4.3: Target beam parameters of the TESLA damping ring.

Damping time (ms)	28	
Number of bunches	2820	
Bunch spacing (ns)	20	
Current (mA)	160	
Extracted σ_δ (%)	0.13	
	Inj.	**Ext.**
$\gamma\epsilon_{x,e^+}$ (m · rad)	1×10^{-2}	8×10^{-6}
$\gamma\epsilon_{y,e^+}$ (m · rad)	1×10^{-2}	2×10^{-8}

times; such a ring has the benefit that nonlinearities coming from the field in one magnet can be canceled by the nonlinearities coming from the identical field in the next repeating sequence. The cells that make up the TESLA dogbone shaped ring do not repeat at all and this led researchers to be concerned over the possibility of resonances in the tune plane making the TESLA ring less stable and harder to operate.

Achieving a 25 ms damping time in the 17 km TESLA ring requires that the beam radiate enough photons to lose 20 MeV of energy on every turn. With no wigglers, the TESLA ring radiates 1.1 MeV per turn. Thus, in order to radiate 20 MeV per turn in a 17 km dogbone ring, the TESLA damping ring was designed with 400 m of wiggler magnets. Using such a large number of wigglers to achieve the damping time generated a lot of concern over the potentially poor performance of the TESLA damping ring.

These performance issues were confirmed in dynamic aperture simulations which show a small dynamic aperture without wigglers that is due to the asymmetric

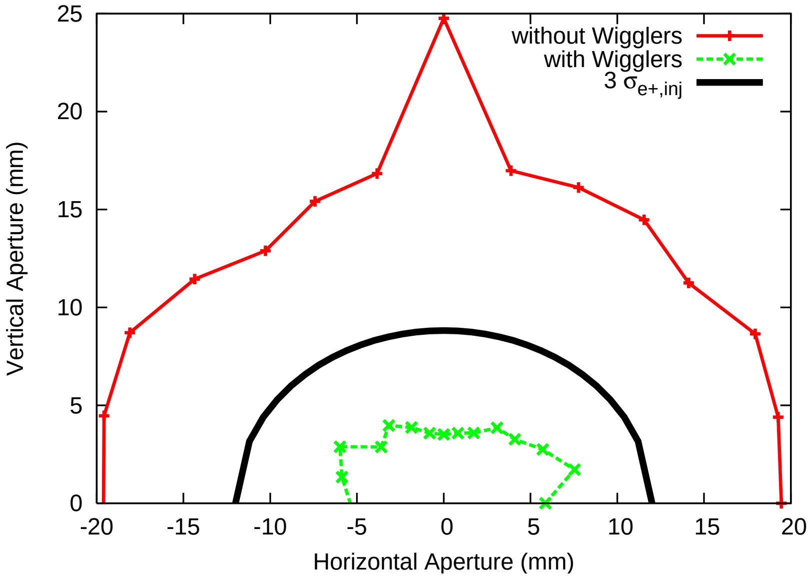

Figure 4.3: The TESLA dynamic aperture with and without wigglers in the lattice. The 3σ curve encloses 99 % of the injected positrons.

shape of the ring, and an even smaller aperture with wigglers (see Figure 4.3). The dynamic aperture in this plot is a computer simulation of the maximum injected particle amplitude that is stable over one damping time. The dynamic aperture target is 3 times the injected positron beam size so that over 99 % of the injected particles will be stable at injection. With such a poor performance of the TESLA ring even without wigglers, the design of the ILC damping ring required a thorough reanalysis and reassessment of the TESLA damping ring design including a comparison of the dogbone ring against all other candidate ILC damping ring designs.

4.5 The Baseline ILC Damping Ring

By the time the ILC collaboration was formed, six damping ring lattices in addition to the TESLA lattice were being designed. These additional lattices gave many more options and potential for a comparison of the pros and cons of different

Table 4.4: Details of the seven reference lattices used in the damping ring configuration studies.

Lattice name	**Circumference (km)**	**Energy (GeV)**	**Lattice style**	**Layout**
PPA	2.82	5.00	π	circular
OTW	3.22	5.00	TME	racetrack
OCS	6.11	5.07	TME	circular
BRU	6.33	3.74	FODO	dogbone
MCH	15.94	5.00	FODO	dogbone
DAS	17.01	5.00	π	dogbone
TESLA	17.00	5.00	TME	dogbone

types of damping ring designs. The seven damping ring designs covered a range of beam energies, circumferences, magnet cell structures, and shapes (see Table 4.4). Each of these damping ring lattices had merits, but they were difficult to compare because each one was being designed by a different laboratory.

A detailed damping ring configuration study was undertaken to evaluate each of the seven damping ring lattices using the same tools and procedures by a specified team of scientists [13]. Each team evaluated every lattice on a different criterion. Teams looked at the collective effects and instabilities, the dynamic aperture, the magnet alignment sensitivities, injection and extraction considerations, and the cost requirements of each lattice.

The result of this configuration study was a consensus design for the new baseline ILC damping ring [13]. The baseline ILC damping ring was selected to keep the TESLA damping ring's beam energy (5 GeV) because it would provide a bal-

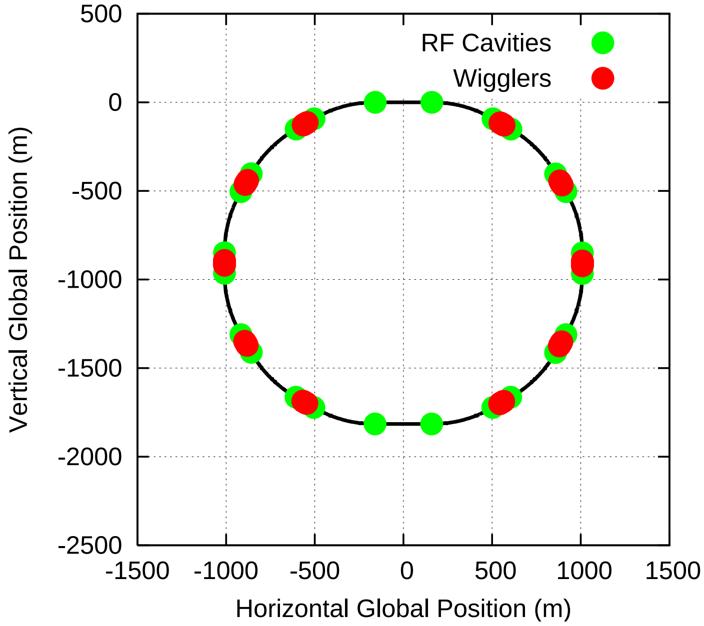

Figure 4.4: Site layout of the baseline ILC damping ring (OCS), showing the position of the wigglers and RF cavities.

ance between poor collective effects at a low energy and the difficulty of aligning the magnets precisely enough to keep the emittance small at a high beam energy. However, the baseline ILC damping ring deviates from the TESLA ring in its size and shape, a more conventional 6 km circular shaped ring was chosen (see Figure 4.4). The 6 km circumference was chosen because it would provide a balance between the expense of a large ring and the damaging collective effects of a small ring.

Two lattices in Table 4.4 meet the specified energy and circumference requirements: OCS and BRU. The OCS lattice was chosen as a starting point for further refinement of the baseline damping ring because its circular shape had a higher degree of symmetry and resulted in a larger dynamic aperture than the dogbone-shaped BRU lattice. Additional recommendations from the ILC damping ring configuration study included using normal conducting electromagnets for the dipoles,

Table 4.5: Injected and extracted beam parameters for the baseline ILC damping ring.

Damping time (ms)	25	
Number of bunches	2820	
Bunch spacing (ns)	4-7	
Current (mA)	400	
Bunch length (mm)	6	
	Inj.	**Ext.**
σ_δ (%)	1	0.14
$\gamma\epsilon_{x,e^+}$ (m · rad)	1×10^{-2}	8×10^{-6}
$\gamma\epsilon_{y,e^+}$ (m · rad)	1×10^{-2}	2×10^{-8}

quadrupoles, and sextupoles and superconducting 650 MHz cavities for the RF system. Required and target beam parameters at the injection and extraction points of the damping ring were also specified (see Table 4.5).

A 6 km circumference ring still requires the use of approximately 200 m of wiggler magnets to achieve $\gamma\epsilon_y = 0.02\ \mu\mathrm{m} \cdot \mathrm{rad}$ in 25 ms. Though half as many wigglers are needed than in the TESLA damping rings, wigglers are still a potentially challenging component of the ILC damping rings. The damping ring configuration study investigated the available wiggler design options and recommended using superconducting technology for the wiggler magnets. The motivation behind this investigation and recommendation will be covered specifically in Section 6.3.

4.5.1 Further Research and Development Requirements

The design of the baseline ILC damping ring has continued to be refined and optimized as new challenges and risks are understood. For example, mitigating the electron cloud is a very important challenge still remaining. In fact, if techniques to actively remove the electron cloud between the tightly spaced positron bunches in the damping ring are not developed, the positrons may have to be damped in two 6 km damping rings at once to double the bunch spacing.

Designing an optimized wiggler magnet is another very important research and development task for the ILC damping ring collaboration. The wigglers in the damping rings have been specified as using superconducting technology, but wiggler magnets can produce difficult beam behavior and can become very expensive if they are not properly designed. Thus, with hundreds of meters of wigglers in the damping rings, a well designed superconducting wiggler is critical for the minimized cost and successful performance of the ILC and is the focus of the rest of this dissertation.

Chapter 5

Wiggler Magnet Fundamentals

The uniform magnetic field of a dipole bends an electron beam in a circular arc, resulting in synchrotron radiation being emitted tangentially from the beam's path. The alternating magnetic field of a wiggler produces synchrotron radiation similar to that of a dipole; however, a wiggler does not bend the electron beam away from its previous trajectory. Thus, wigglers can raise the amount of emitted synchrotron radiation in a ring without changing the ring's overall size and shape.

The increased production of synchrotron radiation by wigglers is used for a variety of applications in different types of accelerators. For example, light sources use wigglers (and their close relatives, undulators) to generate synchrotron radiation for high-quality x-ray diffraction studies of biological samples. Alternatively, damping rings and storage rings use the synchrotron radiation from wigglers to alter the behavior of the electron beam. This is because, depending on how individual accelerators are designed and operated, wiggler generated radiation can increase or decrease the energy spread and the horizontal and vertical emittances of the particle distribution. In the International Linear Collider, the damping rings will be precisely tuned to cause the wiggler radiation to reduce the beam's emittance, thereby increasing the collision luminosity and the chances of finding new physics.

However, designing and operating wigglers that damp the beam's emittance in the ILC is challenging because of additional, non-desired features of wigglers. Wiggler magnets produce complicated magnetic fields which makes it challenging to design a wiggler that has minimal negative impact on the beam. Computer simulations are an important part of designing a wiggler as they help to determine its impact on the beam before it is actually constructed. However, the generation of a computer model of the wiggler is difficult given its complicated magnetic fields. This chapter will describe the wiggler design and simulation challenges and the techniques used to overcome these challenges.

5.1 What are Wigglers?

Wigglers are composed of a series of alternating north-pole/south-pole dipole magnet pairs which oscillate the beam's trajectory (see Figure 5.1). The vertical magnetic field in a wiggler varies from $+B_0$ to $-B_0$ in the center of the magnet poles, with typical values of the peak field being $0.1 - 10\,\mathrm{T}$. The vertical field in a wiggler varies from $+B_0$ to $+B_0$ over one wiggler period, λ_w, and repeats over the entire wiggler length, L_w. The shape of the field variation is controlled by the size and spacing of the poles and can be anything between a sinusoidal wave and a nearly square wave. Wiggler magnets also produce horizontal and longitudinal magnetic fields but these components are weaker and produce less of an effect on the beam.

Like any other magnet in an accelerator, the magnetic fields in a wiggler can be produced with either permanent magnet or electromagnet technologies. Permanent magnets are devices that produce an inherent magnetic field. Electromagnets use electrical currents in coils of wire to produce magnetic fields. If these wires are made of a material that conducts electricity without resistance below a critical temperature, then it is called a superconducting electromagnet. One difference between these technologies is that permanent magnets cannot be turned off (unless their poles are physically separated) while electromagnets become weaker or

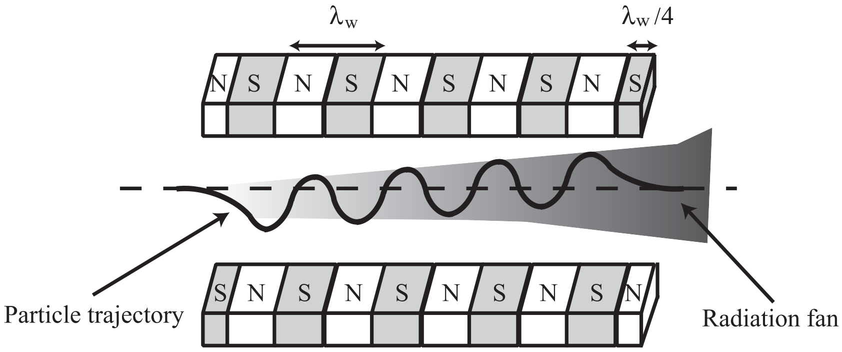

Figure 5.1: A wiggler magnet, including particle trajectory and fan of emitted radiation. The end poles are shorter to return an incoming on-axis beam to its original trajectory.

stronger with the current flowing in the wire. In the case of large aperture wigglers, superconducting electromagnets are typically used above $1-2\,\mathrm{T}$ because they are not as large or as expensive as comparable strength permanent magnets.

5.1.1 Particle Trajectory

The horizontal and longitudinal magnetic fields in a wiggler cannot be ignored in an accurate treatment of a wiggler's negative impacts on the beam and will be discussed further in the following section. For now, B_x and B_z are ignored and B_y is approximated as perfectly sinusoidal, given by:

$$B_y(s) = B_0 \sin\left(\frac{2\pi}{\lambda_w} s\right). \tag{5.1}$$

Solving the equation of motion for an electron moving through this field, yields a sinusoidal oscillation in the electron's horizontal trajectory given by [1]:

$$x(s) = \frac{K}{\gamma}\frac{\lambda_w}{2\pi} \cos\left(\frac{2\pi}{\lambda_w} s\right). \tag{5.2}$$

Here, K is the wiggler parameter and is related to the strength and period of the field by:

$$K = \frac{eB_0}{mc}\frac{\lambda_w}{2\pi} = 93.4 B_0[\mathrm{T}]\lambda_w[\mathrm{m}]. \tag{5.3}$$

The sinusoidal oscillation of a particle's trajectory inside of a wiggler is beneficial because it is what produces the synchrotron radiation, but if that oscillation propagates through the rest of the accelerator problems can occur. Thus, wigglers are designed to take a particle that comes in on-axis, $(x, x', y, y') = (0, 0, 0, 0)$, wiggle its trajectory, and then return it to the beam axis (see for example Figure 5.1). To achieve this, the first and second field integrals must be zero:

$$\int_0^{L_w} B_y(x, z)\, dz = 0, \tag{5.4}$$

$$\int_0^{L_w}\int_0^{z} B_y(x, z')\, dz'\, dz = 0. \tag{5.5}$$

The first integral of the vertical magnetic field in the wiggler controls the angle of the particle's outgoing trajectory. By pairing equal but opposite strength wiggler poles adjacent to each other, the first integral and thus the outgoing angle can be zeroed. The second integral of the vertical magnetic field determines the position offset of a particle as it exits a wiggler. To zero this effect, the strength of the poles at the end of the wiggler are tapered to transition $B_y(z)$ smoothly from zero to B_0. Changing the strength of the magnetic field coming from the end poles is achieved by changing the length of the end poles (see for example Figure 5.1) or, if it is an electromagnetic wiggler, by reducing the current in the end pole coils.

5.1.2 Undulators and Wigglers

The wiggler parameter is a typical way to characterize a wiggler's field since it does not depend on the beam energy or any aspect of the rest of the accelerator. The

K-value of a wiggler is related to the maximum angle of the electron's oscillating trajectory, Θ, by:

$$\Theta = \frac{K}{\gamma}. \tag{5.6}$$

This relationship leads to an important property of the radiation emitted by a wiggler or undulator. If the electron oscillates with a maximum angle less than the opening angle of the cone of emitted radiation ($\Theta < 1/\gamma$), then the radiation emitted by different periods coherently superposes which produces intense monochromatic radiation [1]. This characteristic of the radiation disappears if the electrons have an angle of oscillation larger than the angle of spread in radiation ($\Theta > 1/\gamma$). Thus, an important distinction arises between small oscillation magnets (undulators), and large oscillation magnets (wigglers) that can be characterized by the relationship:

$$\begin{aligned} \text{Undulator}: &\quad K \leq 1, \Theta \leq 1/\gamma \\ \text{Wiggler}: &\quad K > 1, \Theta > 1/\gamma. \end{aligned} \tag{5.7}$$

From this idealized, perfectly sinusoidal wiggler field model, the basic trajectory of an electron through a wiggler is known, as is the difference between a wiggler magnet and an undulator magnet. However, the exact trajectory of an electron through a wiggler is complicated by the realities of an actual wiggler. A real wiggler has horizontal and longitudinal fields in addition to the vertical field, all of which vary as the particle moves away from the center of the magnet. These realities contribute to the nonlinearities present in wigglers that make them so difficult to operate.

5.2 Wiggler Nonlinearities

The magnetic fields in wigglers produce nonlinear terms in the equations of motion for charged particles moving through them which greatly complicates the beam dynamics of the entire accelerator [14, 15, 16]. Wiggler nonlinearities can cause particles moving at different amplitudes to have tunes that vary in such a way that they cannot be easily corrected with higher-order multipole magnets. This is called an amplitude-dependent tune-shift and can result in particles crossing resonance lines in the tune plane as they grow in amplitude. These resonances can accelerate a particle's growth in amplitude and significantly reduce the maximum amplitude of stable orbits in the ring, thus shrinking the dynamic aperture.

5.2.1 Idealized Nonlinearities

A description of wiggler nonlinearities is simplified by separating the dominant nonlinearity that is inherent in all wigglers and the weaker nonlinearities that can be controlled by the shape of the wiggler poles. The inherent nonlinearity comes from the periodic arrangement of north-pole/south-pole magnet pairs and cannot be avoided with different sizes or shapes of poles. This is because this inherent, or idealized, nonlinearity comes about from the longitudinal field that arises from a periodic arrangement of north and south poles.

In fact, wigglers are unique among magnets commonly used in particle accelerators because they have significant longitudinal fields in addition to their transverse fields (see Figure 5.2). This causes a problem when coupled with the fact that the vertical field in a wiggler produces a transverse wiggle in the orbit of a particle. The problem is that the axis of the beam and the axis of the magnetic field are not

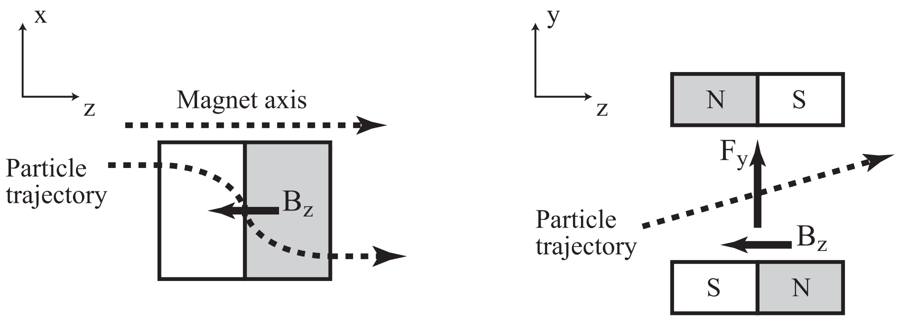

Figure 5.2: Illustration of the inherent vertical wiggler nonlinearity coming from the longitudinal field having a horizontal component in the reference frame of the particle (on the left) which results in a vertically defocusing force (on the right).

aligned, therefore, a horizontal orbit wiggle results in the non-negligible longitudinal field effectively having a horizontal component (see Figure 5.2). This effective horizontal field produces a vertical force on the particle that strongly defocuses its trajectory in a way that more quadrupoles cannot counteract.

Examining the cause and effect of this nonlinearity more closely requires knowledge of the entire magnetic field in the wiggler; however, a full and complete definition of the wiggler's field is not required to approximate the strength of the inherent wiggler nonlinearity. That is because this nonlinearity comes from the periodic arrangement of the poles and can be described using only the peak field and period of a wiggler. Thus, a description of this nonlinearity can be provided with an ideal wiggler model which is infinitely long and infinitely wide.

A further simplification of the field can be made by separating the field into harmonics using the linear superposition of electromagnetic fields. The inherent nonlinearity from an idealized wiggler is driven by the dominant, fundamental field harmonic which has a sinusoidal vertical field on-axis with an unknown vertical position dependence, as shown in:

$$B_y(y,s) = B_0\, b_1(y) \cos{(k_w s)}. \tag{5.8}$$

Determining the dependence of the vertical field on vertical position requires solving Maxwell's equations, $\nabla \times \mathbf{B} = 0$ and $\nabla \cdot \mathbf{B} = 0$, and reveals that the vertically dependent field amplitude of the first wiggler field harmonic is $b_1(y) = a \cosh{(k_w y)} + b \sinh{(k_w y)}$. Using the symmetry of the field and more of Maxwell's equation to solve for a, b, and $B_z(y,s)$, the complete magnetic field from this ideal wiggler is given by [17]:

$$\begin{aligned} B_x(y,s) &= 0, \\ B_y(y,s) &= B_0 \cosh{(k_w y)} \cos{(k_w s)}, \\ B_z(y,s) &= -B_0 \sinh{(k_w y)} \sin{(k_w s)}, \end{aligned} \tag{5.9}$$

where $k_w = \frac{2\pi}{\lambda_w}$ is the wavenumber. The basic form of this expression is similar to the terms in a summation of all harmonics for a realistic wiggler magnet which is finitely wide and long; the entire wiggler field is not required to describe the inherent nonlinearity but will be discussed in greater detail in future sections.

The difference between the beam trajectory and the magnet axis is what causes B_z to impact the vertical trajectory of the beam. This difference is given by the wiggling angle as a function of s, given by:

$$\theta(s) \propto \int_0^s B_y\, ds \propto \frac{B_0}{k_w} \cosh{(k_w y)} \sin{(k_w s)}. \tag{5.10}$$

The projection of the longitudinal magnetic field in the horizontal direction is given by:

$$B_{x,effective} = B_z \tan\theta \approx B_z \theta. \tag{5.11}$$

Which, after inserting Equation 5.9 and 5.10, becomes:

$$B_{x,effective} = -(B_0 \sin(k_w s))^2 \frac{\sinh(k_w y)\cosh(k_w y)}{k_w}. \tag{5.12}$$

By expanding the hyperbolic functions up to 5$^{\text{th}}$ order, the dependence of the vertically defocusing component of the longitudinal field is [17]:

$$B_{x,effective} = -(B_0 \sin(k_w s))^2 (y + \frac{2}{3}k_w^2 y^3 + \frac{2}{15}k_w^4 y^5 + \ldots). \tag{5.13}$$

Finally, up to 3$^{\text{rd}}$ order, the y equation of motion for a charged particle moving through such a field is [18]:

$$y'' \propto B_0^2 (y + \frac{2}{3}k_w^2 y^3). \tag{5.14}$$

The first term in this expression is equivalent to quadrupole-like linear focusing. Through this term, wigglers can change the tune of a circular accelerator by an amount on the order of 0.1 per wiggler. However, this effect can be counteracted in a straightforward manner by modifying the strengths of all of the quadrupoles in the ring.

The second term is the inherent nonlinearity that all wigglers possess which complicates the beam dynamics in an accelerator. This cubic focusing is similar to an octupole magnet, but only in the vertical plane. Thus, wigglers produce a shift in the vertical tune that depends on the particle's amplitude like [19],

$$\Delta Q_y(y) \propto B_0^2 \frac{y^2}{\lambda_w^2}, \tag{5.15}$$

growing with the vertical beam position squared (see Figure 5.3). Since this nonlinearity is only in one plane, it cannot be corrected with compensating octupoles without introducing the same nonlinearity in the horizontal plane.

In addition to growing with the vertical beam position, the vertical tune shift becomes stronger for shorter period wigglers (see Figure 5.4). This nonlinearity

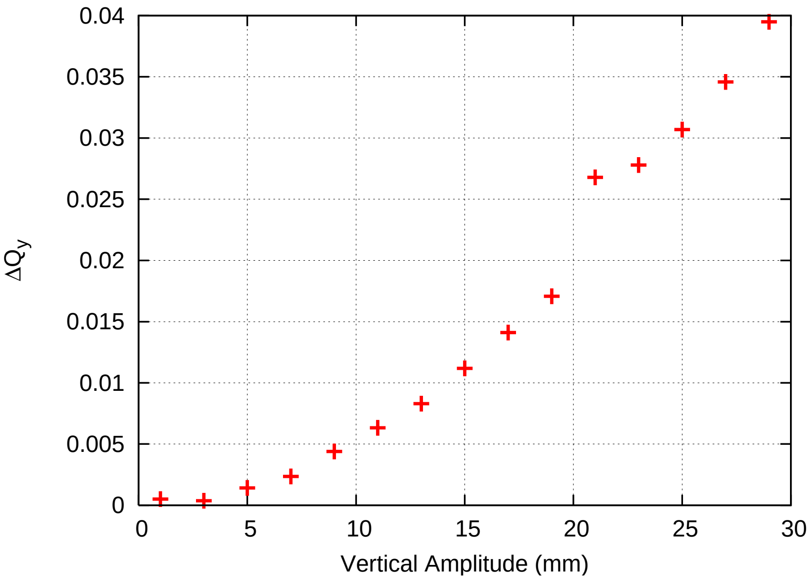

Figure 5.3: Example, from simulations with whole accelerator lattice, of inherent wiggler vertical tune shift as it grows with the beam's vertical position, for a wiggler with $\lambda_w = 40\,\mathrm{cm}$.

is inherent in the fundamental design of wigglers and is thus unavoidable, but by carefully choosing a magnetic field low enough and a period long enough, the effect can be minimized.

5.2.2 Realistic Nonlinearities

A realized wiggler possesses the inherent vertical octupole nonlinearity but it also possesses nonlinearities that come from a finite width and finite length magnet. These boundary conditions can cause additional vertical tune variation, as well as horizontal tune variation that can result in particles becoming unstable and colliding with the physical aperture, even for particles near the core of the beam.

One important nonlinearity that is present in a realistic wiggler magnet with finite width poles, comes from the fact that particles at different positions in the magnet will experience different forces. For example, the vertical magnetic field

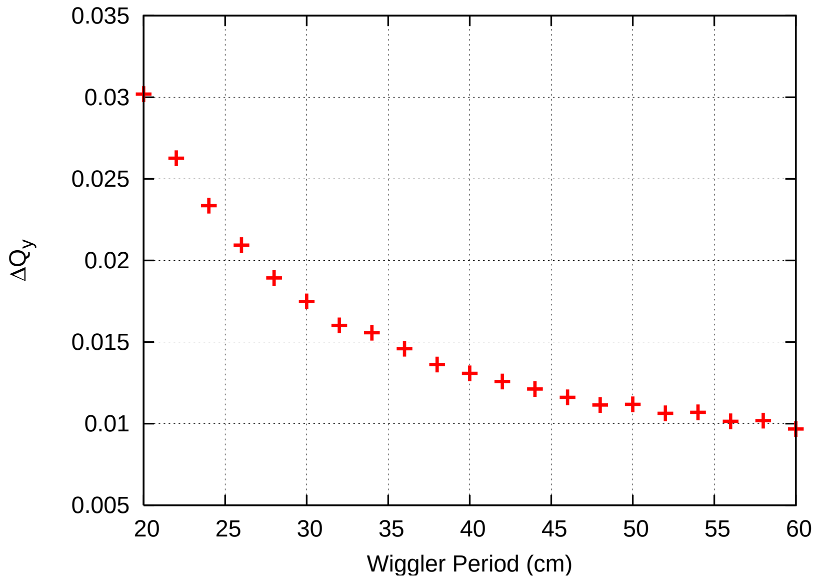

Figure 5.4: Example, from simulations with whole accelerator lattice, of inherent wiggler vertical tune shift as it grows with shorter period wigglers, for a beam at $y = 15\,\mathrm{mm}$.

only peaks to a value of B_0 at $(x, y) = (0, 0)$, as x increases $B_y(x)$ decreases, or rolls-off, from B_0. This causes horizontally offset particles to experience different forces, and similarly for vertically offset particles. Again the wiggling trajectory is critical, because even a particle which enters the magnet at $(x, y) = (0, 0)$ will be displaced horizontally from the central axis as it wiggles and will experience the vertical field horizontal roll-off.

This combination of vertical field horizontal roll-off and horizontal orbit variation produces an additional vertical component to the field. This causes a variation in the horizontal orbit that depends on the variation of the vertical field. The dominant effect is a horizontal tune shift that grows according to [19]:

$$\Delta Q_x \propto B_0 \lambda_w^2 \frac{\partial^2 B_y}{\partial x^2}. \tag{5.16}$$

The variation of the $B_y(x)$ is typically quadratic (see Figure 5.5), so this nonlinearity is quantified by the deviation of the field from peak at some reference position.

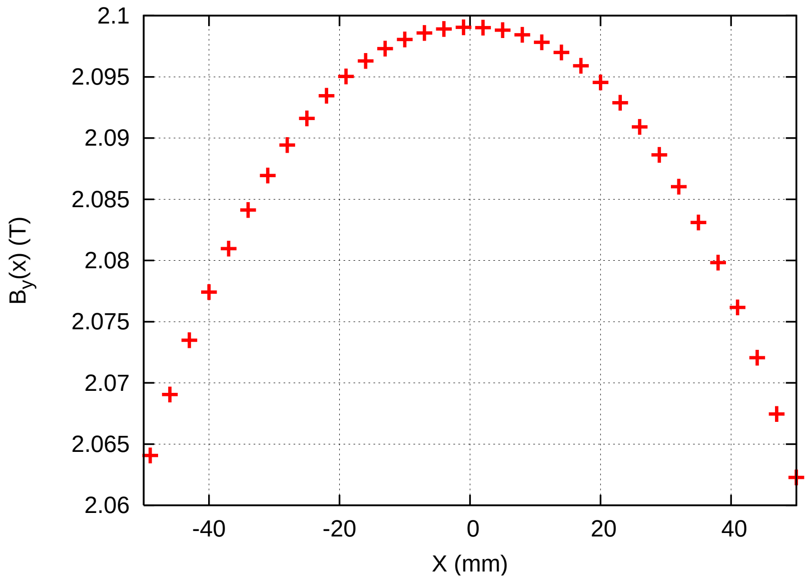

Figure 5.5: Example of the quadratic roll-off of the vertical magnetic field observed with increasing horizontal position in a 2.1 T wiggler.

This is called the field quality and is commonly defined as the field roll-off at 10 mm, $\Delta B/B_0$ at $(x, y, z) = (10\,\text{mm}, 0, \lambda/2)$. Therefore, this nonlinearity causes a horizontal tune shift that depends on the horizontal amplitude of the particle (see Figure 5.6).

This effect is usually weaker than the inherent vertical nonlinearity but it can still cause a significant impact on the performance of the accelerator. Therefore, wigglers are designed and constructed which minimize this effect by having very little field horizontal roll-off. This is done by making the wiggler pole width, w_p, large and the pole gap, g_p, small. Since the field goes to zero outside of the poles, widening the poles reduces the variation of the field and hence the horizontal tune shift (see Figure 5.7). An alternative to widening the poles to reduce the field roll-off is to add shims on the horizontal edges of the pole faces, or cut-out the horizontal center of the pole faces. This enhances the ability of the iron poles to amplify the magnetic field at large amplitudes, thereby achieving a reduced vertical

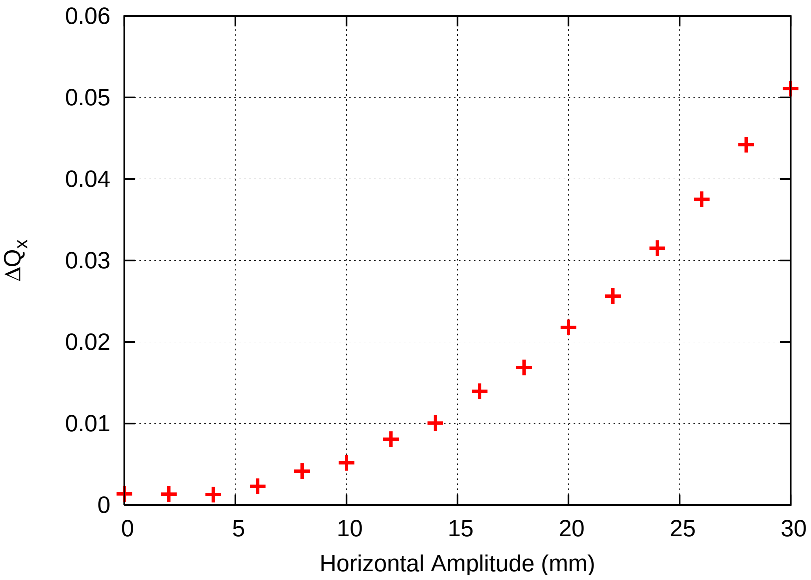

Figure 5.6: Example, from simulations with whole accelerator lattice, of horizontal tune shift from a realistic wiggler model as it grows with the beam's horizontal position, for a wiggler with width= 94 mm and $\Delta B/B_0 = 1.1\,\%$ at $x = 10\,\mathrm{mm}$.

field horizontal roll-off without a wider wiggler.

It is important to note that the inherent wiggler nonlinearity produces a vertical tune shift with amplitude that grows with shorter periods, while this effect produces a horizontal tune shift with amplitude that grows with longer periods. Optimizing the wiggler period to balance these two nonlinearities is an important step in designing a wiggler which will have minimal negative impact on the beam dynamics.

There are more nonlinearities in realistic wigglers than just this horizontal tune shift. In fact, there are additional higher-order terms in Equations 5.15 and 5.16 that have been neglected. Errors in construction, like pole misalignments, can also produce nonlinear dynamics that are not known until a wiggler is actually constructed and operational. Thus, detailed computer simulations are required to measure the wiggler's impact on the beam and then suggest changes to the design

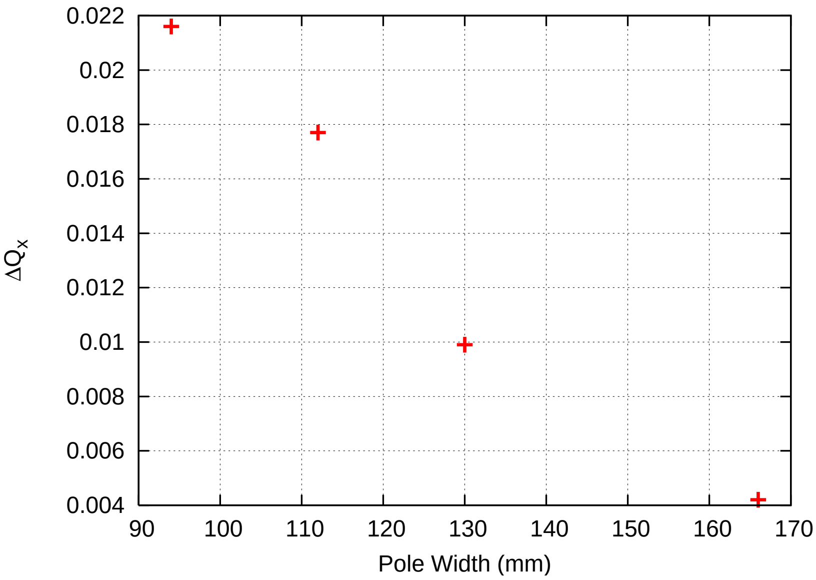

Figure 5.7: Example, from simulations with whole accelerator lattice, of horizontal tune shift from a realistic wiggler model as it grows with wigglers having an increasing field roll-off coming from narrower poles, for a beam at $x = 20\,\mathrm{mm}$.

to minimize the negative impact before it is constructed. Additionally, extreme care is required in the construction of a wiggler to prevent additional field errors.

5.3 Uses in Damping Rings

Wigglers are required in the ILC damping rings to increase the rate of synchrotron production and reduce the beam emittance quickly, but if they are not designed optimally, wiggler nonlinearities can have a severe impact on the damping ring's performance. With an optimized design, adding wigglers can quickly reduce a ring's damping time without serious negative impact on the beam dynamics. Therefore, the ILC damping ring can have a circumference of 6 km and beam energy of 5 GeV and still achieve a damping time of 25 ms as long as it has well-designed wigglers.

Achieving a damping time of 25 ms with the ILC damping ring's energy (5 GeV) and circumference (6 km), requires that the beam lose 8.5 MeV per turn. With no wigglers, such a ring loses 0.5 MeV per turn and takes nearly 500 ms to damp the beam emittance by $1/e$, in $\tau_{damp} = 500\,\mathrm{ms}$. Clearly, this damping ring will require a number of wiggler magnets to achieve the required damping rate.

Adding wigglers to decrease the damping time (Equation 4.2) can be represented mathematically by adding the bending of the wigglers to the bending of the dipoles in the I_2 integral, $I_{2,tot} = I_{2,dipoles} + I_{2,wigglers}$. Plugging Equation 5.1 into Equation 2.11 yields the relationship:

$$I_{2,wigglers} \approx \frac{1}{2} L_{w,tot} B_0^2. \tag{5.17}$$

Thus, in a ring where the emission of synchrotron radiation is dominated by wigglers and not dipoles, the damping time is given by [2]:

$$\tau_{damp} \propto \frac{1}{L_{w,tot} B_0^2}. \tag{5.18}$$

In the ILC damping ring, approximately 200 meters of $B_0 \approx 2\,\mathrm{T}$ wiggler magnets would be needed to achieve $\tau_{damp} = 25\,\mathrm{ms}$.

The length of wigglers in the damping ring could be reduced to save money while keeping the damping time fixed by raising the peak field, but this comes at the prize of stronger nonlinearities. The inherent and realistic wiggler nonlinearities will reduce the dynamic aperture through amplitude-dependent tune shifts that can cause the beam to cross tune plane resonances. Additionally, to achieve a higher peak field the physical aperture in the ring may be reduced. The physical aperture is set according to the strength of the magnet–narrowing the vertical gap between the poles allows weak poles to achieve a high peak field, but at the cost of the physical aperture.

The desire to meet the target dynamic and physical apertures is not the only motivation for keeping the wiggler field low. Like radiation damping and the I_2

integral, the amount of quantum excitation and the value of the I_5 integral in the ring are also increased when wigglers are inserted into the lattice. This will result in changes to the radiation equilibrium horizontal emittance and the energy spread of the beam. Since the I_5 integral depends on the energy dependent orbit, or dispersion, at the location of the radiation emission, wigglers will change a beam's energy spread and horizontal emittance differently depending on the value of the dispersion in the lattice.

If wigglers are placed in a location with dispersion, then the I_5 integral will increase and the energy spread and horizontal emittance will equilibrate at a value determined by the balance of radiation damping and quantum excitation. In a ring where the majority of radiation comes from wigglers, the radiation equilibrium energy spread is related only to the wiggler field as given by [20]:

$$\sigma_\delta \propto \sqrt{B_0}, \tag{5.19}$$

and the radiation equilibrium horizontal emittance is given by:

$$\epsilon_{x,rad} \propto B_0 \mathcal{H}, \tag{5.20}$$

with $\mathcal{H}$ depending on the dispersion in the ring, as given in Equation 2.14.

However, even with no dispersion in the region around the wigglers, quantum excitation will still prevent radiation damping from reducing the emittance and energy spread all the way to zero because wigglers themselves generate dispersion. Since dispersion comes from bending, wigglers internally generate dispersion even if there is no dispersion in the section of the ring without the wigglers. The slope of the wiggler-generated dispersion is related to the slope of the wiggling trajectory so $\eta' \propto \Theta \propto \lambda_w B_0$. Inserting this into Equation 2.14 yields $\mathcal{H} \approx \beta_x(\lambda_w B_0)^2$ because η is small and the contribution of η' to $\mathcal{H}$ dominates. Finally, inserting this expression into Equation 5.20 gives the impact on the radiation equilibrium horizontal emittance in a wiggler dominated ring where the wigglers are located in zero-dispersion straight sections [2]:

$$\epsilon_{x,rad} \propto \beta_x \lambda_w^2 B_0^3. \tag{5.21}$$

Combining these results with the dependence of the damping time on the wiggler parameters reveals that while a stronger wiggler field will result in the beam emittance damping faster, it will also result in the beam emittance and energy spread not being damped to as small of a value.

From these relationships, it is clear that wigglers alter the fundamental properties of circular accelerators and result in changes to many of the beam's parameters. Depending on the choice of peak field, gap height, pole width, and period, wigglers can modify the beam's horizontal emittance and energy spread and the lattice's damping rate, physical aperture, and dynamic aperture. Detailed simulations and calculations are required to set each wiggler parameter to a value that meets as many of the beam and lattice parameters at once as possible.

5.4 Wiggler Simulation Techniques

Computer simulations are critical tools for predicting the behavior of a proposed particle accelerator so that the design can be modified to maximize its performance before it is actually built. Computer simulations are used by the ILC damping ring lattice designers as a feedback loop, allowing them to test one version of the lattice then recommend and quickly implement the next version of the lattice. This is particularly true for the design of the damping ring wigglers, because minimizing one beam parameter, like the beam emittance, can require changing the characteristics of the wiggler magnets in a way that negatively impacts another beam or ring parameter, like the dynamic aperture. Thus, during magnet design studies, particle tracking simulations are critical for evaluating the impact of a specific magnet design on the target beam and lattice parameters.

5.4.1 Particle Tracking

The most basic and useful method of accelerator simulation is to create a computer model of the accelerator lattice and determine the trajectory of particles through the lattice. Bmad [21] is a library of computer programs that is used for the simulation of relativistic charged-particle dynamics in circular and linear high energy particle accelerators [22]. Bmad can track individual particles or beams of particles through lattice elements such as dipoles, quadrupoles, higher-order magnets, wigglers, RF cavities, and arbitrary electromagnetic fields. Bmad includes the effects of the beam-beam interaction, space charge, radiation damping, and quantum excitation during calculations of the particle trajectories and other beam and lattice parameters.

Dipoles, quadrupoles, and other accelerator elements produce simple enough electromagnetic fields, that an analytic expression can determine their influence on a particles' trajectory using only information like the length and strength of the elements. However, wiggler fields are too complex to parameterize particle trajectories with simply the length and strength of the magnet. Therefore, the exact behavior of $\mathbf{B}(x, y, z)$ in a wiggler is used to calculate the precise trajectory of a particle through the wiggler magnet.

If $\mathbf{B}(x, y, z)$ can be expressed analytically, then a Taylor series expansion of the particle's trajectory through the field, or a Taylor map, can be generated. If

$\mathbf{B}(x, y, z)$ is only known at discrete points and an analytic equation cannot be written for the field, then the trajectory of a particle can be determined through Runge-Kutta integration from one discrete step to the next. There are trade-offs between tracking with a Taylor map or with Runge-Kutta integration. A Taylor map is much faster, but the analytic expression of $\mathbf{B}(x, y, z)$ is only approximate, leading to a result that is not as accurate as Runge-Kutta. A comparison of the wiggler trajectories calculated using a Taylor map versus Runge-Kutta integration confirms that the accuracy of Taylor tracking is sufficient for wiggler simulation needs [23].

The wiggler modeling in Bmad was developed at Cornell when wigglers were being studied and developed for use in the Cornell Electron Storage Ring (CESR) in the late 1990's and early 2000's [23]. Therefore, Bmad provides a practical and useful collection of diverse diagnostic tools for wiggler modeling. One such tool is the ability to use different wiggler representations that are based on increasingly nonlinear models. Switching between more simplified and more complex wiggler models allows a computer simulation to reveal the impact of the different types of wiggler nonlinearities on the beam. A full nonlinear wiggler model, an ideal nonlinear linear wiggler model, and a completely linear wiggler model are available in Bmad.

Model A: Linear Wiggler

The simplest wiggler model available is a purely linear wiggler model which is composed of a series of alternating dipole magnets. The alternating bend field focuses and damps the beam as a real wiggler does; however, the poles of the dipoles do not give an accurate wiggler field with longitudinal components and field roll-offs.

This results in the linear wiggler model omitting the nonlinear beam dynamics that would come from a real wiggler magnet. Nevertheless, the linear wiggler model is useful for damping ring studies, because it allows the evaluation of the performance of the ring while ignoring the complication of the wiggler nonlinearities, thus giving the baseline performance of the ring.

Model B: Ideal Nonlinear Wiggler

The next more complex wiggler model includes some, but not all, of the wiggler nonlinearities. This wiggler model is equivalent to the infinitely wide and infinitely long wiggler magnet described in Section 5.2.1 so it does have a longitudinal field component. This model includes the effects of the linear wiggler model plus quadrupole-like focusing and the vertical octupole term intrinsic in all wiggler magnets.

Since this model includes the dominant nonlinearity but none of the nonlinearities that only come from a realistic wiggler, this is called the ideal nonlinear wiggler model. This model is useful for determining how the dominant octupole-like nonlinearity degrades the baseline performance of the ring. This model only requires B_0, λ_w, and the number of poles to calculate particle trajectories, so it does not depend on the precise arrangement of wiggler poles in a specific magnet design. Therefore, the ideal nonlinear wiggler model gives the ring performance that would be expected if the wiggler poles were designed perfectly to minimize as many non-inherent nonlinearities as possible.

Model C: Full Nonlinear Wiggler

The most complex wiggler model is a Taylor map generated from an approximate analytic expression of the exact wiggler field. Since this model is based on a realistic wiggler field, it includes all of the wiggler nonlinearities of a realistic wiggler and is called the full nonlinear wiggler model [23]. The full nonlinear wiggler model includes the nonlinearities of the ideal nonlinear model plus those coming from a realistic wiggler magnet with finite width poles, end poles, and fringe fields.

The exact wiggler field used depends on the specific shape, size, and arrangement of poles for a specific wiggler design. Thus, comparing a full nonlinear model to an ideal nonlinear model reveals the impact of a wiggler's pole design on the optimal performance of the beam dynamics which can lead to redesigning the wiggler poles. For example, Figure 5.8 shows how the three different tracking models incorporate varying amounts of the wiggler tune shifts. The linear wiggler model produces no horizontal or vertical tune shifts as the vertical amplitude of the particle increases. The ideal nonlinear wiggler model incorporates the inherent wiggler nonlinearity which provides a majority of the total vertical tune shift and no horizontal tune shift. Finally, the full nonlinear wiggler model produces all of the horizontal tune shift coming from finite width poles and a vertical tune variation that adds to the effect of the inherent wiggler nonlinearity.

5.4.2 Generating the Magnetic Field

Wigglers with slightly different pole shapes or arrangements can have totally different fields resulting in completely different particle trajectories. Thus, the first step in performing wiggler tracking studies with the full nonlinear wiggler model is to determine the exact magnetic field coming from the specific wiggler under

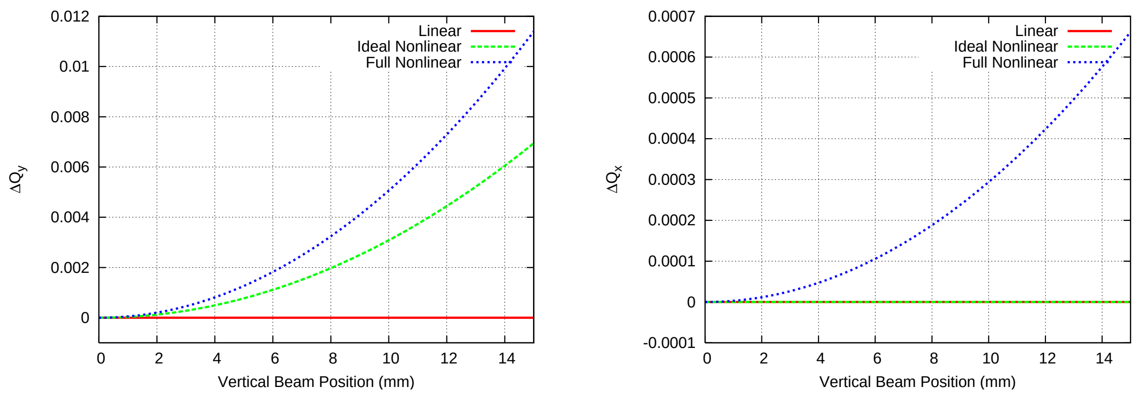

Figure 5.8: Comparison of wiggler tracking models.

investigation.

Wiggler magnets can be composed of permanent magnets or electromagnets, therefore the **B**-field comes from combinations of field sources and current sources. Finite element analysis and similar techniques are used to approximate the magnet as a finely discretized mesh of individual field and current sources, allowing the entire magnet's field to be solved through a system of equations. Common finite element analysis codes for 3-D magnet modeling are OPERA-3d [24] and Radia [25]. These programs allow the user to graphically assemble the wiggler poles and coils in the same arrangement as the real magnet (whether the magnet has been actually built or is just proposed, see Figure 5.9) and then output the value of the magnetic field on a table of (x, y, z) points.

These models include the intricate design components of a real wiggler, including features like the size and curvature of the poles, the horizontal width and vertical gap of the poles, pole shims or cut-outs, end poles of various sizes, wire dimensions, and the saturation of the magnetic material. The resulting magnetic field table includes all of the details of a real field and can be used to determine the exact impact of such a field on the accelerator's performance.

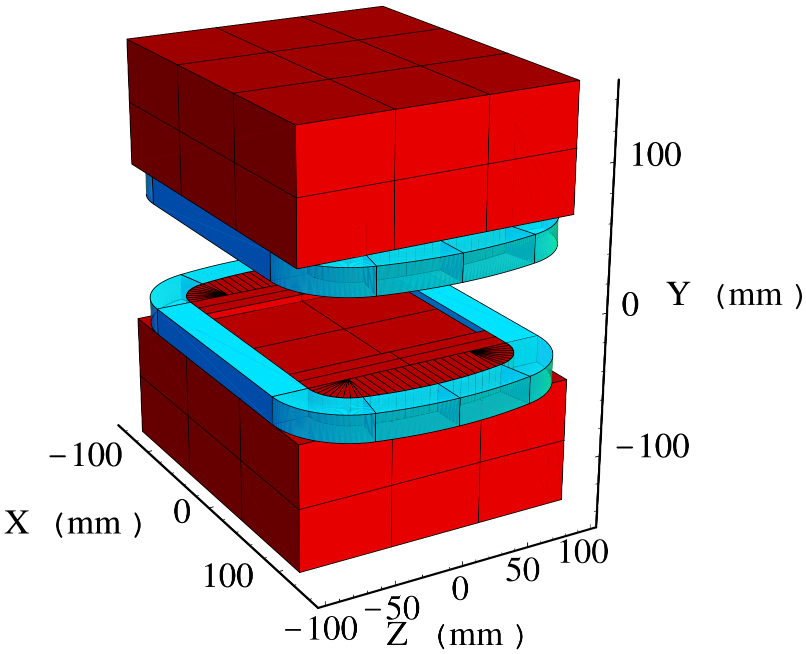

Figure 5.9: A set of wiggler poles with coils, in Radia.

5.4.3 Fitting the Magnetic Field

For Taylor map tracking, calculating derivatives from discrete data is inaccurate and the field table cannot be directly tracked through [23]. Therefore, to quickly and accurately calculate all order derivatives needed to create a reliable Taylor map, the discrete data must be represented by a functional form. Deriving an analytic equation for the fields in a wiggler magnet is not possible for realistic fields; however, a harmonic expansion of the fields is possible using the Halbach approximation [26]. The Halbach approximation extends Equation 5.9 to the x dimension with additional sinusoidal and hyperbolic terms and incorporates the higher order field harmonics. The higher order field harmonics describe how uniform and how sinusoidal the magnetic field is and determine the strength and form of the realistic nonlinearities unique to each wiggler magnet.

At Cornell, a field model has been developed based on the Halbach approximation in Cartesian coordinates [23]. In the Cornell model, the Halbach approximation is extended by performing an iterative fit which varies the wavenumbers and the field strength,

$$\mathbf{B}_{fit} = \sum_{n=1}^{N} \mathbf{B}_n(x, y, s; C_n, k_{xn}, k_{sn}, \phi_{sn}, f_n), \tag{5.22}$$

to minimize a merit function, M, given by the difference between the fit and the data:

$$M = \sum_{data} |\mathbf{B}_{fit} - \mathbf{B}_{data}|^2. \tag{5.23}$$

It is important to note that this fitting procedure does not require the wavenumber to be directly related to the period ($k_n \neq 2\pi n/\lambda$). Allowing the wavenumbers to vary minimizes the total number of terms needed in the summation, and provides a result which represents a non-periodic longitudinal field. This is required in wigglers where λ_w is different for the end poles and the central poles so that the second field integral and the outgoing trajectory offset are zeroed.

The Cornell wiggler fitting model is described by three sets of functions that each describe the wiggler field appropriately over a different range of wavenumbers. When $k_{xn} > 0$ then $f_n = 1$ selects the following set of functions:

$$\begin{aligned} B_x &= -C\frac{k_x}{k_y}\sin(k_x x)\sinh(k_y y)\cos(k_s s + \phi_s), \\ B_y &= C\cos(k_x x)\cosh(k_y y)\cos(k_s s + \phi_s), \\ B_z &= -C\frac{k_s}{k_y}\cos(k_x x)\sinh(k_y y)\sin(k_s s + \phi_s), \\ & \quad k_y^2 = k_s^2 + k_x^2. \end{aligned} \tag{5.24}$$

Note that this expression is equivalent to Equation 5.9 for the specialized case of $x = 0$, $C = B_0$, and $k_s = k_y$. When $-|k_{sn}| \leq k_{xn} \leq 0$ then $f_n = 2$ selects the next set of functions:

$$
\begin{aligned}
B_x &= C\frac{k_x}{k_y}\sinh(k_x x)\sinh(k_y y)\cos(k_s s+\phi_s),\\
B_y &= C\cosh(k_x x)\cosh(k_y y)\cos(k_s s+\phi_s),\\
B_z &= -C\frac{k_s}{k_y}\cosh(k_x x)\sinh(k_y y)\sin(k_s s+\phi_s),\\
&\quad k_y^2 = k_s^2 - k_x^2.
\end{aligned} \tag{5.25}
$$

And when $k_{xn} < -|k_{sn}|$ then $f_n = 3$ selects the final set of functions:

$$
\begin{aligned}
B_x &= C\frac{k_x}{k_y}\sinh(k_x x)\sin(k_y y)\cos(k_s s+\phi_s),\\
B_y &= C\cosh(k_x x)\cos(k_y y)\cos(k_s s+\phi_s),\\
B_z &= -C\frac{k_s}{k_y}\cosh(k_x x)\sin(k_y y)\sin(k_s s+\phi_s),\\
&\quad k_y^2 = k_x^2 - k_s^2.
\end{aligned} \tag{5.26}
$$

The relations between the wavenumbers insure that the fields satisfy Maxwell's equations.

The result is a sum of sinusoidal and hyperbolic sinusoidal functions that represents the wiggler field at an accuracy corresponding to the precision of the fit. The precision of the fit (χ^2) depends on the number of terms in the fit and the length of time that the fitting program is allowed to run. Once completed, the field residuals between the field table data and the fit can be evaluated and the fit can continue if the quality of the fit is not sufficient for accurate particle tracking studies (see Figure 5.10). The field fit in this figure ran for multiple days and is typical for the fits utilized in this dissertation in regards to its number of terms (132), residuals to the data (less than a few Gauss on-axis), and quality of fit with the data ($\chi^2 = 0.002$).

The Cornell-developed Cartesian-based iterative fitting method was compared with the wiggler field fitting procedures used at other laboratories. Detailed results

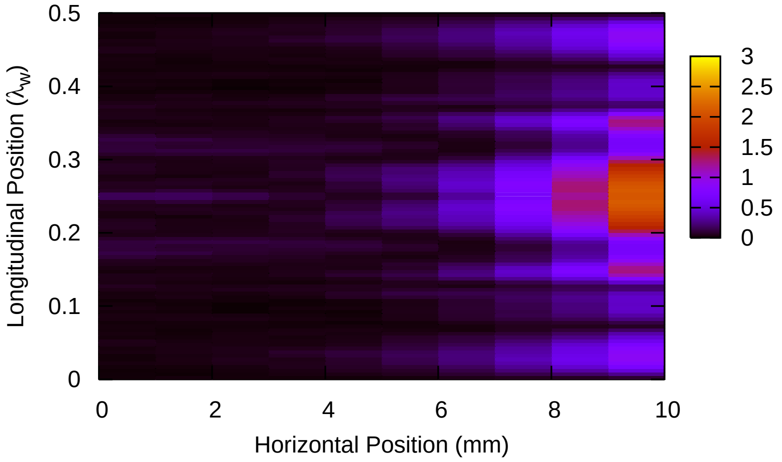

Figure 5.10: Vertical magnetic field residuals (in Gauss) between the fit and the data $(B_{y,fit}(x,z) - B_{y,data}(x,z))$, over one half period.

of these benchmark studies are in Appendix A. These benchmark studies showed strong agreement between the field fitting and wiggler tracking methods allowing wiggler simulation results to be compared between investigators and validating the results of all of the simulations.

5.4.4 Dynamic Aperture and Frequency Map Simulations

Once the magnetic field has been fit to an analytic expression, it can be used for particle tracking studies in Bmad. The two most common simulation tools used to characterize the performance of the accelerator are dynamic aperture and the frequency map analysis simulations.

Dynamic Aperture

The dynamic aperture is used to quantify the impact of wiggler nonlinearities on the beam. The size of the dynamic aperture is determined by the amplitude-dependent tune shifts which can push particles to unstable locations in the tune plane. Throughout this dissertation, the dynamic aperture is simulated with single particle tracking studies in Bmad that include longitudinal dynamics but ignore radiation effects. A particle is tracked through the accelerator for multiple revolutions, long enough for the particle to circulate for one damping time. If the particle is stable over one damping time then its initial displacement is increased and it is tracked again, this is repeated until the particle becomes lost during one damping time. The smallest initial displacement that is large enough to produce a trajectory that is unstable over one damping time defines the dynamic aperture of the accelerator.

Simulating the dynamic aperture of an accelerator lattice in this manner gives a baseline aperture for a ring with no errors or misalignments and only including the nonlinearities that are described in the theoretical models used in the tracking program. This is a best-case scenario as an actual accelerator is made of electromagnetic elements with construction errors that can be misaligned or even moving over time. The realistic errors in the elements of an accelerator produce magnetic field errors that couple to existing nonlinearities and drive the beam to nonlinear resonances and degrade the beam dynamics in ways that computer simulations cannot fully include.

In order to leave a sufficient margin of error to account for unanticipated deterioration of the ring's stable dynamics when the machine is actually constructed and operated, the target for a baseline lattice aperture during computer simulations is generally at least as large as ten times the maximum beam size. For the ILC damping rings the maximum beam size is the size of the positron beam at injection; therefore, it is hoped that if the ILC damping ring starts with $10 \times \sigma_{e+,inj}$ then the dynamic aperture will be large enough that realistic errors and misalignments will not limit the final dynamic aperture below approximately $5 \times \sigma_{e+,inj}$.

A more realistic simulation of the dynamic aperture is achieved for the ILC damping ring by using multipole field errors on the main ring magnets: the dipoles, quadrupoles, and sextupoles. The strength of the field errors used for these simulations were measured from the actual errors on the PEP-II and SPEAR-3 magnets and are given in Reference [12]. Since these errors include systematic and random effects, simulations are performed with 15 different configurations of the random errors on the magnets, or 15 random seeds. In the graphs of these results, the thick line is the average dynamic aperture result for the 15 seeds and the thin line is the minimum dynamic aperture result for the 15 seeds (see for example Figure 8.8).

Frequency Map Analysis

Frequency map analysis is a tool that is used to map the beam's movement in the tune plane and potentially explain degradation or growth of the dynamic aperture [27]. Like dynamic aperture studies, the frequency map analysis is performed with single particle tracking studies in Bmad that include longitudinal dynamics but ignore radiation effects. A single particle is tracked for τ_{damp} with an initial position defined by a dense grid of points in the $\pm x$, $+y$ plane. If a particle at a given amplitude is lost on the physical aperture within τ_{damp}, that initial position is left blank; if a particle at a given amplitude is not lost then its initial position has a point of a certain color or intensity (see for example Figure 8.5b). Thus, on a frequency map analysis plot, the boundary between the colored points and the white points defines the dynamic aperture.

However, the frequency map analysis provides further information about the beam dynamics than just the dynamic aperture. The color or intensity of the point is related to the tune of the particle. The rate of change of the horizontal or vertical tune from the first half of the damping time ($t = 0 - 1/2\,\tau_{damp}$) to the second half ($t = 1/2\,\tau_{damp} - \tau_{damp}$) is a measure of the chaoticity of the particle's orbit. The tune of the particle for the first half or second half of the damping time is calculated in the computer simulations by taking a Fourier transform of the particle's trajectory and locating the peak frequency [27]. A larger change in tune over time corresponds to a more chaotic orbit or an orbit that is near the aperture of stable beam dynamics. Therefore, the intensity of the points in the frequency map analysis plots is given by:

$$\text{Intensity} = \log\left(\sqrt{(\Delta Q_x^2 + \Delta Q_y^2)}\right), \tag{5.27}$$

where $\Delta Q_x = Q_{x,\,1^{st}\,1/2\,\tau_{damp}} - Q_{x,\,2^{nd}\,1/2\,\tau_{damp}}$, and similar for y. Small tune changes are indicated with darker colors and large tune changes with lighter colors (see for example Figure 6.4).

When the frequency map analysis is examined in physical space (x, y), the dark colors are located near the center of the guide field region (at $(x, y) = (0, 0)$) where amplitude-dependent tune shifts are weak. Lighter colors are located at large amplitudes just inside the dynamic aperture limit, this is where the tune shifts are strong enough that the tune is changing with time. These brightly colored points at the edge of the dynamic aperture also mean that if the amplitude is increased slightly the particle will cross the dynamic aperture, become chaotic, and be lost.

Finally, the frequency map analysis can be represented in tune space (Q_x, Q_y) and not just physical space (x, y). In tune space plots, the position of each particle is given by the value of the particle's tune in the first half of the damping time and the color is again related to the difference in tune from the first half to the second half, given by Equation 5.27. Particles at small amplitudes orbit the accelerator and experience few tune shifts, so the frequency of their betatron orbits stays at the operating point; therefore, in tune space plots, the largest density of dark colored points are located at and near the operating point of the machine. Lighter colored points are located farther away from the operating point because wiggler nonlinearities change the tune with position (given by the distance of a point from the operating tunes in the plot) as well as with time (give by the color of a point in the plot).

The position of all of the points in the tune plane create a tune "footprint" which describes the direction and size of tune shifts in the accelerator. A large tune footprint means that wiggler magnets are causing the horizontal and vertical tunes to change as the beam's horizontal and vertical position is increased. A large tune footprint will cross more tune resonances which increases the time rate of change of the tune and is shown by brightly colored points following the line of the tune resonances. The brightly colored points in the frequency map analysis can be located on both the tune space plots and the physical space plots to show how wiggler nonlinearities are shifting the beam to tune resonances and to large amplitudes. Thus, comparing the frequency map analysis in tune space and physical space can reveal which tune resonances are producing limitations in the dynamic aperture.

These simulation techniques will be utilized in the following chapter to create nonlinear models of two candidate ILC damping wigglers and then evaluate their performance in the baseline damping ring. Their performances will be simulated through dynamic aperture and frequency map analysis studies to determine how the unique characteristics of the two wiggler options result in different impacts on the beam dynamics of the ILC damping ring. In evaluating the unique aspects of the design and performance of the two candidate wiggler designs the conceptual design of an optimized wiggler will be achieved.

Chapter 6

Existing Wiggler Designs

Wiggler magnets are operating in particle accelerators around the world with a wide range of performance capabilities and magnet designs (see for example [28, 29]). However, only a small number of wigglers in the world actually provide the required beam parameters and meet the technical requirements of the ILC.

In this dissertation, the two most promising ILC damping wiggler options will be examined. The first is a proposed wiggler and the second is an existing wiggler: the proposed wiggler design [30] from the TESLA linear collider, and the Cornell wiggler [31] which is used in the Cornell Electron Storage Ring (CESR).

These two wigglers are well suited for a direct comparison of their potential performance in the ILC damping ring because they have some of the same wiggler parameters but differ in some very important ways. The largest difference between these two magnets is their technology; the TESLA wiggler design is permanent magnet and the CESR wiggler is a superconducting magnet. Comparing these two wiggler options highlights the critical decision of which technology option should be used in the ILC damping wiggler.

6.1 TESLA Permanent Magnet Wiggler

The TESLA collaboration developed a damping wiggler prioritizing compact-size and ease of operation. They chose a permanent magnet instead of an electromagnet because as a passive device it would not need a power supply and would result in negligible operating costs and maintenance needs [32]. The TESLA wiggler is actually a hybrid permanent magnet wiggler, with iron poles in the center to

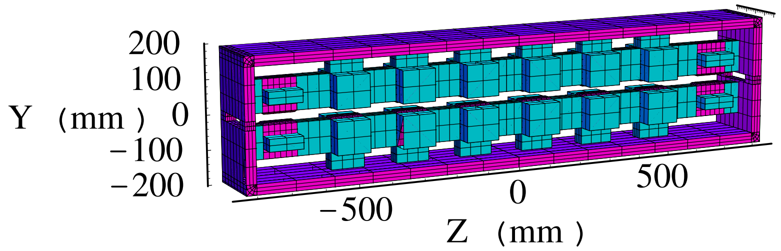

Figure 6.1: The TESLA permanent magnet wiggler. The permanent magnet material, NdFeB, surrounds the iron poles in the center, all of which are enclosed in an iron yoke.

reinforce the field coming from the neodymium, iron, and boron magnets (NdFeB) surrounding the poles (see Figure 6.1) [30].

The TESLA wiggler has $\lambda_w = 400\,\mathrm{mm}$ and $g_p = 25\,\mathrm{mm}$ and the hybrid permanent magnet structure was built within those constraints (see Table 6.1). The resulting magnet structure would produce a 1.67 T peak field ($B_{rms} = 1.17\,\mathrm{T}$) with a non-sinusoidal vertical field profile (see Figure 6.2). With that field strength, 108 wigglers, over 400 m, were required to achieve a 25 ms damping time in the TESLA dogbone ring.

6.1.1 Principles of Design

The TESLA damping ring was designed with all of its wigglers in a 400 m straight section (see Figure 4.2), with the wigglers hung from the ceiling of the tunnel that the damping ring would share with the main linac. Because of this configuration, a premium was placed on compact wigglers. Additionally, in order to minimize the total cost of 400 m of wigglers the design aperture was chosen to be only as large as required to fit the beam [30].

Table 6.1: Physical specifications of the TESLA wiggler.

Parameter	**Unit**	**Value**
Peak Field	T	1.67
Number of poles		18
Total length	m	3.6
Period	m	0.4
Pole Width	cm	6.0
Gap Height	cm	2.5
$\Delta B/B_0$ at $x = 10\,\text{mm}$		5.7×10^{-3}
Beam Energy	GeV	5

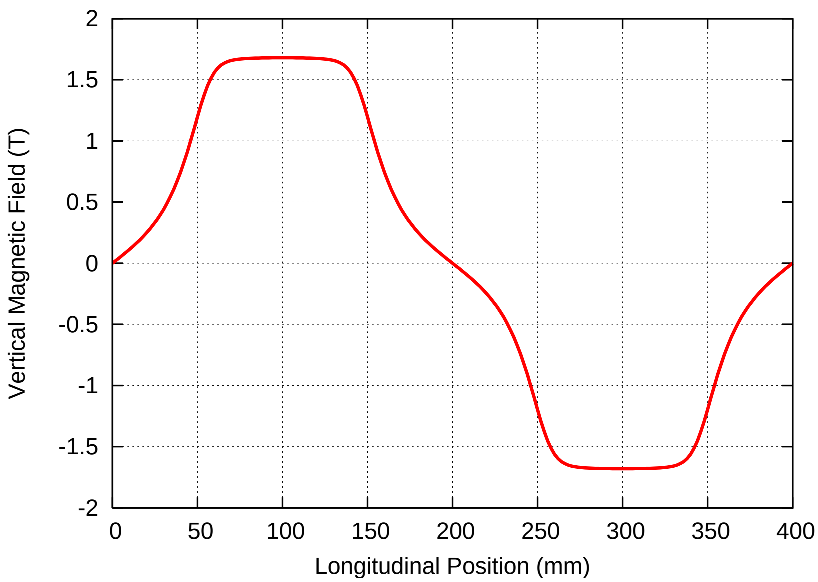

Figure 6.2: Vertical magnetic field profile on-axis $(x, y) = (0, 0)$ coming from the TESLA wiggler.

The pole width was initially set at 40 mm to be as narrow as possible while achieving a field quality of $\Delta B/B_0 = 4 \times 10^{-2}$ at $x = 10$ mm, which previous studies had concluded would be sufficient [33]. However, further studies by the TESLA collaboration determined that such a large field horizontal roll-off was not sufficient and the TESLA baseline wiggler was widened to 60 mm in order to achieve $\Delta B/B_0 = 5.7 \times 10^{-3}$ at $x = 10$ mm which was hoped to improve the simulated beam dynamics [34].

6.1.2 Simulated Performance in ILC

Bmad is one of the only accelerator simulation programs in the world that has the capacity to generate a full nonlinear wiggler model. Thus, the Bmad simulations performed for this dissertation were one of the first to examine the complete and realistic impact of the TESLA wiggler on the TESLA damping ring. These simulations began with the linear wiggler model to establish the ring's baseline performance, without the extra complication of wiggler nonlinearities. Then, the ideal nonlinear and full nonlinear wiggler models were inserted in the ring to look at the specific impact the wigglers had on the ring's performance. The magnetic field used in Bmad to generate a full nonlinear model of the TESLA wiggler came from a Radia model generated by DESY [35].

With the linear wiggler model, the on-energy dynamic aperture of the TESLA dogbone damping ring is approximately 6 times the injected positron beam size (see Figure 6.3). The ideal target of the TESLA damping ring dynamic aperture is over 10 times the size of the positron beam injection so that the operational realities of misalignments and field errors do not push the dynamic aperture below 3-5 times the injected beam size. Therefore, this ring's linear wiggler dynamic aperture is not

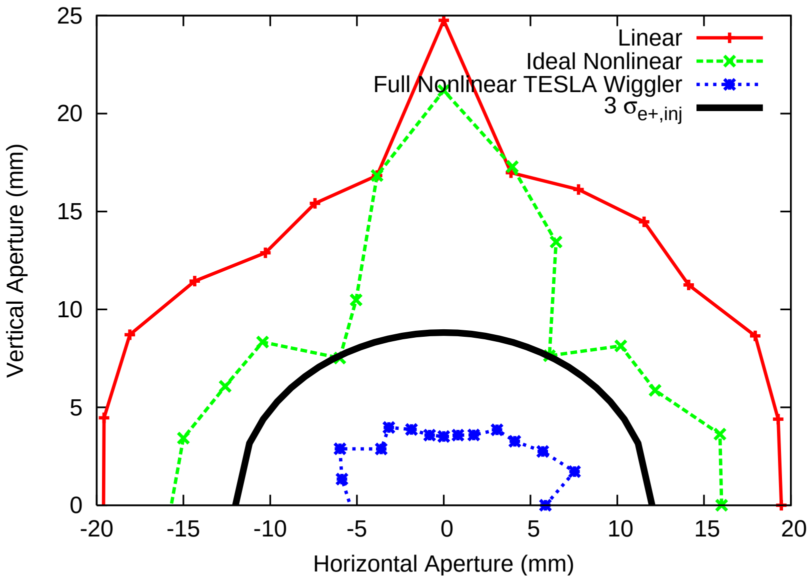

Figure 6.3: Dynamic aperture results for the linear, ideal nonlinear, and full nonlinear models of the TESLA wiggler in the TESLA damping ring.

very large to begin with and will only become smaller when multipole field errors and magnet misalignment errors are included as will happen in actual operation.

Before all of the other realistic errors are included in the lattice, it is important that a nonlinear wiggler not further compromise the ideal lattice's dynamic aperture. Unfortunately, including the full TESLA wiggler in tracking studies does yield a much smaller dynamic aperture and much larger tune spread with amplitude. The full nonlinear wiggler model yields a dynamic aperture between $1-2\times\sigma_{e^+,inj}$ which would result in excessive beam loss (see Figure 6.3). Figure 6.4 reveals that the poor dynamic aperture is due to the large tune footprint of the TESLA wiggler. The tune plane shows that the TESLA wiggler causes the beam to spread over half an integer in horizontal and vertical tune. Such a large spread makes the damping ring impossible to operate without crossing many resonances that can blow up the amplitude of stable particles and cause them to be lost. Thus, this wiggler design has strong amplitude-dependent tune shifts that are causing

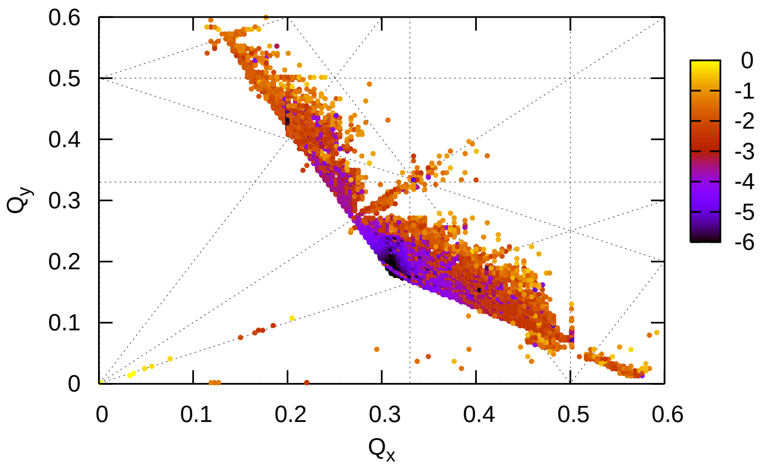

Figure 6.4: Frequency map analysis result in tune-space for the full nonlinear model of the TESLA wiggler in the TESLA damping ring. Operating point is $Q_x = 0.31$, $Q_y = 0.18$.

the particles to cross many resonance lines as they grow in amplitude, resulting in a smaller dynamic aperture.

Figure 6.3 reveals that with the ideal nonlinear wiggler model, the dynamic aperture is larger than the full nonlinear aperture and is close to the linear wiggler aperture. This suggests that the nonlinearities inherent in a wiggler can be accommodated by the TESLA damping ring design without sacrificing the ring's dynamic performance; but the nonlinearities coming from the specific shape and arrangement of the poles in the TESLA wiggler design result in reduced performance of the TESLA damping ring.

In addition to the dynamic aperture, the wiggler sets the limiting physical aperture in the dogbone ring. The TESLA wiggler has a vertical pole spacing of 25 mm. Such a small aperture would result in a reduced wiggler cost, however it corresponds to a half-aperture of only $2.1 \times \sigma_{e^+,inj}$ in the TESLA positron damping

Table 6.2: Wiggler-related lattice parameters in the TESLA damping ring lattice, using the full nonlinear model of the TESLA wiggler.

τ_{damp}	30.2 ms
$\epsilon_{x,rad}$	2.10 nm · rad
σ_δ	0.13 %

ring. This physical aperture is extremely small and has the potential to cause significant beam loss leading to magnet irradiation and luminosity degradation.

Using the full nonlinear model of the TESLA wiggler, also shows the impact the TESLA wiggler has on the beam parameters as the particles are extracted from the TESLA damping ring (see Table 6.2). The TESLA damping ring lattice was designed with 108 18-pole, 3.6 m wigglers placed in dispersion-free straight-sections to achieve the damping time with minimal quantum excitation generated emittance growth. With this model of the TESLA wiggler, the damping time is 30 ms, not quite meeting the target that was specified for the TESLA damping ring of 28 ms, the energy spread meets the 0.13 % TESLA target and the equilibrium horizontal emittance misses the 0.6 nm · rad target. The damping time and emittance targets could be easily achieved with slightly longer wigglers but this modification to the TESLA lattice was not performed in this study.

6.1.3 TESLA Wiggler Conclusions

From the results of these and other simulations [36, 37], it is clear that the TESLA wiggler design imposes severe dynamic and physical aperture limitations on the TESLA dogbone damping ring. It is anticipated, that the TESLA wiggler would produce similar aperture limitations if it were used in the ILC damping ring.

Therefore, the TESLA wiggler is not an acceptable candidate for the ILC damping wiggler unless it were to be redesigned.

Since the full nonlinear dynamic aperture is significantly smaller than the ideal nonlinear aperture, the TESLA wiggler could potentially be redesigned to increase the full nonlinear aperture. The design of the TESLA wiggler is in many respects not optimized so its poor beam dynamics is not unexpected [35]. The permanent magnet wiggler described above was created for a cursory comparative analysis with an electromagnetic design and was not completed to the full extent required for achieving optimal damping ring performance [30].

For example, wider magnet poles would decrease the field roll-off and improve the dynamic performance of the full nonlinear wiggler model in the ILC damping ring. In addition to meeting the dynamic aperture, if the pole spacing was raised the TESLA wiggler design would avoid an unacceptable amount of beam loss and would provide the required physical aperture.

6.2 CESR-c Superferric Wiggler

A thorough design effort was conducted at Cornell leading to the decision to install twelve superconducting damping wigglers in CESR [38]. The results of this work and the ensuing wiggler installation and operation have received international recognition. Wiggler studies performed at other accelerator laboratories are frequently measured against the standard set by the CESR wigglers. Therefore, the Cornell superconducting wigglers are a promising candidate for the ILC damping wigglers.

Twelve 2.1 T superconducting wigglers have been designed [31], fabricated [39, 40], tested [41], simulated [23, 42], and operated [43, 44] at Cornell University's

Table 6.3: Physical specifications of the CESR-c wiggler.

Parameter	**Unit**	**Value**
Peak Field	T	2.1
Number of poles		8
Total length	m	1.3
Period	m	0.4
Pole Width	cm	23.8
Gap Height	cm	7.6
$\Delta B/B_0$ at $x = 10\,\mathrm{mm}$		7.7×10^{-5}
Coil Current	A	141
Beam Energy	GeV	2

Laboratory for Elementary Particle Physics. These wigglers were required in order to operate CESR in a low-energy CESR-c configuration for the CLEO experiment's current research program to study charmonium resonances around $E_{COM} = 3\,\mathrm{GeV}$ [38].

The CESR-c wigglers are hybrid superconducting magnets with a magnetic field produced by superconducting wires and amplified by iron pole cores; this type of magnet is called a superferric magnet. The superconducting material is an alloy of Niobium and Titanium (NbTi) that is cooled to 4.2 K. With superferric technology, a field strength of $1.7 - 2.1\,\mathrm{T}$ is achievable over a significant portion of the 238 mm pole width and 76 mm gap height (see Table 6.3).

The CESR-c wigglers have eight total poles, with four central poles and two end poles on each side (see Figure 6.5). The central poles have a length of 200 mm, giving a wiggler period of 400 mm. The end poles are shorter, 150 and 100 mm

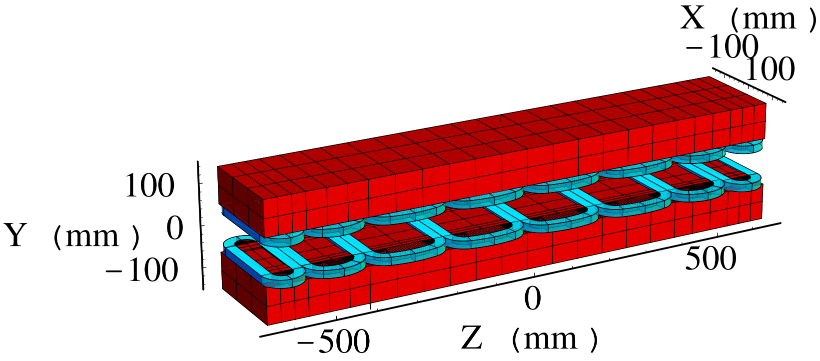

Figure 6.5: The 8-pole CESR-c wiggler shown with iron poles and NbTi coils.

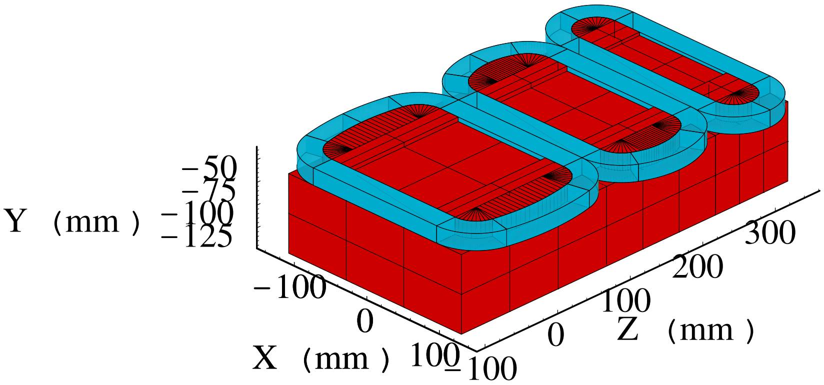

Figure 6.6: 20, 15, and 10 cm end poles used on the 8-pole CESR-c wiggler to eliminate the position offset in particle trajectory.

(see Figure 6.6), to zero the position and angle offset coming out of the wiggler for a particle entering on-axis. This gives the CESR-c wigglers a total length of 1.3 m to transition smoothly from zero field to ± 2.1 T and back to zero field (see Figure 6.7).

The CESR-c wigglers were decided to be 8-pole after prototypes with an odd number of poles, 7, and an even number of poles, 8, were constructed and experimentally compared. One difference in these two wiggler design options is that an even pole wiggler produces a vertical magnetic field integral that does not depend

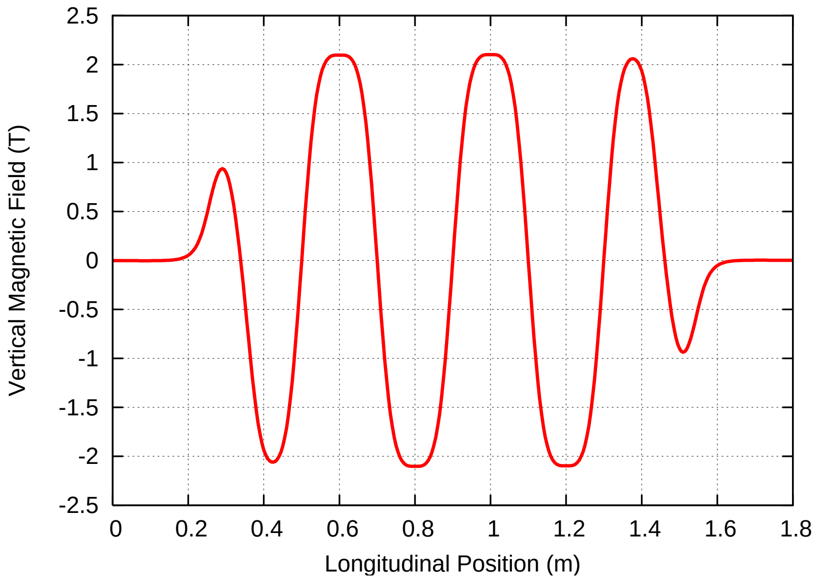

Figure 6.7: Vertical magnetic field profile on-axis $(x, y) = (0, 0)$ coming from the CESR-c wiggler.

on systematic errors in the poles, either in construction or position. Additionally, through experiments and simulations, the CESR-c wiggler designers determined that the field integral of an even pole wiggler was independent of the current in the superconducting coils. These benefits arise because with an even number of poles the integral of the vertical field from each pole is canceled by an identical pole at the opposite end of the magnet with the opposite polarity. The cancellation is not as simple with an odd number of poles, thus resulting in a less flexible range of operation for the 7-pole wigglers and the choice of 8 poles for the CESR-c wigglers [41].

6.2.1 Principles of Design

One of the features of CESR that drove the size of the wigglers was the "pretzel" orbits used during CLEO colliding-beam conditions. The pretzel describes the intertwined oscillations which the electron and positron beams experience after

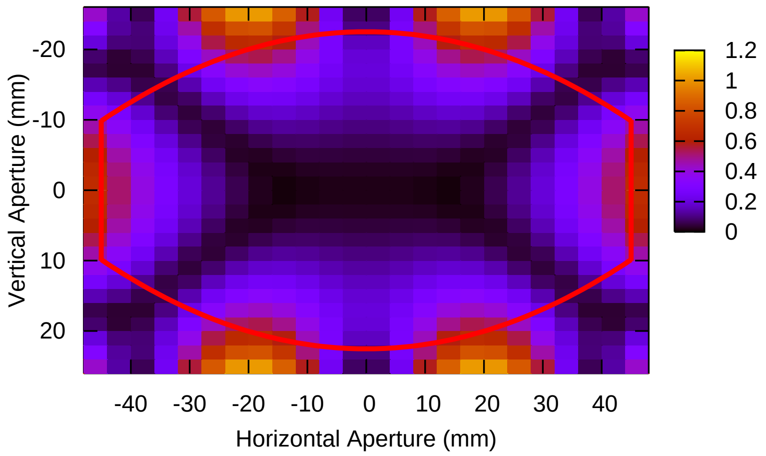

Figure 6.8: Fractional deviation of the wiggler field from B_0 ($\Delta B_y(x, y)/B_0$, %), over the entire region of the CESR beam pipe (solid black line).

passing through horizontal and vertical electrostatic separators in CESR. These pretzel orbits result in the counter-rotating electron and positron beams colliding only within the CLEO detector, thereby eliminating unwanted collisions outside of CLEO and minimizing the beam-beam interaction.

The CESR beam pipe has a 9 cm horizontal aperture and a 5 cm vertical aperture, and contains both beams as they undergo $x, y = \pm 2$ cm pretzel orbits. This means that the wiggler needs to be strong enough to produce 2.1 T with a pole separation of at least 5 cm and wide enough to produce a suitably uniform field over a significant fraction of the 9 cm horizontal aperture. This is achieved with a 238 mm pole width and 76 mm gap height (see Figure 6.8).

This field would be expensive to produce with a permanent magnet of reasonable size and weight with a pole separation of over 5 cm. Additionally, permanent magnet wigglers had the disadvantage of being impractical to turn off during the multiple modes of operation for CESR. Using an electromagnetic wiggler overcomes

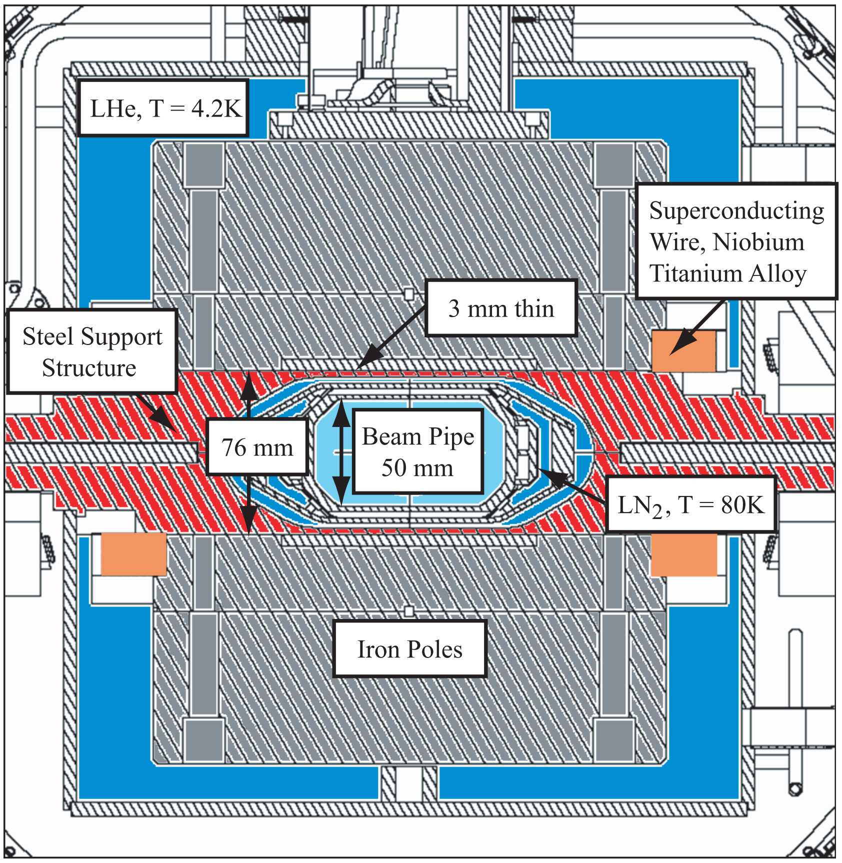

Figure 6.9: Vertical cross-section of the magnet, cryostat, shielding, and support structure for the CESR-c wigglers in CESR.

this problem, but achieving the desired field and gap with a normal conducting electromagnetic wiggler would have required a magnet with prohibitively large power consumption. Thus, superconducting magnet technology was the option chosen for the CESR-c wigglers [38].

The pole gap in the CESR-c wigglers, $g_p = 7.6\,\text{cm}$, is as small as possible while still providing room between the 5 cm tall beam pipe and the pole face for the required cryogenics, insulation, radiation shielding, and mechanical support structure. Fitting all of the supporting infrastructure for the wigglers into a 1.3 cm vertical gap between the poles and the beam pipe was at the limit of what was feasible (see Figure 6.9).

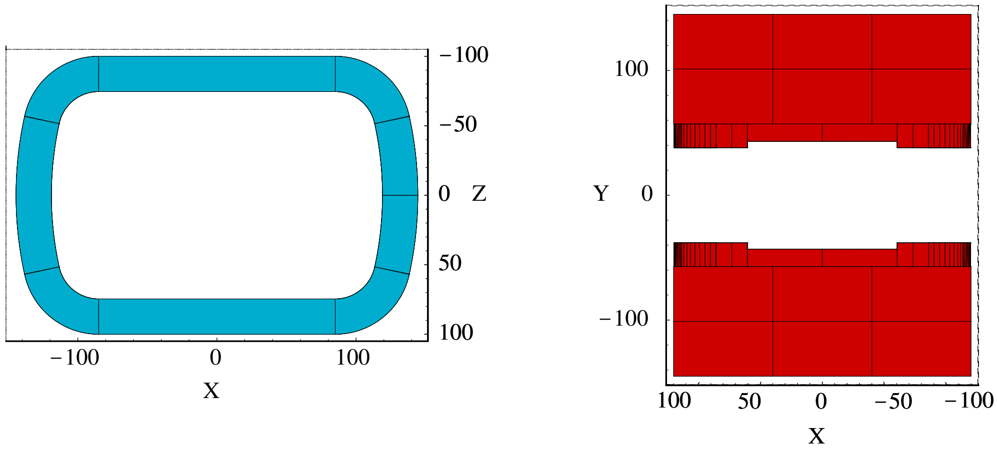

Figure 6.10: The exact coil curvature and pole cutout shapes of the CESR-c wiggler.

With a combination of wide poles and cut-outs in the pole faces (see Figure 6.10), the CESR-c wigglers achieve a field roll-off of $\Delta B/B_0 = 7.7 \times 10^{-5}$ at $x = 10\,\mathrm{mm}$ and $\Delta B/B_0 = 2.0 \times 10^{-3}$ at $x = 40\,\mathrm{mm}$. A final design consideration on the CESR-c wigglers was the exact coil curvature around the ends of the poles. The radii of curvature are chosen separately for the central ($L_{pole} = 20\,\mathrm{cm}$) and end poles ($L_{pole} = 10, 15\,\mathrm{cm}$) to keep the local field strength below the quench limit (see Figure 6.10) [31].

6.2.2 Experimental Performance in CESR

The CESR-c wigglers have been studied using direct experiments involving the wigglers and indirect evidence gathered during daily operation of CESR for the past three years. These studies have shown that the wiggler nonlinearities have produced no significant complication to the machine performance or degradation of the machine luminosity or dynamic aperture [44, 20]. Nonlinearities are not nonexistent in the CESR-c wiggler dynamics, but with a lattice full of independently tuned sextupoles, the entire ring performance has been optimized to produce a dynamic aperture that is limited by the 5 cm tall beam pipe and not the wiggler nonlinearities.

The dominant field error in the CESR wigglers is an effective skew quadrupole component that was not identified until after the wigglers were constructed. This error was determined to come from left/right symmetric coil widening that was different for the upper and lower coils. When the coils were wound around the poles, successive layers of wires were not held at a fixed position at the transverse edges of the poles; this resulted in the pole plus coil width varying by up to approximately 1 mm for the poles in the CESR-c wigglers. The coil widening effect was not identified until after the poles were already constructed but its negative impact on the beam dynamics was successfully minimized by sorting coils with similar deformations into upper and lower pairs [42].

Experiments have been performed in CESR to characterize the behavior of the twelve superferric wigglers in order to improve the low energy performance of CESR and maximize the success of CLEO's physics program [44, 20]. In these experiments, the amplitude dependent tune shifts coming from the wigglers were determined by measuring the tune while varying the beam position in the wiggler. The beam position in the wiggler can be varied with a closed orbit bump which reveals amplitude-dependent tune shifts coming only from the region where the beam is being displaced. This can be constrained to either one wiggler or a group of wigglers. The beam position in the wiggler can also be varied with an orbit oscillation around the entire ring which shows the effect of the wigglers plus all other sources of amplitude-dependent tune shifts in the accelerator, like multipole magnets and field errors.

The tune shift with bump position and tune shift with shaking amplitude have been measured in CESR with the wigglers at their design field strength, 2.1 T [43, 20]. These experiments have shown reliable agreement with Bmad-based simulations using the full nonlinear wiggler model fitted to a field from OPERA-3d.

The successful performance of the superferric wigglers in CESR suggests that they might also perform well as the ILC damping wigglers. However, using the CESR-c wiggler in the ILC damping ring could require operating them below their operational range ($1.9 - 2.1\,\mathrm{T}$). The amplitude-dependent tune shifts given in Equations 5.15 and 5.16 become weaker with peak field, but it is important to verify that there are not additional field-dependent nonlinearities in the wigglers that have a larger effect a lower magnetic fields. If this type of nonlinearity exists, it would not have been explored in standard CESR operation but may be relevant if the CESR wigglers were redesigned for the ILC damping rings. Whatever the field-dependent effect on the beam by the wigglers, it is important to verify that the real effects observed in CESR are accurately represented in the Bmad-based simulations.

The tune shift versus bump position experiment was repeated in CESR for this dissertation in a low field ($B_0 = 1.4\,\mathrm{T}$) wiggler configuration to examine the dependence on the peak field. Three vertical steering elements were used to create a closed-orbit bump in wigglers No. 18E1, 18E2, and 18E3 in CESR. The resulting data and corresponding curves from Bmad simulations can be seen in Figure 6.11. Additionally, a closed-orbit bump was created in wigglers No. 15E, 14E1, and 14E2 (see Figure 6.12). The simulation curves correspond to linear, ideal nonlinear, and full nonlinear models of the wiggler only, in all cases a full nonlinear model is used

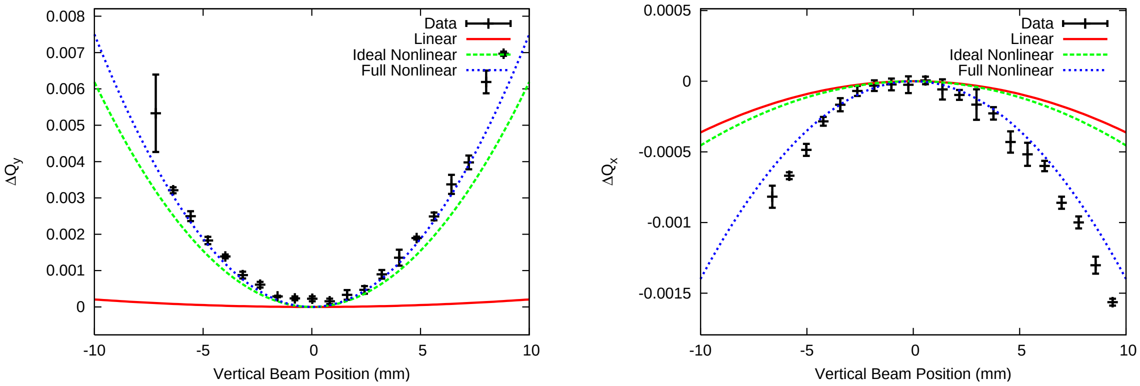

Figure 6.11: Vertical and horizontal tune shift with vertical beam position in wigglers 18E1, 18E2, and 18E3 of CESR operating at $B_0 = 1.4\,\mathrm{T}$.

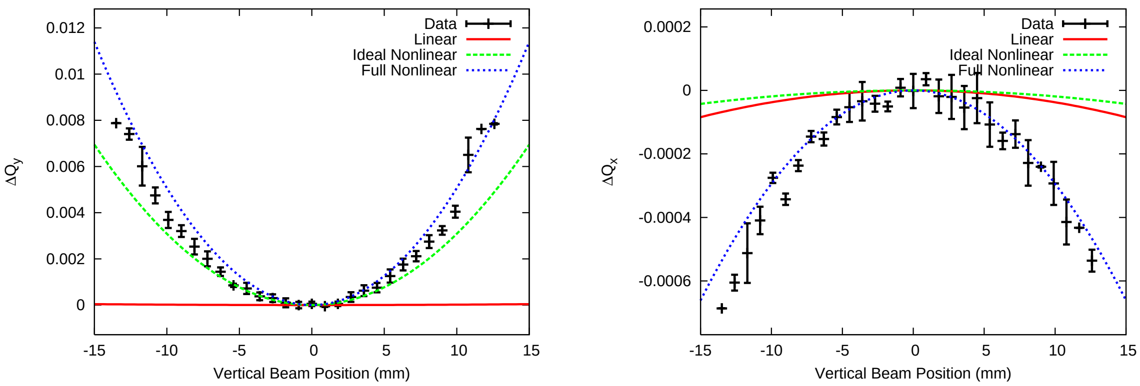

Figure 6.12: Vertical and horizontal tune shift with vertical beam position in wigglers 15E, 14E1, and 14E2 of CESR operating at $B_0 = 1.4\,\mathrm{T}$.

for the rest of the lattice.

The agreement between the data and the full nonlinear wiggler model in Figures 6.11 and 6.12 is an excellent validation of this wiggler model. Additionally, the simulation results for the linear and ideal nonlinear wiggler models are validated by the way in which they disagree with the data. For example, a linear wiggler model produces no amplitude-dependent tune shift, so varying the beam position in a localized section of wigglers should result in no horizontal or vertical tune shift. Figures 6.11 and 6.12 do show a small amount of tune variation with the linear wiggler model, this variation is not coming from the wigglers but from sources in the rest of the ring that came about because the orbit distortion was not able to be perfectly zeroed outside the localized wiggler regions. An ideal nonlinear wiggler model has the vertical octupole-like amplitude-dependent tune shift, but no horizontal dependence. Therefore, this model should incorporate the majority of the vertical tune shift seen in the data and none of the horizontal tune shift; this is again confirmed by the results in Figures 6.11 and 6.12. The small amount of horizontal tune shift with vertical beam position seen in the ideal nonlinear wiggler model is again coming from other sources in the ring and not the wigglers.

6.2.3 Simulated Performance in ILC

The CESR-c wigglers have the same period and roughly the same peak magnetic field as the TESLA wiggler. However, with four times the pole width and three times the gap height, the CESR-c wigglers have a field roll-off two orders of magnitude smaller than the TESLA wigglers (see Figure 6.13). Additionally, comparing Figure 6.2 with Figure 6.7 shows that the TESLA wiggler produces a field that is shaped more like a square wave and the CESR-c wiggler produces a more sinusoidal field. These differences in field roll-offs and profiles suggest that the CESR-c wiggler could be better represented with only the dominant field mode than the TESLA wiggler. This would mean the CESR-c wiggler would be more like an ideal nonlinear wiggler model, have less realistic nonlinearities coming from higher order field modes, and result in a better performance. Given the anticipated improvement in beam dynamics coming from the more horizontally uniform and longitudinally sinusoidal field, the CESR-c wiggler was suggested as a possible candidate for the ILC damping wiggler.

Design modifications were made to the OPERA-3d model of the CESR-c wig-

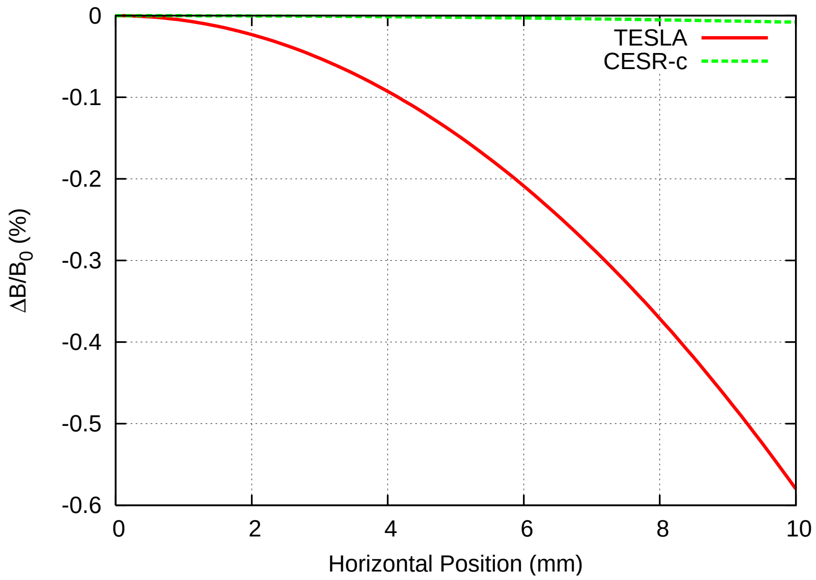

Figure 6.13: Field roll-off of the TESLA and CESR-c wigglers.

gler to correspond with the TESLA wiggler design. The current in the superferric wigglers was lowered from 141 A to 92 A to lower the field of the CESR-c wigglers to that of the TESLA wiggler, $B_0 = 2.1 \rightarrow 1.67\,\mathrm{T}$. The number of poles in the CESR-c wiggler design was changed from 8 to 22 to correspond with the number of central poles in the TESLA wiggler design utilized in the TESLA dogbone ring, 18, plus 2 trajectory-matching poles on each end of the wiggler. This changed the length of the CESR-c wiggler from 1.3 m to 4.1 m. This new wiggler design has not deviated significantly from the fundamental properties of the CESR-c wiggler, thus this is called the modified CESR-c wiggler (see Figure 6.14 and Table 6.4) [45].

Using the modified CESR-c wiggler for tracking studies in the TESLA dogbone ring yields a significant increase in the dynamic aperture for the full nonlinear wiggler model compared with the full nonlinear TESLA wiggler model (see Figure 6.15). This is also reflected in the smaller tune footprint of the modified CESR-c wiggler as compared to the TESLA wiggler (see Figure 6.16).

Comparing Figure 6.16 with Figure 6.4, reveals that the amplitude-dependent

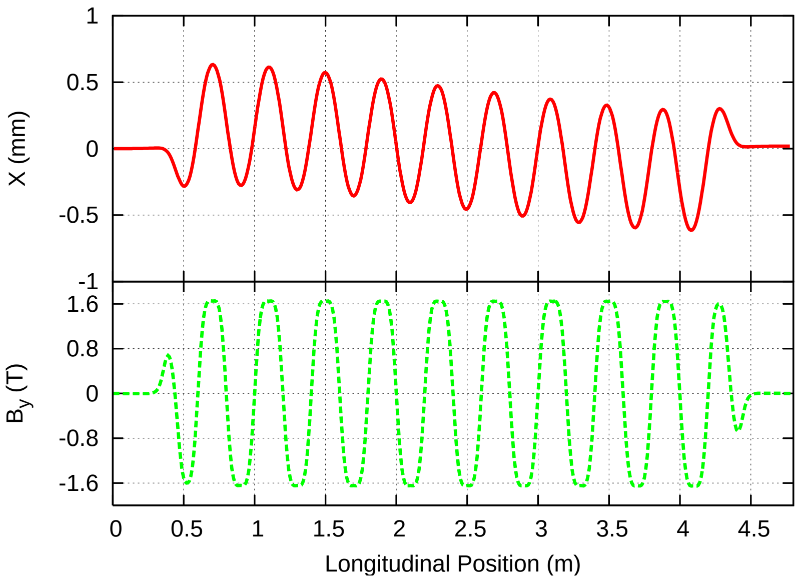

Figure 6.14: Vertical magnetic field and horizontal trajectory of a 5 GeV electron through the 22-pole, modified CESR-c wiggler.

Table 6.4: Physical specifications of the modified CESR-c wiggler.

Parameter	**Unit**	**Value**
Peak Field	T	1.67
Number of poles		22
Total length	m	4.1
Period	m	0.4
Pole Width	cm	23.8
Gap Height	cm	7.6
$\Delta B/B_0$ at $x = 10\,\mathrm{mm}$		7.7×10^{-5}
Current	A	92
Beam Energy	GeV	5

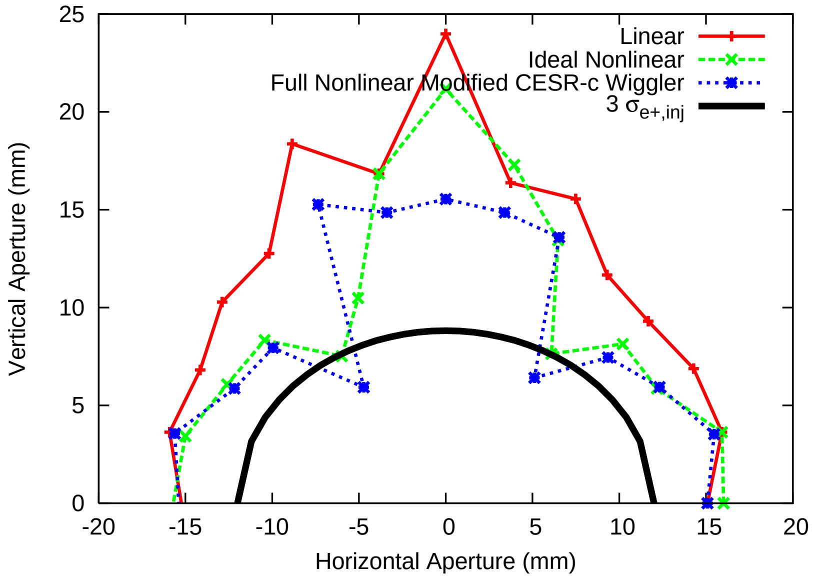

Figure 6.15: Dynamic aperture results for the linear, ideal nonlinear, and full nonlinear models of the modified CESR-c wiggler in the TESLA damping ring.

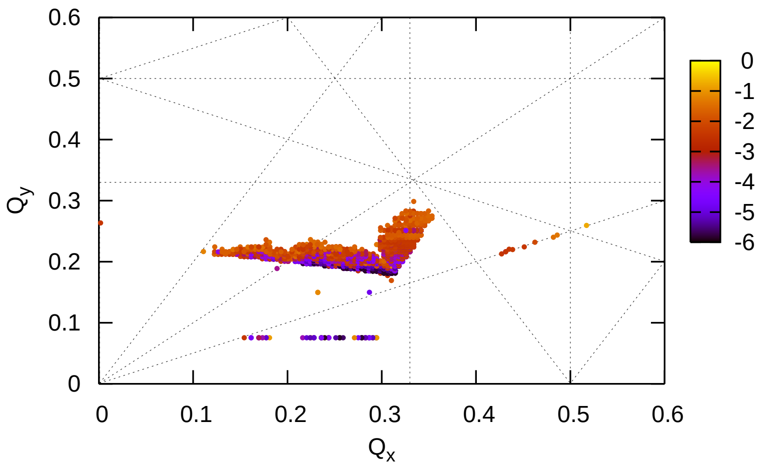

Figure 6.16: Frequency map analysis result in tune space for the full nonlinear model of the modified CESR-c wiggler in the TESLA damping ring. Operating point is $Q_x = 0.31$, $Q_y = 0.18$.

Table 6.5: Wiggler-related lattice parameters in the TESLA damping ring lattice, using the full nonlinear model of the modified CESR-c wiggler.

τ_{damp}	$22.7\,\mathrm{ms}$
$\epsilon_{x,rad}$	$0.50\,\mathrm{nm}\cdot\mathrm{rad}$
σ_δ	$0.13\,\%$

tune shifts are much smaller in the case of the CESR-c wiggler. This results in particles crossing less tune-plane resonances and the dynamic aperture not being degraded as much from the linear wiggler case for the modified CESR-c wiggler as compared to the TESLA wiggler. In fact, the dynamic aperture for the modified CESR-c wiggler is nearly "ideal" meaning that the dynamic aperture of the full nonlinear model is not significantly smaller than dynamic aperture of the ideal nonlinear model. This means that the total nonlinearities in the modified CESR-c wiggler are dominated by the inherent wiggler nonlinearity, and the realistic nonlinearities coming from a wide pole width and high field uniformity are very weak and are not degrading the dynamic aperture.

The CESR-c wiggler vertical gap of $g_p = 7.6\,\mathrm{cm}$ provides a beam stay-clear in CESR of 5 cm. This gap is three times that of the TESLA wiggler and is expected to be sufficient to minimize beam loss in the ILC damping rings. Additionally, the wiggler-related lattice parameters meet their specified targets in the TESLA damping ring after the TESLA wiggler is replaced with the modified CESR-c wiggler (see Table 6.5).

6.2.4 CESR-c Wiggler Conclusions

A modified version of the CESR-c wiggler was used in the TESLA dogbone damping ring with excellent results. The full nonlinear wiggler produces a dynamic aperture which is dominated by the aperture defined by the inherent octupole-like wiggler nonlinearity. This suggests that the specific pole shape and size of the CESR-c design have been well optimized for reducing the realistic wiggler nonlinearities. The TESLA dogbone dynamic aperture is still not large enough to handle the misalignments and errors of a non-ideal lattice, but simulations suggest that this is a feature of the TESLA dogbone ring itself and not the CESR-c wigglers. Therefore, initial results suggest that a modified version of the CESR-c wigglers would perform well as the ILC damping wiggler.

6.3 ILC Wiggler Technology Decision

At the time of these results, the international ILC damping ring design community was mobilizing to organize and evaluate the damping ring options available throughout the world. The damping ring community felt that there was an adequate amount of information known about the poor performance of the TESLA wiggler; however, a more thorough analysis was requested of the performance of the modified CESR-c wigglers in the seven damping ring configuration study lattices (see Table 4.4).

Dynamic aperture, dynamic aperture with multipole field errors, and frequency map analysis simulations were performed using the modified CESR-c wiggler, with the linear, full nonlinear, and ideal nonlinear tracking models, in each of the seven lattices. Results from these simulations can be found in Appendix B with the

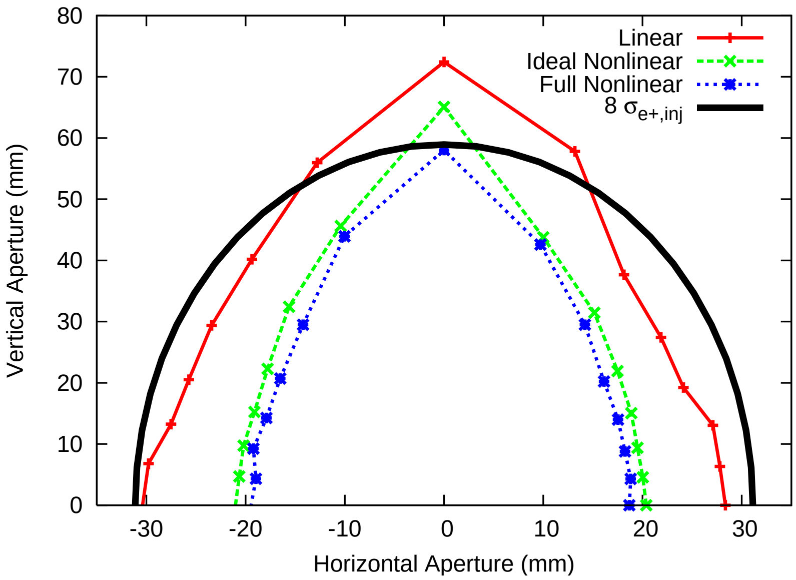

Figure 6.17: Dynamic aperture results for the linear, ideal nonlinear, and full nonlinear models of the modified CESR-c wiggler in version 1.0 of the OCS damping ring.

conclusion being that the modified CESR-c superferric wigglers operated very well in all of the configuration study lattices [12]. In all lattices, the modified CESR-c wiggler produced negligible degradation of the dynamic and energy apertures beyond that of the linear and ideal nonlinear wiggler results; for example, the performance of the initial baseline ILC damping ring lattice, OCS, is given in Figure 6.17. This suggests that the modified CESR-c wiggler meets and exceeds the physics requirements of the ILC damping ring.

Other simulations confirmed that, in addition to the dynamic aperture, the physical aperture of the modified CESR-c wiggler is sufficient for meeting the required apertures in each of the candidate ILC damping ring lattices. Simulations studied the injection efficiency [46] and electron cloud production thresholds [47] with physical apertures and determined that in both cases a vertical beam pipe aperture of over 48 mm is needed in the wiggler to meet ILC damping ring performance requirements. The CESR-c wigglers have a 76 mm vertical gap and operate with a 50 mm vertical beam pipe in CESR, thus meeting the physical aperture requirements of the ILC damping ring.

A decision on the magnet technology to be used for the ILC damping wiggler was made based on the results of these physical and dynamic aperture simulations. Additionally, the practical costs and risks (e.g. radiation resistance, availability, and power consumption requirements) associated with the choice of technology for the ILC damping wigglers were considered [48]. Ultimately, superferric technology was chosen for the ILC damping wiggler, in part because the TESLA permanent magnet wiggler did not meet the dynamic and physical aperture requirements and no other permanent magnet option existed.

6.4 Baseline ILC Damping Ring

Since superferric technology was chosen for the ILC wigglers, work has proceeded using the best available option for a superferric damping wiggler, the modified CESR-c wiggler. In addition, development and optimization has proceeded on the overall lattice design of the damping ring, resulting in more recent lattice versions of the OCS lattice [49, 50]. The circumference and detailed lattice design of these rings differs considerably from TESLA and it is important to confirm that the modified CESR-c wiggler still performs at a high level in these rings.

The biggest difference between the wigglers in the TESLA ring and the wigglers in the OCS ring are their unit and total lengths. The OCS ring is a 6 km ring and so it has a shorter revolution time than the TESLA ring and requires less wigglers to achieve $\tau_{damp} = 25\,\text{ms}$. The OCS ring was designed with 80 wigglers, less than the 108 in the TESLA ring. Using 80 modified CESR-c wigglers in the OCS ring

Table 6.6: Wiggler-related lattice parameters in version 2.0 of the OCS damping ring lattice, using the full nonlinear model of the modified CESR-c wiggler.

τ_{damp}	20.3 ms
$\epsilon_{x,rad}$	$0.62\,\mathrm{nm}\cdot\mathrm{rad}$
σ_δ	0.13 %

to achieve the target damping time allowed the magnets to be shortened from 22-pole, 4.1 m in TESLA to 14-pole, 2.5 m unit length in OCS. This change in length was accepted to the modified CESR-c wiggler to make it suitable for use in the OCS lattice, the baseline ILC damping ring lattice.

In OCS, the modified CESR-c wiggler provides a damping time significantly shorter than is required (see Table 6.6) allowing the possibility of using even less wiggler to save money in the damping ring. Simulations with the full nonlinear model of the modified CESR-c wiggler meet the energy spread requirements and provide an equilibrium horizontal emittance which is right at the target value. Additionally, in these more recent OCS lattice versions, the modified CESR-c wiggler still provides the required dynamic, physical and energy apertures (see Figure 6.18).

The OCS lattice was modified in version 6.0 by moving the wigglers and RF cavities to four locations in the ring, instead of the eight locations in version 2.0. This modification was made in order to satisfy the desires of the scientists designing the conventional systems associated with the ILC; by concentrating the wiggler magnets and RF cavities, the cryogenic production plants and transfer lines would only have to supply four locations, not eight. However, this change reduced the symmetry of the OCS lattice in version 6.0 resulting in the baseline lattice dynamic

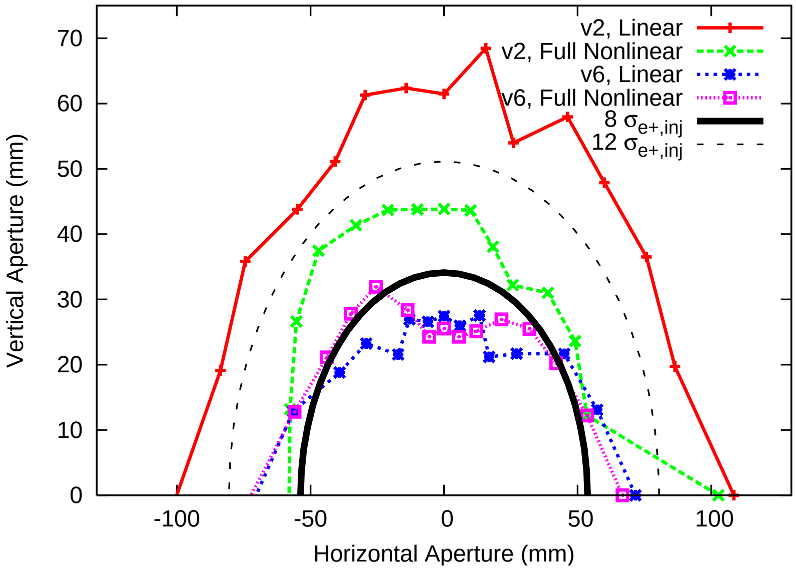

Figure 6.18: Dynamic aperture results for the linear and full nonlinear models of the modified CESR-c wiggler in version 2.0 and 6.0 of the OCS damping ring.

aperture being degraded to an amplitude below that of the wiggler-limited dynamic aperture.

Additionally, the nonlinearities of the modified CESR-c wigglers are weak enough to produce a large dynamic aperture even when including multipole field errors on the dipoles, quadrupoles, and sextupoles (see Figure 6.19). These results suggest that the multipole field errors used are quite strong and are limiting the dynamic aperture below that of both the baseline lattice aperture and the wiggler-limited dynamic aperture. Finally, at $B_0 = 1.67\,\mathrm{T}$ and $L = 2.5\,\mathrm{m}$, using 80 modified CESR-c wigglers in the OCS damping ring results in a 20 ms damping time which is less than required to meet the required emittance in 200 ms.

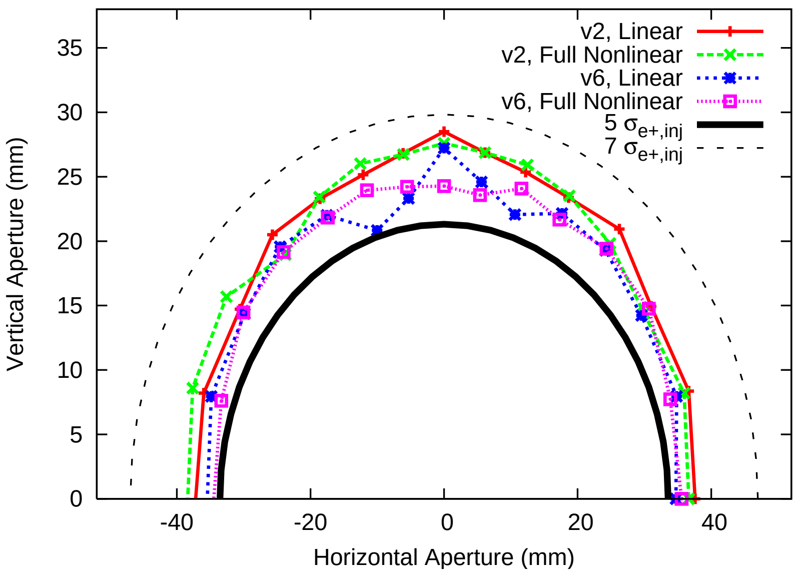

Figure 6.19: Dynamic aperture results for the linear and full nonlinear models of the modified CESR-c wiggler in version 2.0 and 6.0 of the OCS damping ring. Including multipole field errors on the dipoles, quadrupoles, and sextupoles. Shown are curves of the average dynamic aperture result for 15 random seeds.

Chapter 7

ILC-Optimized Wiggler Design

The previous results show that the modified CESR-c wiggler is a better wiggler choice for the ILC damping rings than the TESLA design, but it is not necessarily the best choice possible. Simulations show that the modified CESR-c wiggler exceeds the physics requirements of the ILC; however, superior performance is accompanied by a wiggler that is perhaps larger and more expensive than necessary to meet the goals of the ILC.

The amplitude of the modified CESR-c wiggler dynamic aperture is nearly that of the linear wiggler aperture in the ILC which suggests a larger field roll-off could be accommodated. There is likely room in the phase space of wiggler parameters to design a new wiggler which is less expensive than the CESR-c wiggler but still minimizes the impact of the wiggler on the ILC damping ring's dynamic aperture. Potentially, a superferric wiggler could be designed that satisfies the damping ring requirements with a lower cost and with fewer construction challenges than the CESR-c wiggler model.

7.1 Optimization Goals

The design of the modified CESR-c wiggler resulted from a melding of the existing wiggler used in CESR with the wiggler constraints considered for the TESLA damping ring. Therefore, the modified CESR-c wiggler has not been optimized for the specific engineering and cost challenges present in the ILC damping rings. The goal of this dissertation is to present the conceptual design of a superferric wiggler that is suitable for the ILC damping ring which has been realistically optimized considering cost, construction, and performance requirements.

Practical constraints like cost, construction, operation, and reliability of the wiggler may make certain beam or lattice parameters unattainable. For example, a large dynamic aperture requires wide poles with a long period, but it is also desirable to minimize the cost and thus size of the wiggler. Alternatively, re-optimization may reveal that a large reduction in the width of the wiggler leads to a slight reduction in the dynamic aperture and a significant reduction in cost, which could be an acceptable trade-off.

7.2 Motivation

There are a number of factors that must be balanced during the wiggler redesign process–the most important element being cost. The twelve 1.3 m CESR-c wigglers each had a capital cost of roughly \$250,000 [48], and with a 2.5 m length the modified CESR-c wiggler will cost nearly twice that, or \$500,000. Additionally, international cost studies have concluded that the approximate cost of the damping ring is 10 % of the cost of the entire ILC, and the cost of the damping wigglers is approximately 22 % of the entire damping ring [51].

Therefore, a reduction in the physical size or total number of wigglers could yield significant cost savings when integrated over two 6 km damping rings, each with 80 2.5 m wigglers. Reducing the size of a single wiggler would save on the cost per wiggler and increasing the damping capacities of the wiggler would save on the total number of wigglers required. Increasing the peak field of the modified CESR-c wiggler would be an easy way to use less wigglers and save money in the ILC damping rings; however, detailed simulations must be performed to determine if a stronger wiggler would compromise the ring's performance by increasing the horizontal emittance, energy spread, or nonlinearities.

7.2.1 Construction

Modifying the superferric wiggler construction process has the potential to reduce the unit cost of the ILC damping wigglers without compromising the ring's dynamic performance. The twelve CESR-c wigglers were carefully constructed in house at Cornell with, for example, technicians winding the superconducting wires around the iron poles by hand. It is believed that this process could be redesigned for the ILC to use machines to wind the coils. Automating this process would eliminate the winding errors that led to coil misalignments and field errors in the CESR wigglers, and allow the 160 ILC wigglers to be feasibly mass-produced [52].

In addition to saving money, changes to the physical design of the wiggler might simplify the engineering challenges expected during the construction and installation of 160 wiggler magnets. One engineering challenge present when the superferric wigglers were assembled and installed in CESR was the support structure for the magnet. The stainless steel plate used to support the wigglers in CESR is 1.3 m long and narrows to 3 mm for a portion of the width (see Figure 6.9).

Moving and supporting this plate during construction and installation was a delicate process. If the plate became twisted during installation it was taken back to the machine shop to be re-smoothed and aligned. Performing multiple iterations of smoothing this extremely thin plate was a time consuming but surmountable task for twelve CESR-c wigglers; however, it will not be feasible for the quick and reliable mass-production of 160 ILC wigglers. Therefore, the vertical gap in the superferric CESR-c wiggler assembly does not meet the engineering requirements of the damping ring and the pole gap must be increased.

The ILC damping ring wiggler is currently designed with a 2.5 m unit length (14 poles in the OCS lattice), nearly twice that of the CESR-c wiggler (8 poles, 1.3 m). Doubling the CESR-c wiggler length also requires doubling the length of the cryostat, vacuum chamber, and the rest of the wiggler assembly. All of which may have to be redesigned and could potentially become significantly more difficult to construct, install, and operate at a longer length.

7.2.2 Radiation Load

Additionally, the beam current and energy going through the wigglers in the ILC damping ring will not be the same as in their proven application in CESR and this will change the radiation load on the ring. The total power of the photons radiated by a wiggler is given by [3]:

$$P_{rad}(\mathrm{kW}) = 0.633 \cdot I(\mathrm{A}) \cdot L_{wig}(\mathrm{m}) \cdot E^2(\mathrm{GeV}) \cdot B_0^2(\mathrm{T}), \tag{7.1}$$

where E and I are the energy and current of the electron beam. In CESR, the wigglers operate with beams having a maximum current of 130 mA and an energy of about 2 GeV per beam. This results in $\approx$ 2 kW of radiated power per wiggler in CESR which can be reasonably handled with radiation absorbers around the wigglers.

In the ILC damping ring the beam will be significantly more intense at 400 mA and 5 GeV. This results in 42 kW of radiated photon power which means that significant radiation shielding is required to protect the wiggler vacuum chamber and prevent the radiated photons from ejecting electrons from the chamber walls and forming an electron cloud. The horizontal chamber aperture needs to be as wide as possible and made at a shallow angle to reduce the incident radiation density.

This could potentially require widening the support structure and even the wiggler poles themselves to keep the heat load below an acceptable level. Widening the support structure and the poles would require a complete redesign of the structure and would be expensive.

7.2.3 Vacuum Chamber

To simplify construction and assembly, the CESR-c wigglers are designed so that the wiggler vacuum chamber is actually welded to the magnet and is not separable. This precludes removing the chamber and treating it or cleaning it in order to achieve ultra-low vacuum. The required vacuum in CESR is not low enough for this to be a problem; however, because of the higher beam current in the ILC damping rings, the vacuum in the damping ring will have to be kept lower than in CESR to stay below the instability thresholds for the collective effects.

This lower vacuum requirement requires modifying the CESR-c wigglers to allow for a separate vacuum chamber which can be baked to clean the surface and achieve ultra-low vacuum. This difference again could necessitate changes to the CESR-c wiggler design in order to make it suitable for the ILC damping ring engineering requirements. For example, there needs to be enough space between the vacuum chamber and the cold-mass to be able to reliably remove and reinsert the beam pipe during vacuum processing without damaging the chamber or the magnet.

7.2.4 Cryogenics

Another costly feature of the superferric wigglers in CESR is the 4.2 K liquid helium bath used to cool the superconducting NbTi coils. Again, this design was appropriate for twelve wigglers in CESR but does not scale suitably to the ILC requirements.

Cooling 160 damping ring wigglers, each entirely surrounded by their own liquid helium bath, would require a very large amount of expensive liquid helium and a significant amount of cool-down time. Therefore, the CESR-c wiggler design may have to be changed to allow for switching the cryogenic structure from directly bathing all of the poles and coils in liquid helium to a system of tubing on the poles which indirectly cools the coils [52]. This would save money by improving reliability and allowing for quicker repair and recovery time in the ILC damping ring. Additionally, without the liquid helium bath, the wiggler assembly would be simplified by eliminating the need for the wall inside the magnet poles which separates the helium from the vacuum. Eliminating this wall saves time and money during construction and allows a larger vertical margin between the poles and beam pipe permitting a thicker support plate with the same pole gap.

Another change that must be made to the CESR-c wiggler design for it to be an acceptable ILC damping wiggler is to remove the liquid nitrogen from the system. At 80 K, liquid nitrogen is used in the CESR wigglers to shield the room temperature (300 K) copper beam pipe from the liquid helium temperature (4.2 K) wiggler magnet. Additionally, using liquid nitrogen cools the wiggler magnet to an intermediate temperature without using as much expensive liquid helium. However, the safety requirements in certain countries do not allow liquid nitrogen in enclosed tunnels. Since the global location of the ILC is not known, all of the cryogenic systems in the ILC must be designed with only liquid helium and no nitrogen. With even more liquid helium in the system, this another reason to avoid the liquid helium bath and use less helium in an indirect cryogenic system.

The design of the construction, radiation load, vacuum chamber, and cryogenics requirements of the ILC damping wiggler are realistic engineering considerations, but will not be covered further here. These practical requirements will only be used as guidelines while interpreting the results and motivation while selecting the desired outcome of the wiggler design optimizations in the rest of this chapter.

7.3 Optimization Methods

The ILC damping wiggler optimizations began with minimal changes to the overall CESR-c wiggler design. The reason for this was to keep the final ILC-optimized superferric wiggler model as similar in design, construction, and operation to the CESR-c wigglers as possible in order to prove its practical feasibility.

The pole gap and width were modified to establish the possibility of meeting the specified apertures while simplifying the engineering problems. The peak magnetic field was changed to learn how short the wiggler length could be made and still meet the desired beam parameters. Finally, the wiggler period was varied to map out the impact of the field nonlinearities on the damping ring's performance.

7.3.1 Details of the Magnet Model

Optimizations to the modified CESR-c wiggler model were performed using Radia. Straightforward modifications to the number of poles, coil currents, pole width, and other magnet parameters generates a magnetic field specific to that magnet shape, including sources of nonlinearities and fringe fields. Unless otherwise stated, all results were generated with the full nonlinear wiggler model in Bmad.

The quality and performance of each new magnet shape was evaluated through dynamic aperture and amplitude-dependent tune shift studies in version 2.0 of the

OCS damping ring. Though 2.0 is not the most recent version of the OCS lattice, it has the largest dynamic aperture and thus can reveal the dynamic aperture limits imposed by a wiggler model and not the lattice. This was necessary in order to observe potentially small changes in the dynamic aperture as the wiggler parameters changed during the optimization

The pole cut-out and variable radius coil curvature of the CESR-c wiggler (see Figure 6.10) were eliminated before the optimizations were performed. This was done to simplify changes to the pole dimensions and create a direct variation of field roll-off with pole width. These changes did not increase the field roll-off considerably ($\Delta B/B_0 = 0.020\,\%$ at $x = 10\,\mathrm{mm}$), therefore this "simplified" modified CESR-c wiggler still meets the ILC damping ring physics requirements with a less complicated and presumably cheaper magnet design. Thus, the optimizations given below can be viewed as worst-case scenarios, as the pole profiles and curvatures are taken to be a simplified version of the CESR-c wiggler pole and are not re-optimized for each new width, period, gap, or field. Once the ILC damping wiggler is ultimately selected, an optimization of the pole profiles and curvatures should be done to minimize the field roll-off, but this was not completed for the present analysis.

Finally, the optimizations described in the following sections were performed before taking into account the results of the previous sections. The magnet parameter being varied in each section is the only one changed from the simplified modified CESR-c wiggler's original design. The final ILC-optimized CESR-c wiggler will implement the recommendations coming from each individual optimization to follow and will be given in Section 7.8.

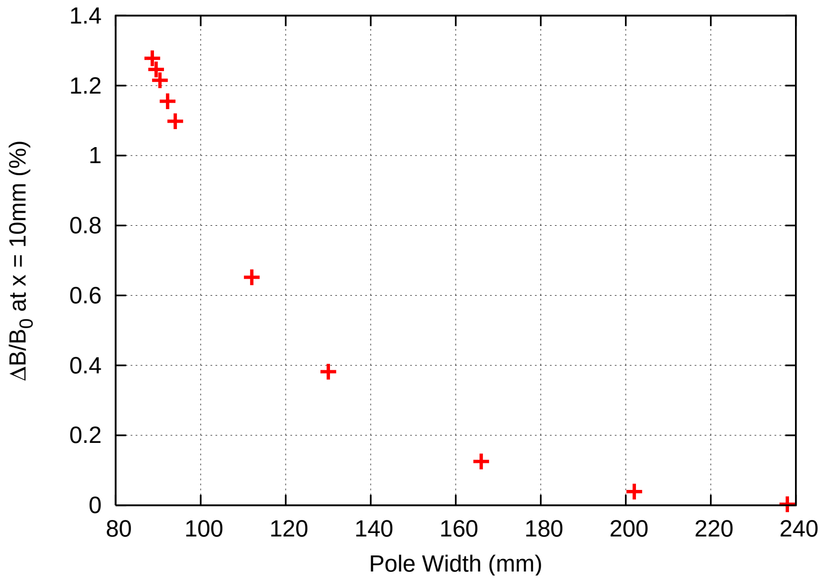

Figure 7.1: Variation of vertical field horizontal roll-off versus pole width of the simplified modified CESR-c wiggler.

7.4 Pole Width

Decreasing the pole width increases the roll-off of the magnetic field in the horizontal direction, causing the region of high field-uniformity to decrease until it hits the dynamic aperture and begins to negatively impact the trajectory of the beam core. With the simplified modified CESR-c wiggler, varying the width of the wiggler poles in Radia reveals a cubic dependence in the transverse field roll-off (see Figure 7.1).

Using these wiggler models in version 2.0 of the OCS lattice shows the impact of increased field roll-off on the dynamic aperture (see Figure 7.2). A clear range of dynamic aperture areas, from $10\,\sigma$ near the CESR-c wiggler width (238 mm) to below $5\,\sigma$ near the TESLA wiggler width (60 mm), allows the possibility of selecting the required dynamic aperture and then working backwards to see how wide the wiggler poles have to be. Additionally, as the width of the poles decreases, the maximum allowable error in the horizontal position of the wigglers also decreases

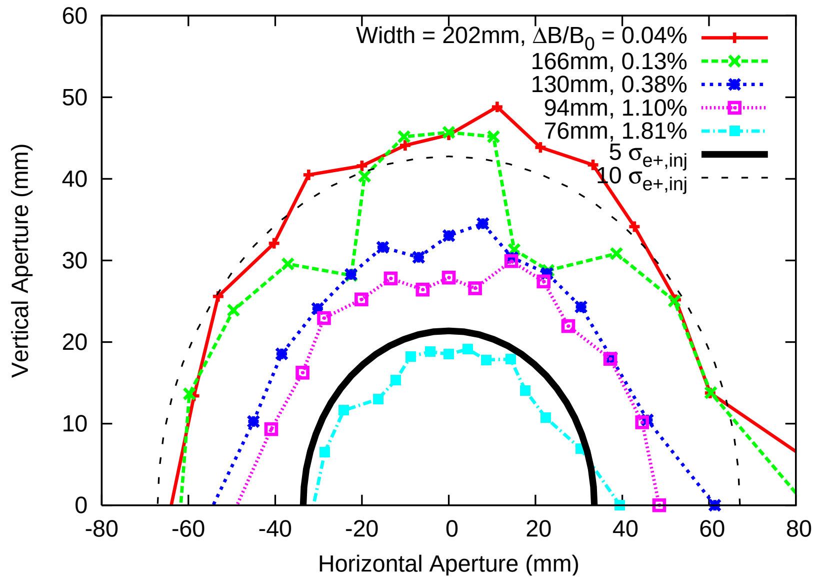

Figure 7.2: Dynamic aperture results for a range of pole widths of the simplified modified CESR-c wiggler.

(see Figure 7.3).

Recommendation

The size of the dynamic aperture depends clearly and directly on the wiggler pole width. This allows a reduction of the wiggler width if the benefit of narrower poles outweighs the minimal-to-significant decrease in dynamic aperture that would happen at a reduced pole width. Therefore, as long as a smaller dynamic aperture is acceptable, the wiggler width could be reduced to save money. However, the increased engineering challenges of a narrower wiggler support structure and increased photon density on the vacuum chamber do present a serious barrier to reducing the pole width. Balancing the cost/benefit ratio of narrower poles against these challenges leads to a final recommendation to keep the wiggler pole width at 238 mm–the same as the original CESR-c wigglers.

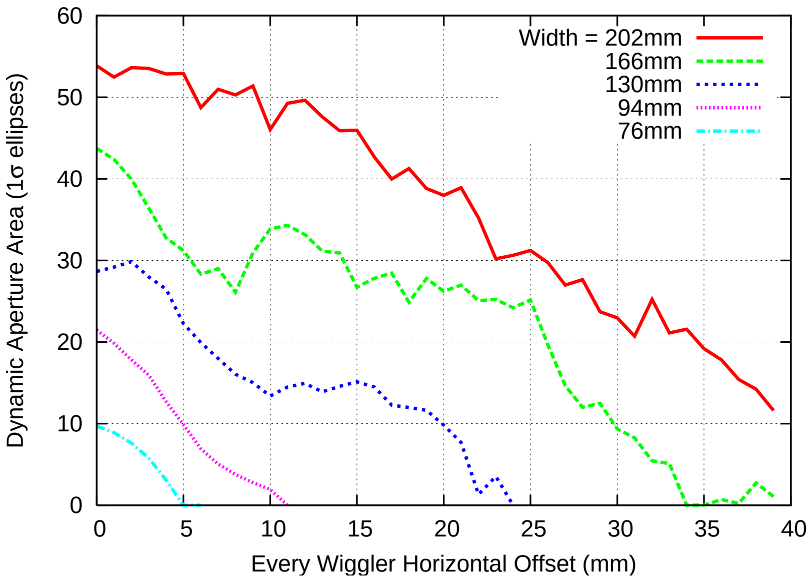

Figure 7.3: Wiggler offset results for a range of pole widths of the simplified modified CESR-c wiggler.

7.5 Pole Gap

Increasing the pole gap will be a necessary modification in order to meet the engineering requirements of the ILC. This should be possible given the weak linear dependence of field quality on the pole gap observed with the simplified modified CESR-c wiggler in Radia (see Figure 7.4). This small variation in field quality with pole gap results in minimal dynamic aperture degradation at larger pole gaps in version 2.0 of the OCS lattice (see Figure 7.5).

With a 1.67 T peak field in the damping ring, the modified CESR-c wiggler has a significantly lower current (92 A) than the 2.1 T wigglers in CESR (141 A). The wiggler current in CESR has an operational limit of 141 A to provide a safety margin below the quench limit of NbTi at $T = 4.2\,\mathrm{K}$ and $B_0 = 2.10\,\mathrm{T}$. Table 7.1 shows that with a 1.67 T wiggler, the wiggler current could be increased to allow the pole gap to be raised by at least 22 mm and still be below the NbTi quench limit at this temperature and lower field.

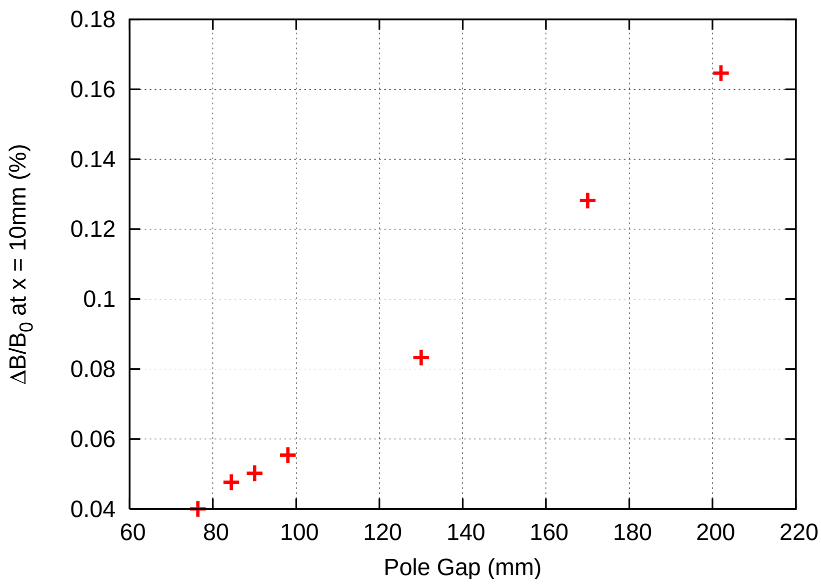

Figure 7.4: Variation of vertical field horizontal roll-off versus pole gap of the simplified modified CESR-c wiggler.

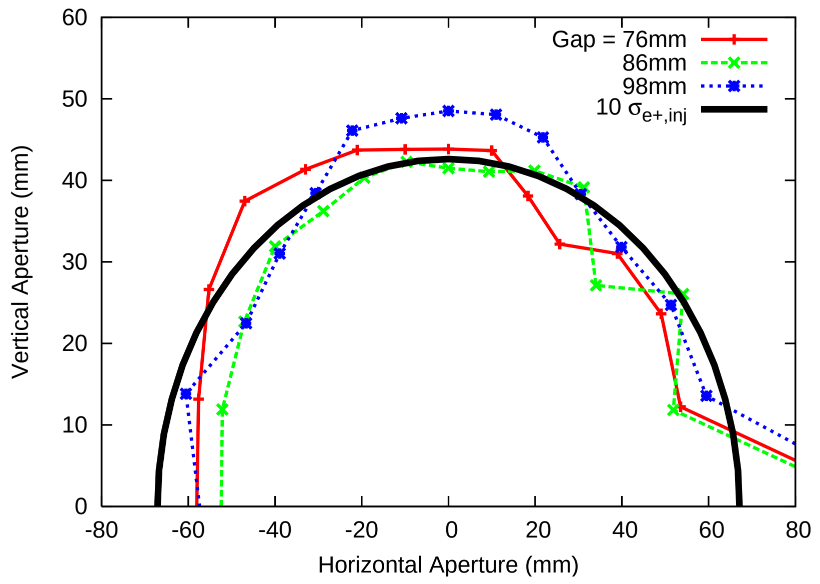

Figure 7.5: Dynamic aperture results for a range of pole gaps of the simplified modified CESR-c wiggler.

Table 7.1: Current values required to meet $\tau_{damp} = 25\,\mathrm{ms}$ in the ILC damping ring at pole gaps equal to and larger than the CESR-c value.

g_p **(mm)**	76.4	86.4	98.0
B_0 **(T)**	1.67	1.67	1.67
I **(A)**	92	107	125

Recommendation

Given the challenge in constructing a 3 mm thin stainless steel support plate, the superferric wiggler pole gap should be raised by at least 10 mm. The observed minimal dynamic aperture degradation at increased pole gap suggests that the gap could be raised even more, as long as the current can be increased to achieve the $\tau_{damp} = 25\,\mathrm{ms}$ ILC target. With a 1.67 T peak field, this allows the wiggler pole gap to be raised to 98 mm, leaving a sufficient safety margin below the superconducting quench limit.

7.6 Peak Field and Length

The TESLA wiggler was designed with a peak field of 1.67 T to meet $\tau_{damp} = 28\,\mathrm{ms}$ without pushing the radiation equilibrium horizontal emittance and energy spread above their specifications (see Table 7.2). However, this trade-off may need to be re-examined against the potential cost savings of a lower number of higher field wigglers. Another advantage of higher field wigglers would be achieved by using the same number of wigglers but reducing the length per wiggler to provide greater spacing between wigglers and allow more room for radiation shielding between the wigglers. Simulations described below were performed in this configuration (the same number of shorter wigglers) in order to examine the costs and benefits

Table 7.2: Lattice parameters that depend on the wiggler's peak magnetic field and their target extracted values in the ILC and TESLA damping rings.

Parameter	**Dependence**	**ILC target**	**TESLA target**
τ_{damp}	$L_{wig}^{-1} B_0^{-2}$	25 ms	28 ms
$\epsilon_{x,rad}$	$\beta_x \lambda_w^2 B_0^3$	$0.6\,\mathrm{nm} \cdot \mathrm{rad}$	$0.6\,\mathrm{nm} \cdot \mathrm{rad}$
σ_δ	$B_0^{1/2}$	0.15 %	0.13 %

of a modified wiggler magnet without requiring time-consuming changes to the number and location of wigglers in the baseline lattice which could change the ring's performance independent of changes to the wiggler.

Investigation of these options was performed using Radia models of the simplified modified CESR-c wiggler that ranged in number of poles from the 8-pole CESR-c wiggler to the 14-pole modified CESR-c wiggler in the OCS lattice, with the magnetic field changed to keep $\tau_{damp} = 25\,\mathrm{ms}$ (see Table 7.3). Taking into consideration the dependence of $\epsilon_{x,rad}$ on β_x, the shorter wigglers were moved to the low β_x end of the wiggler FODO cell, which has $\eta_x = 0$ throughout, in order to minimize the emittance. All of these configurations meet the target equilibrium energy spread of 0.15 % (see Table 7.3) and the required dynamic aperture in the version 2.0 of the OCS damping ring (see Figure 7.6). However, only the longest magnet has a peak field low enough to meet the target radiation equilibrium horizontal emittance, $0.6\,\mathrm{nm} \cdot \mathrm{rad}$.

Recommendation

Reducing the number of poles in the ILC damping wigglers would produce instant cost-savings in the construction of 160 wigglers; however, for a fixed damping time,

Table 7.3: Wiggler and lattice parameters resulting from peak field and length optimization, with peak field set to fix $\tau_{damp} = 25\,\mathrm{ms}$.

$\mathbf{L_{wig}}$ **(m)**	**1.3**	**1.7**	**2.1**	**2.5**
N_{poles}	8	10	12	14
B_0 (T)	2.25	1.92	1.69	1.51
τ_{damp} (ms)	24.2	24.2	24.1	24.6
$\epsilon_{x,rad}$ (nm · rad)	1.02	0.77	0.64	0.56
σ_δ (%)	0.143	0.133	0.126	0.119

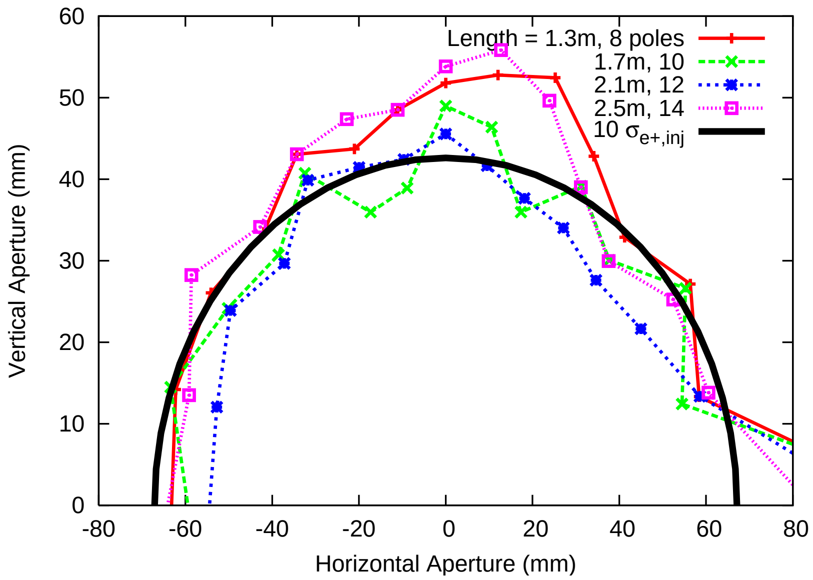

Figure 7.6: Dynamic aperture results for a range of pole numbers of the simplified modified CESR-c wiggler, with peak field set to fix $\tau_{damp} = 25\,\mathrm{ms}$.

the same number of shorter wigglers leads to an increase in horizontal emittance coming from the stronger wiggler fields. However, since $\epsilon_{x,rad}$ also depends on λ_w, a 12-pole wiggler with a shorter period could shift the emittance, $\epsilon_{x,rad} = 0.64\,\mathrm{nm}\cdot\mathrm{rad}$, below the target of $0.60\,\mathrm{nm}\cdot\mathrm{rad}$. Therefore, if the period of a 12-pole wiggler can be reduced to meet the target emittance, then a 12-pole ILC damping wiggler could work, otherwise the current 14-pole design should be used.

7.7 Magnet Period

The results of Section 7.6 motivate a magnet period optimization study for a 12-pole ILC damping wiggler. The wiggler period controls the strength of the dominant wiggler nonlinearity, so a short wiggler period can potentially increase the amplitude-dependent tune shift enough to push the tune footprint over resonances in the tune plane and degrade the dynamic aperture. Therefore, though a shorter period is good for the emittance–as long as the increased peak field does not counteract the benefit–and good for the horizontal dependent nonlinearities, it is bad for the dynamic aperture-limiting inherent vertical nonlinearity.

Generating the full nonlinear wiggler model is a detailed and time-consuming process as every new Radia field table must be re-fit to the harmonic expansion. Speeding this process up would simplify an examination of changes in the damping ring performance as the wiggler period is shortened. The dominant octupole-like wiggler nonlinearity is expected to exhibit the strongest growth with shorter periods and this nonlinearity is included in the ideal nonlinear wiggler model. Therefore, the ideal nonlinear model was used to initially determine where the wiggler period begins to degrade the dynamic aperture, and then the full nonlinear model was generated to examine the complete dependence.

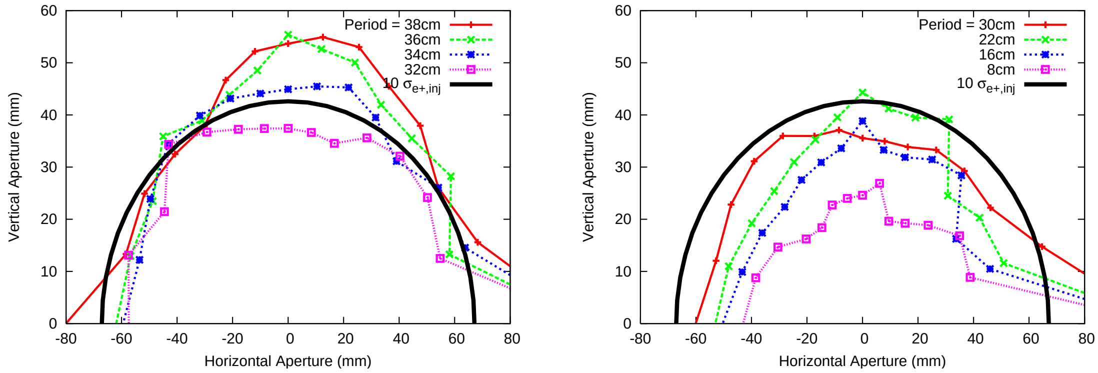

Figure 7.7: Dynamic aperture results for a range of wiggler periods of a 12-pole ideal nonlinear wiggler model, with peak field set to fix $\tau_{damp} = 25\,\mathrm{ms}$.

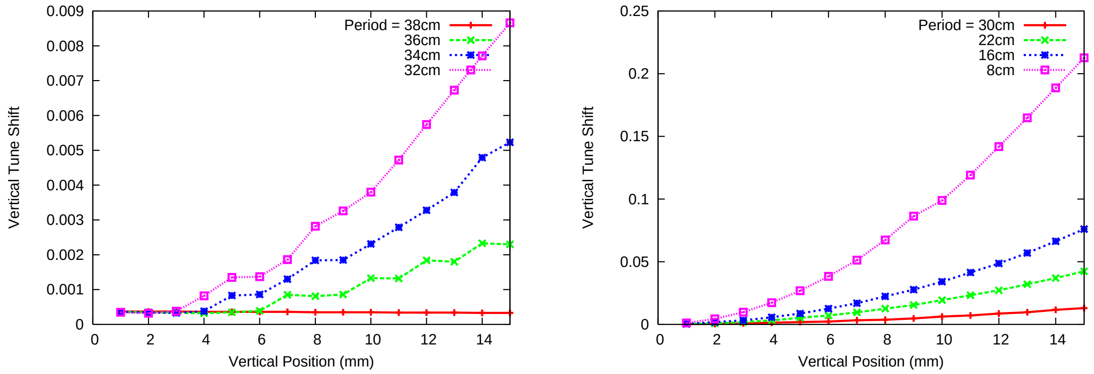

Figure 7.8: Amplitude-dependent tune shift results for a range of wiggler periods of a 12-pole ideal nonlinear wiggler model, with peak field set to fix $\tau_{damp} = 25\,\mathrm{ms}$.

Using 12-pole ideal nonlinear wiggler models in version 2.0 of the OCS damping ring reveals the dynamic aperture and tune-shift with amplitude as the wiggler period is decreased from 40 cm (see Figure 7.7 and 7.8). The increase in tune-shift with amplitude exhibited at shorter periods accounts for the decrease in dynamic aperture, which becomes significant at $\lambda_w = 30\,\mathrm{cm}$. These results suggest that a wiggler period below $\approx 32\,\mathrm{cm}$ would produce significant degradation of the beam dynamics in the ILC damping ring.

Generating detailed magnet descriptions in Radia led to full nonlinear models of the 12-pole simplified modified CESR-c wiggler with periods of $38 - 32\,\mathrm{cm}$ and

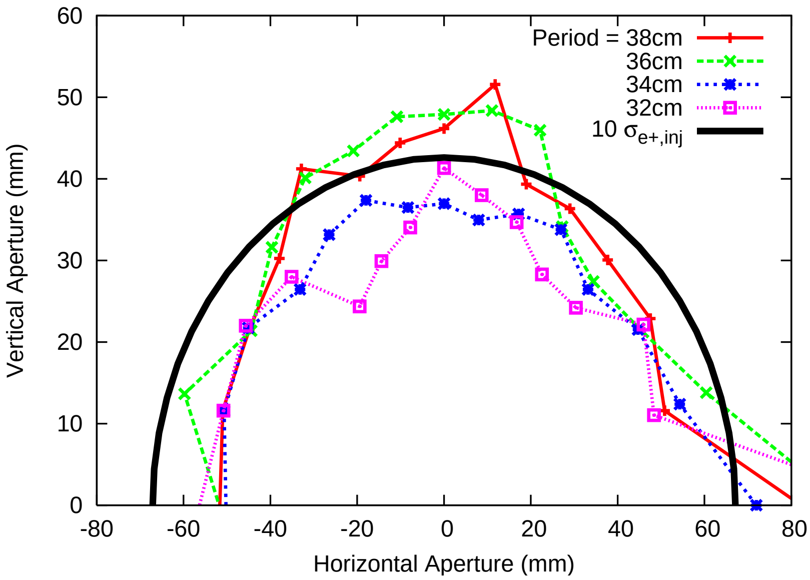

Figure 7.9: Dynamic aperture results for a range of wiggler periods of a full non-linear model of the 12-pole simplified modified CESR-c wiggler, with peak field set to fix $\tau_{damp} = 25\,\text{ms}$.

peak fields raised accordingly ($1.70 - 1.95\,\text{T}$) to achieve a 25 ms damping time. The performance of these wiggler models is shown in version 2.0 of the OCS damping ring lattice in Figure 7.9 and Table 7.4.

Including all of the wiggler nonlinearities in the shorter period models confirms that no significant decrease in dynamic aperture exists from $40 - 32\,\text{cm}$. Table 7.4 shows that reducing the period and pole number from 40 cm with 14-poles to 32 cm with 12-poles still meets the target horizontal emittance. However, raising the peak

Table 7.4: Wiggler and lattice parameters for the full nonlinear model of shorter period designs of the 12-pole simplified modified CESR-c wiggler.

λ (cm)	**38**	**36**	**34**	**32**
B_0 (T)	1.70	1.77	1.85	1.95
τ_{damp} (ms)	26.0	25.9	26.1	25.7
$\epsilon_{x,rad}$ (nm · rad)	0.59	0.58	0.56	0.55

field to meet the target damping time with the same number of wigglers proved difficult without sacrificing the target radiation equilibrium horizontal emittance. Therefore, none of these wiggler configurations meet the target damping time without adding wigglers to the ring and changing the baseline lattice design.

Finally, comparing dynamic aperture results for the ideal nonlinear (see Figure 7.7) and full nonlinear (see Figure 7.9) wiggler models with $\lambda_w = 38 - 32\,\mathrm{cm}$ shows reasonable agreement. This validates the initial assumption that the inherent octupole-like vertical nonlinearity will dominate the damping ring's performance as the wiggler period is decreased.

Recommendation

Given these dynamic aperture results, a 32 cm wiggler looks to be above the period where the dynamic aperture starts to degrade. Reducing the period and pole number from 40 cm with 14-poles to 32 cm with 12-poles corresponds to a 31 % reduction in total wiggler length which will greatly reduce the wiggler unit cost.

The damping time from a 32 cm, 12-pole wiggler is 3 % higher than the target; therefore, in a 200 ms storage cycle, the beam will be damped for $7.8\,\tau_{damp}$ instead of $8\,\tau_{damp}$. This will result in very little decrease in the radiation equilibrium emittance and should be an acceptable trade-off given that a 31 % reduction in total wiggler length corresponds to about a 25 % reduction in the cost of this superferric wiggler. Compared to the modified CESR-c wiggler which would cost nearly $500,000/wiggler, implementing this length reduction for 160 ILC damping wigglers will save $20 million which is considerable enough to recommend that the ILC damping wiggler be designed with 12-poles and a 32 cm period.

Table 7.5: Parameters achieved after combining the individual optimization recommendations into a superferric ILC-optimized CESR-c wiggler.

Parameter	**Unit**	**Value**
Peak Field	T	1.95
Number of poles		12
Total length	m	1.68
Period	m	0.32
Pole Width	cm	23.8
Gap Height	cm	8.6
$\Delta B/B_0$ at $x = 10\,\mathrm{mm}$		6.0×10^{-4}
Coil Current	A	141
Beam Energy	GeV	5

7.8 Optimization Conclusions

Taking the recommendations of each of the individual optimizations and combining them into a fully optimized and consistent wiggler model gives the wiggler description in Table 7.5. By reducing the number of poles and shortening the wiggler period at the same time as raising the wiggler field, 31 % less wiggler will be needed in the damping ring. This will result in significant cost savings during construction and operation. The wiggler unit length has been shortened to a value close to that of the CESR-c wiggler, thus eliminating the engineering challenge of constructing a wiggler considerably longer than the proven CESR-c design. Additionally, a shorter wiggler length provides additional space between subsequent wigglers for radiation absorbers. Finally, a larger vertical pole gap has simplified the engineering challenge into a process that could be feasibly mass produced.

Combining the results of each of the optimizations required a final consistency check when designing the magnet in Radia. For example, the minimal degradation of machine performance would allow $g_p > 86\,\mathrm{mm}$, but the results of the length and peak field optimization require $g_p \leq 86\,\mathrm{mm}$. This is because at $g_p = 86\,\mathrm{mm}$, the current had to be raised to the CESR-c operational limit (141 A) in order to produce a field that gave $\tau_{damp} \approx 25\,\mathrm{ms}$ with 31 % less wiggler in the ring.

This new wiggler model remains similar in basic design to the superferric CESR-c wigglers, but has been optimized for cost and performance in the ILC damping ring. Thus, it is called the superferric ILC-optimized CESR-c (SIOC) wiggler. The performance of the SIOC wiggler in the ILC damping rings will be given in the following chapter.

Chapter 8

ILC-Optimized Wiggler Performance

Throughout the ILC wiggler studies, the CESR-c superferric wiggler performed very well. A significant improvement in the dynamic aperture of the TESLA damping ring was observed after a replacement of the TESLA wiggler with a modified version of the CESR-c wiggler. The modified CESR-c wiggler has performed well in all versions of the OCS baseline damping ring lattice.

Performing variations of independent parameters of the CESR-c wiggler has revealed a number of possible modifications to the CESR-c design that reduce the cost of the final ILC damping wiggler. This wiggler design has features that are based closely on the existing superferric CESR-c wigglers, therefore proving the feasibility of overcoming the engineering challenges and risks that would potentially be faced during construction, installation, and operation of 160 of these wigglers in the ILC damping rings.

The parameters of this superferric ILC-optimized CESR-c (SIOC) wiggler are given in Table 7.5. The lattice parameters resulting from using the SIOC wiggler in version 2.0 of the OCS damping ring are given in Table 8.1. This shows that by combining the results of each independent magnet parameter optimization into

Table 8.1: Wiggler-related lattice parameters in version 2.0 of the OCS damping ring lattice, using the full nonlinear model of the SIOC wiggler.

τ_{damp}	$26.4\,\mathrm{ms}$
$\epsilon_{x,rad}$	$0.56\,\mathrm{nm}\cdot\mathrm{rad}$
σ_δ	$0.13\,\%$

the final SIOC wiggler, the exact impact of the wiggler on the damping ring beam parameters is not the same as the individual optimizations suggested.

For example, the emittance and energy spread targets are still satisfied but the damping time of 26.4 ms is larger than the 25.7 ms damping time achieved in the period optimization study. This difference came once the recommendation from the gap optimization study was combined with the recommendation from the period optimization study. At a 86 cm pole gap, the peak field could not be increased beyond 1.95 T to reduce the damping time without exceeding the CESR-c wigglers' operational current limit of 141 A. The superconducting quench limit is at a higher current now that the SIOC wiggler field strength is lower than the CESR-c wiggler field strength; however, even with the same current limit, a slightly larger damping time is still an acceptable trade-off given the cost-savings the SIOC wiggler provides.

The following sections detail the performance of the SIOC wiggler in version 2.0 of the OCS damping ring. Comparing results for the linear, ideal nonlinear, and full nonlinear models of the SIOC wiggler revealed additional information about the performance and limitations of this design.

8.1 Dynamic Aperture

The dynamic apertures of linear, ideal nonlinear, and full nonlinear wiggler models of the SIOC wiggler are presented in Figure 8.1. The nonlinear wiggler models produce dynamic apertures that, while below the linear wiggler aperture, are still greater than eight times the injected positron beam size. An $8 \times \sigma_{e+,inj}$ dynamic aperture provides an acceptable performance level for the ILC damping ring with a realistic nonlinear model of 80 damping wigglers.

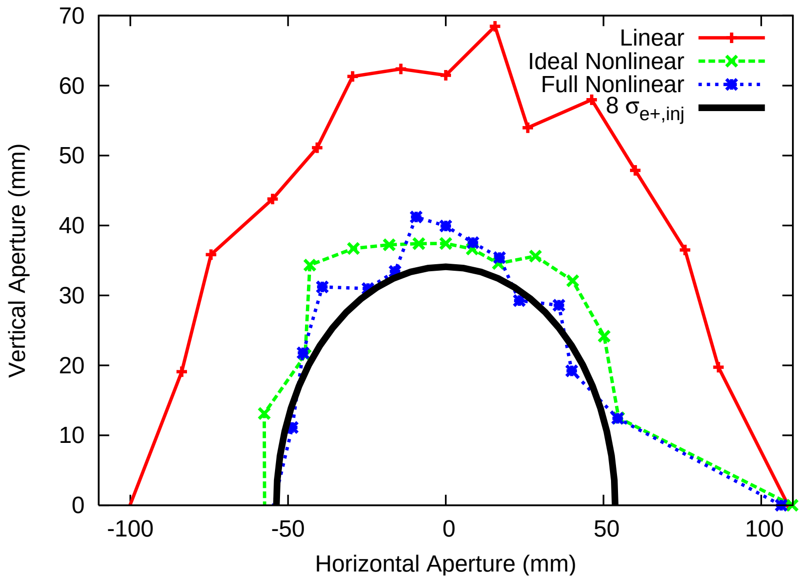

Figure 8.1: Dynamic aperture results for the linear, ideal nonlinear, and full nonlinear models of the SIOC wiggler.

Additionally, Figure 8.1 shows that the full nonlinear SIOC wiggler performs as well in version 2.0 of the baseline damping ring lattice as the ideal nonlinear wiggler model. Therefore, the dynamic aperture limitation produced by the SIOC wiggler is dominated by the vertical octupole-like nonlinearity inherent in all wigglers. The parameters of the SIOC wiggler have been successfully chosen to minimize the realistic wiggler nonlinearities coming from field roll-off and fringe fields, even with a vertical field roll-off of $\Delta B/B_0 = 6.0 \times 10^{-4}$ at $x = 10\,\mathrm{mm}$.

The off-energy performance of the full nonlinear model of the SIOC wiggler is presented in Figure 8.2. The SIOC wiggler provides as large a dynamic aperture ($8 \times \sigma_{e+,inj}$) for particles that deviate from the design energy by $\Delta p/p = 0.5\,\%$ and $1.0\,\%$ as particles on the design energy. Larger energy deviations including all models of the SIOC wiggler (see Figure 8.3) show that the full nonlinear SIOC wiggler meets the energy aperture requirements of the ILC damping ring.

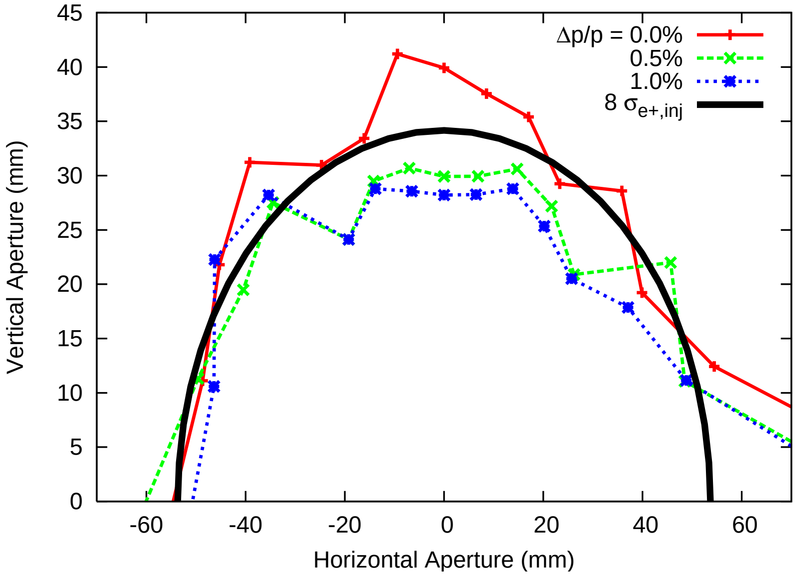

Figure 8.2: Off-energy dynamic aperture results for the full nonlinear model of the SIOC wiggler.

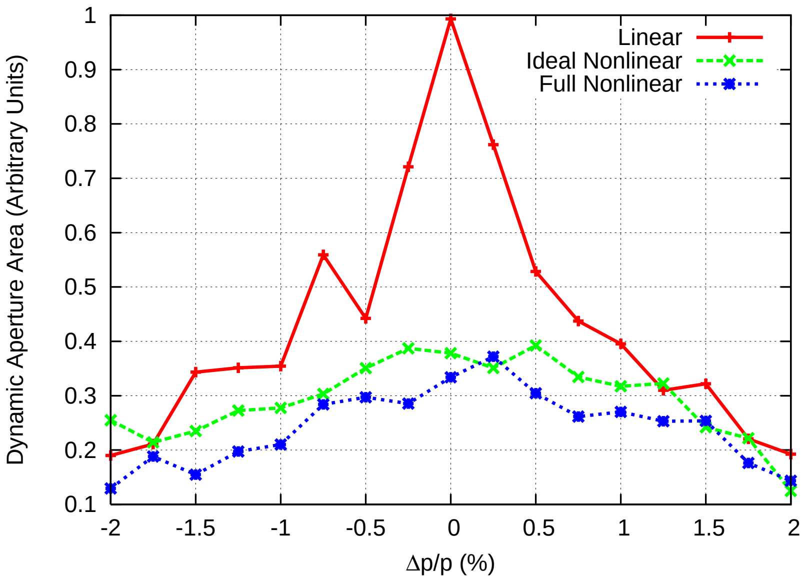

Figure 8.3: Energy aperture results for the linear, ideal nonlinear, and full nonlinear models of the SIOC wiggler.

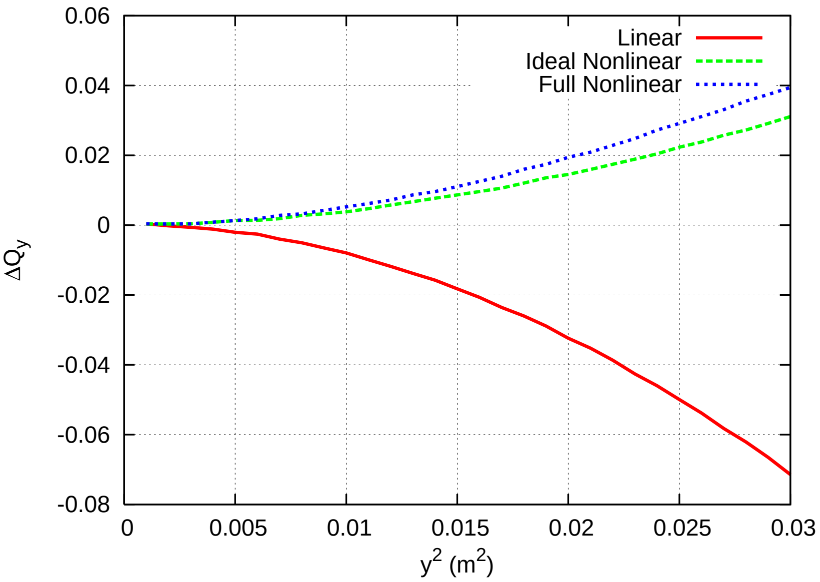

Figure 8.4: Tune versus amplitude results for the linear, ideal nonlinear, and full nonlinear models of the SIOC wiggler.

8.2 Frequency Map Analysis

Like the dynamic aperture, the vertical tune shift with vertical amplitude for all models of the SIOC wiggler confirms that the wiggler is well designed to minimize the impact of realistic wiggler nonlinearities on the ILC damping ring performance (see Figure 8.4). This result shows that there is a small difference in tune shift with amplitude between the full nonlinear and the ideal nonlinear wiggler models. Therefore, the SIOC wiggler's realistic nonlinearities produce a measurable impact on the beam dynamics, but not enough to adversely influence the dynamic aperture.

All of these results are confirmed with the frequency map results given in Figures 8.5-8.7. The frequency map results couple the tune shift with amplitude to the dynamic aperture to provide a detailed picture of where the performance of the ring is being degraded. These results show that the nonlinearities of the

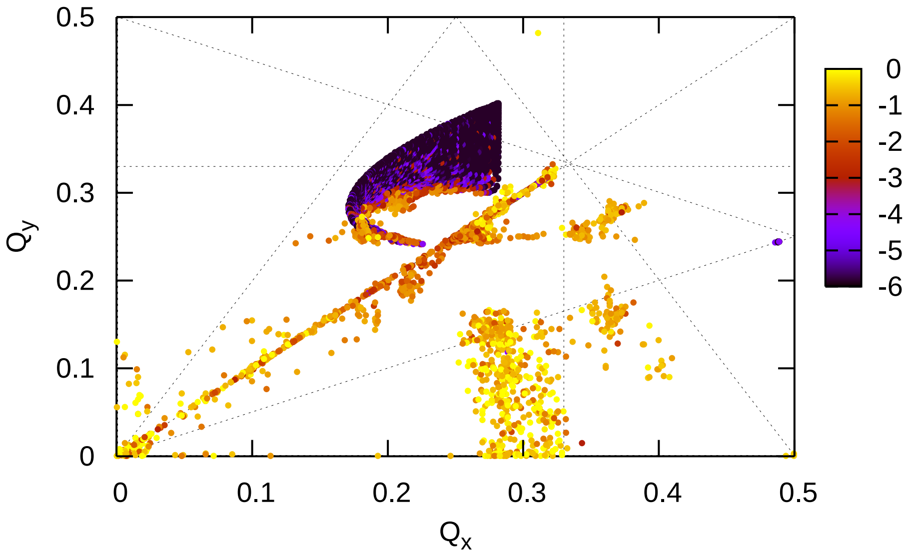

Figure 8.5a: Frequency map analysis result in tune-space for the linear model of the SIOC wiggler. Operating point is $Q_x = 0.28$, $Q_y = 0.40$.

SIOC wiggler are moving the tune across resonances as the particles increase in amplitude. When compared with the frequency map analysis result for the linear wiggler model, the dominant wiggler nonlinearity is responsible for the majority of the changes to the dynamic aperture and tune plane. However, the realistic wiggler nonlinearities do manifest themselves in Figure 8.7b as large amplitude particles that have a lighter intensity. These particles are inside the dynamic aperture but have tunes that are changing (lighter intensity), though not fast enough to cause a limitation to the dynamic aperture. This suggests that the damping ring with the SIOC wiggler might be more susceptible to field errors or magnetic misalignments in the ring dipoles, quadrupoles, and sextupoles, which could reduce the dynamic aperture by perturbing those nearly chaotic but stable particles into chaotic and unstable trajectories.

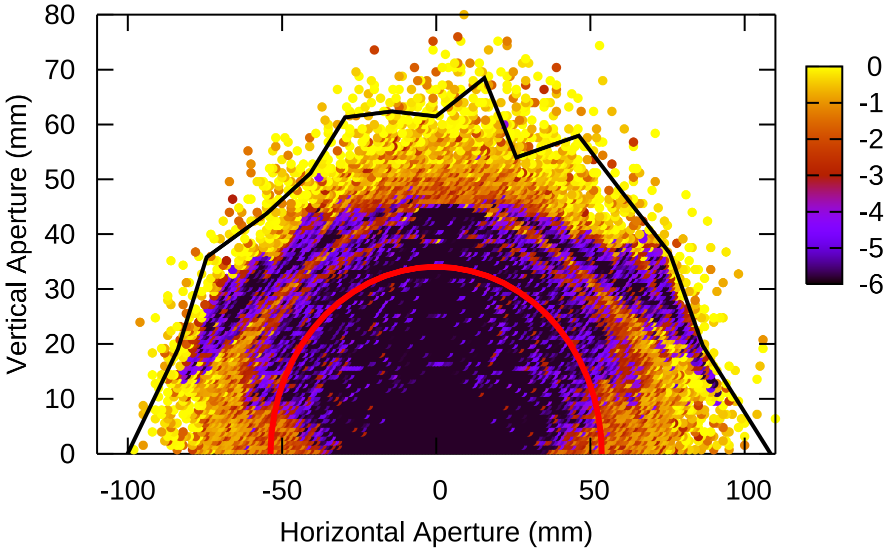

Figure 8.5b: Frequency map analysis result in physical-space for the linear model of the SIOC wiggler. The lines show the standard dynamic aperture limit (dashed) along with the 8σ curve (solid).

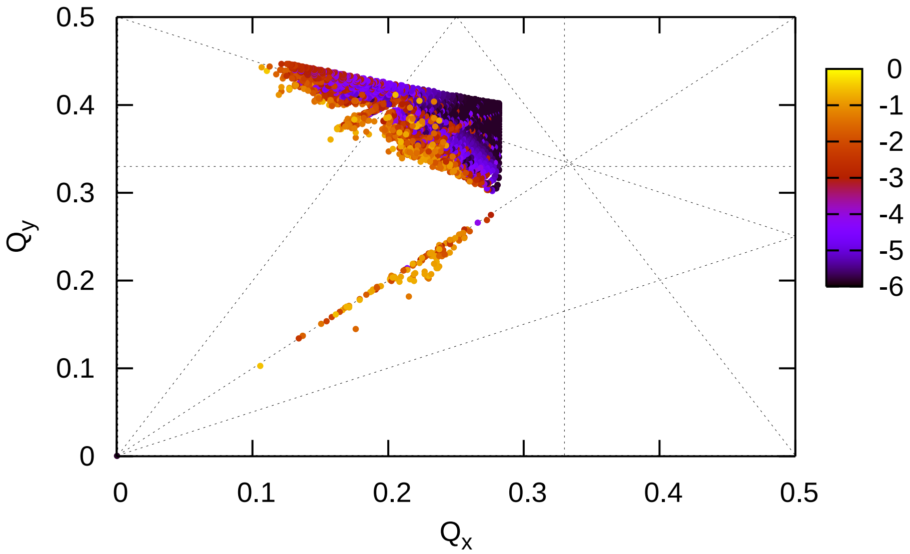

Figure 8.6a: Frequency map analysis result in tune-space for the ideal nonlinear model of the SIOC wiggler. Operating point is $Q_x = 0.28$, $Q_y = 0.40$.

8.3 Multipole Field Errors

Further simulations examined the performance of the ILC damping ring with nonlinearities coming from both the SIOC wiggler and higher-order multipole field errors on the dipoles, quadrupoles, and sextupoles. Simulations reveal that in this condition, the full nonlinear SIOC wiggler does not reduce the on-energy dynamic aperture below that of the limit imposed by the combination of the multipole field errors with a linear wiggler model (see Figure 8.8). For an off-energy beam experiencing higher-order multipole field errors in the ring magnets, the full nonlinear SIOC wiggler produces a minimal dynamic aperture degradation compared to the performance of a linear wiggler model (see Figure 8.9).

These results show that multipole field errors on the ring magnets limit the amplitude of the dynamic aperture, even when a realistic wiggler model is included.

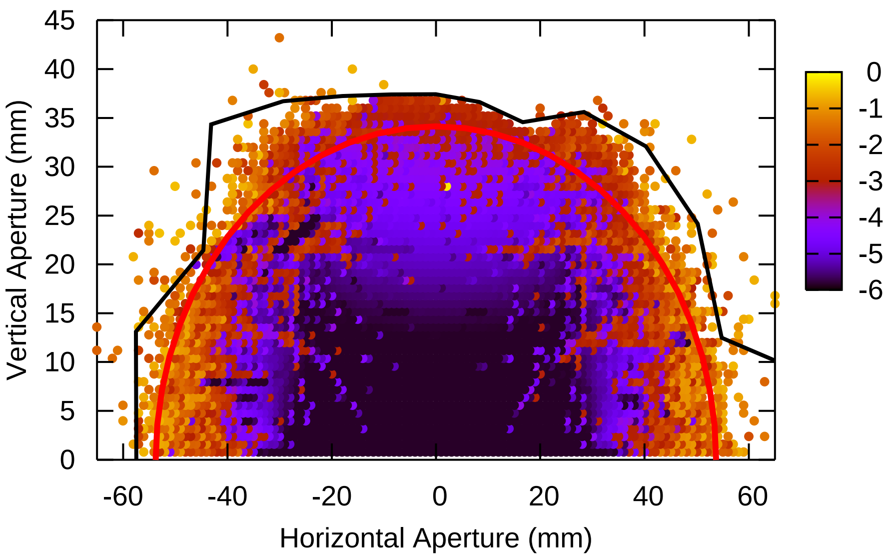

Figure 8.6b: Frequency map analysis result in physical-space for the ideal nonlinear model of the SIOC wiggler. The lines show the standard dynamic aperture limit (dashed) along with the 8σ curve (solid).

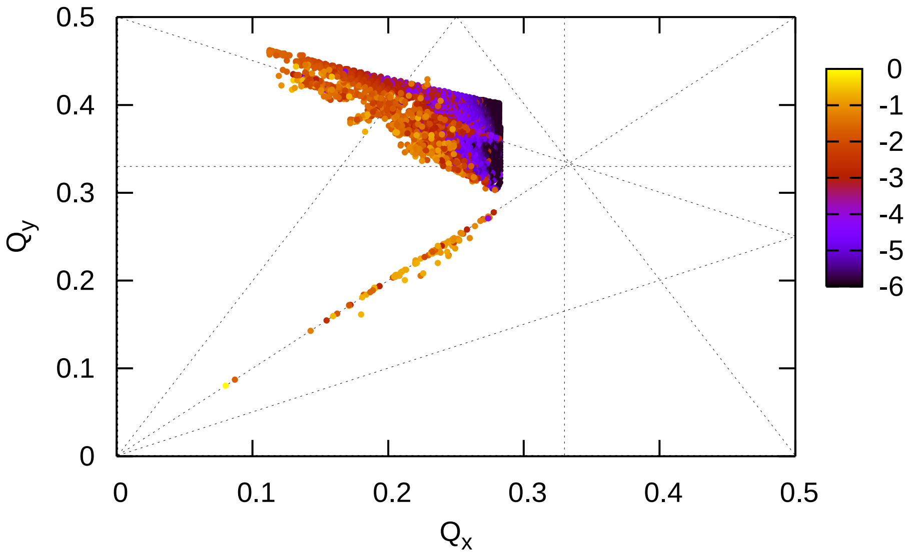

Figure 8.7a: Frequency map analysis result in tune-space for the full nonlinear model of the SIOC wiggler. Operating point is $Q_x = 0.28$, $Q_y = 0.40$.

Therefore, the potential susceptibility of the SIOC wiggler to other errors (that was hinted at in the frequency map analysis results) was not revealed with these multipole field errors. Additionally, even with these strong field errors the dynamic aperture is limited to $5 \times \sigma_{e+,inj}$ which is an acceptable aperture for a ring that includes realistic performance limiting effects like magnet errors and wiggler nonlinearities.

8.4 Performance Conclusions

All of the previous results show that optimizing the CESR-c wiggler for operation in the ILC damping ring yields a magnet which provides practical cost and engineering benefits without any significant degradation of beam dynamics and machine performance. Further, since the full nonlinear model does not reduce

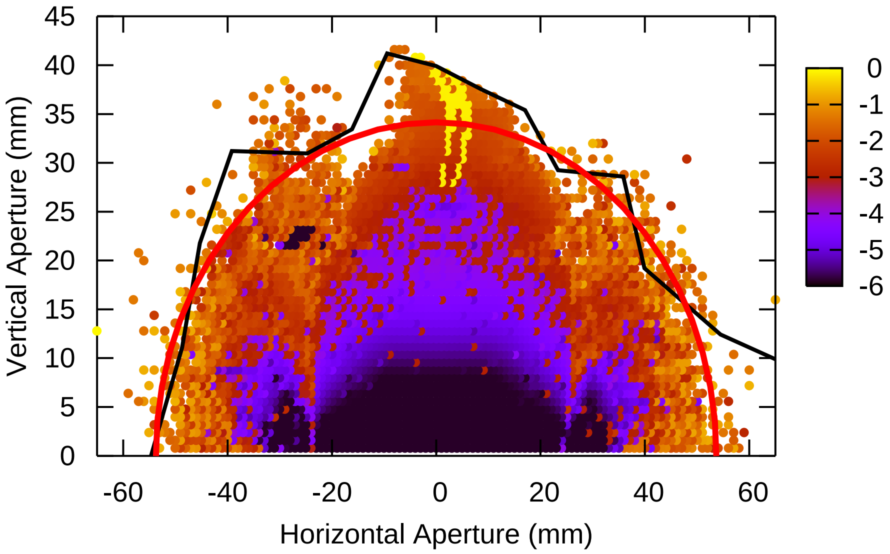

Figure 8.7b: Frequency map analysis result in physical-space for the full nonlinear model of the SIOC wiggler. The lines show the standard dynamic aperture limit (dashed) along with the 8σ curve (solid).

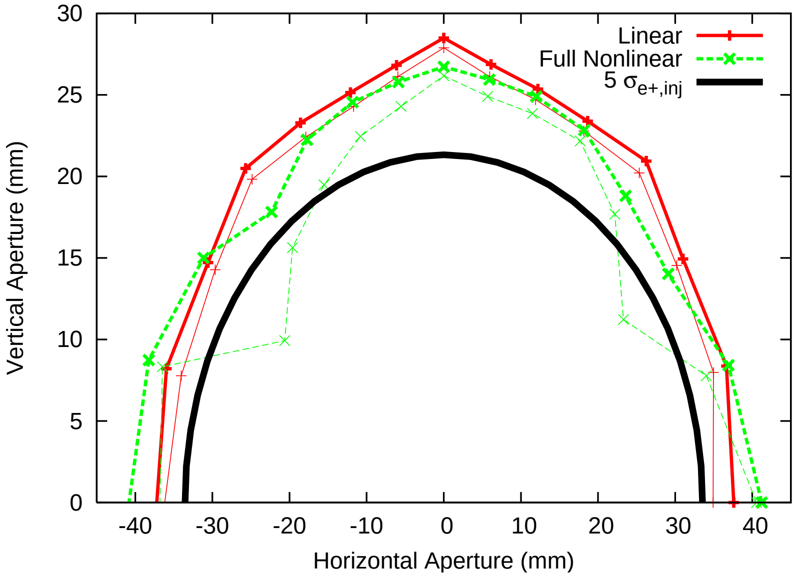

Figure 8.8: Dynamic aperture results, with multipole field errors included on dipole, quadrupole, and sextupole magnets, for the linear and full nonlinear models of the SIOC wiggler.

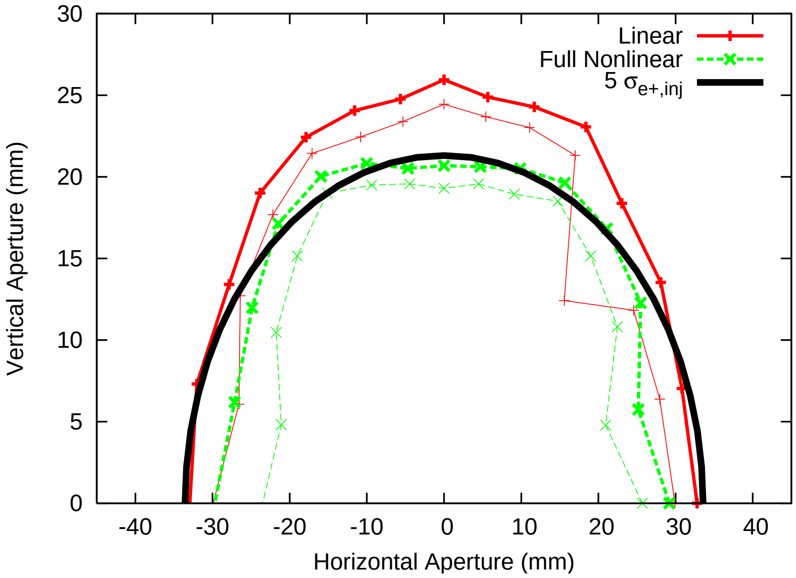

Figure 8.9: Off-energy dynamic aperture results, $\Delta p/p = 1\,\%$, with multipole field errors included on dipole, quadrupole, and sextupole magnets, for the linear and full nonlinear models of the SIOC wiggler.

the dynamic aperture beyond that of the ideal nonlinear model, the SIOC wiggler was well designed to minimize realistic wiggler nonlinearities. In conclusion, the advantages and performance of the SIOC wiggler motivates selecting this wiggler design as the baseline superferric ILC wiggler.

8.5 Next Steps

The next step in a complete wiggler design is to optimize the coil curvature and pole cutouts to reduce the vertical field roll-off from its value of 6.0×10^{-4} at $x = 10\,\text{mm}$. Optimizing both the precise coil curvature and pole cutout designs was required to achieve a field roll-off of 7.7×10^{-5} in the CESR wigglers. Reducing the roll-off will not improve the simulated performance of the SIOC wiggler since the full nonlinear model does not reduce the simulated dynamic aperture beyond that of the ideal nonlinear model; however, minimizing the roll-off is potentially crucial for allowing a sufficient margin of error during operation of a real accelerator.

Another lesson learned from operating the superferric wigglers in CESR, was that optimizing the sextupole distribution was required to minimize the dynamic aperture reduction caused by the wigglers. Sextupole fields cannot completely correct the magnetic fields in the wigglers that cause nonlinearities in the particles' trajectories, however, in the operation of CESR they nevertheless proved useful. The overall design of this version of the OCS lattice, including sextupoles, was optimized to provide a very large dynamic aperture, but this was completed with a linear wiggler model. Using a nonlinear model of the SIOC wiggler during sextupole and lattice design optimizations could potentially produce a maximum dynamic aperture with different sextupole settings.

Finally, realizing this conceptual design in the ILC damping ring requires the construction of a prototype. The significant experience and tools developed at Cornell for the twelve superferric wigglers in CESR would be valuable to the construction of a prototype ILC damping wiggler. Constructing the ILC damping wiggler prototype would be a significant multi-year man-power investment, but there would be minimal additional hardware research and development required if the Cornell resources were fully utilized. This would be a straightforward research and development project and should be feasible given Cornell's interest and the approval of the global ILC organization.

Chapter 9

Conclusions

Specifying the technical design of the International Linear Collider has been a complex on-going process involving years of productive international collaboration. Optimal performance of the ILC damping rings is crucial for producing collisions between beams of electrons and positrons that are useful to experimental particle physicists looking for the Higgs boson and other new physics. Within the damping rings, the wigglers are a particularly challenging component. This dissertation provides the conceptual design of the first wiggler to meet both the physics and engineering requirements of the ILC damping rings.

9.1 The ILC Damping Wiggler

Wigglers will be used in the ILC damping rings to speed the emission of synchrotron radiation from a 5 GeV, 6 km ring. The damping rings must damp the electron and positron beams to $\gamma\epsilon_x = 8\,\mu\mathrm{m}\cdot\mathrm{rad}$ and $\gamma\epsilon_y = 0.02\,\mu\mathrm{m}\cdot\mathrm{rad}$ in 200 ms, requiring the installation of hundreds of meters of wiggler magnets. Using this many wigglers has the potential to greatly complicate the performance of the damping rings due to strong wiggler nonlinearities. The poor beam dynamics produced by wigglers come from an inherent vertical nonlinearity as well as realistic nonlinearities which can be minimized with the proper choice of magnet parameters.

The wiggler design proposed in this dissertation is based on the 2.1 T superferric wigglers that are operating with minimal degradation of the beam dynamics in the Cornell Electron Storage Ring (see Table 9.1). The performance of this magnet in the ILC was compared against a proposed permanent magnet wiggler designed by the TESLA damping ring collaboration (see Table 9.1).

Replacing the TESLA wiggler with a modified version of the CESR-c wiggler significantly improved the dynamic performance of the TESLA damping ring. This wiggler performed so well because its nonlinearities are dominated by the inherent nonlinearity and the specific pole design of the CESR-c wiggler produces low levels of realistic wiggler nonlinearities. The superferric, modified CESR-c wiggler continued to perform at this high level in all candidate ILC damping ring lattices.

9.2 The ILC-Optimized Wiggler

The modified CESR-c wiggler met the physics performance requirements of the ILC damping rings and some, but not all, of the technical engineering requirements. With 160 superconducting wigglers in the ILC damping rings, the technical requirements during construction, installation, and performance will be on an entirely different scale than the twelve wigglers operating in CESR. Therefore, optimizations were conducted on the peak field, unit length, period, pole width, and pole gap of the CESR-c wigglers in order to ease the technical requirements without compromising the physics performance of the ILC damping rings.

Optimizations achieved a superferric ILC-optimized CESR-c (SIOC) wiggler design that minimized the cost and technical engineering risks (see Table 9.1). Evaluating the physics performance of the SIOC wiggler in the baseline ILC damping ring showed that this wiggler continues to meet the targets for dynamic aperture, tune shift with amplitude, off-energy dynamics, and dynamics with multipole field errors.

Table 9.1: Parameters of the TESLA permanent magnet wiggler, the CESR-c superferric wiggler, and the superferric ILC-optimized CESR-c wiggler.

Parameter	**Unit**	**TESLA**	**CESR-c**	**SIOC**
Peak Field	T	1.67	2.1	1.95
Number of poles		18	8	12
Total length	m	3.6	1.3	1.68
Period	m	0.40	0.40	0.32
Pole Width	cm	6.0	23.8	23.8
Gap Height	cm	2.5	7.6	8.6
$\Delta B/B_0$ at $x = 10\,\text{mm}$		5.7×10^{-3}	7.7×10^{-5}	6.0×10^{-4}
Coil Current	A	NA	141	141
Beam Energy	GeV	5	2	5

9.3 Recommendations

With the results of the above magnet optimizations, a range of beam and lattice parameters are available with only slight changes to the design of the modified CESR-c wiggler. Modifications to the design of the CESR-c wiggler have reduced the cost per wiggler by roughly 25 %, saving approximately $20 million for the entire ILC project. Additionally, this conceptual design eases the technical risks and challenges associated with the mass-production of 160 ILC damping wigglers. Therefore, the superferric ILC-optimized CESR-c wiggler is recommended to be the baseline superferric ILC wiggler.

Additionally, the wiggler parameter optimizations performed here will provide crucial data to any future discussion of changes to the ILC damping wiggler. The results presented in this dissertation detail the full effect of realistic wiggler nonlinearities on the beam dynamics as the design parameters of the wiggler are varied. These results will be of use to the international ILC damping ring community even if the exact conceptual design recommended here is not selected as the ILC damping wiggler.

Appendix A

Wiggler Field-Fitting Benchmark

Benchmarking the particle accelerator simulation codes used by different scientists is an important component of validating initial simulation results. Computer simulations are a crucial part of particle accelerator design and operation, and, like the entire field of accelerator physics, this process is often very collaborative as it crosses the national and international accelerator laboratories. Therefore, benchmarking the computer programs developed and used by different scientists is a first step in validating the results and conclusions of the many different accelerator codes available.

The full nonlinear wiggler model described in Section 5.4.1 is only available in a limited number of accelerator codes utilized world-wide. In the codes where it does exist, the full nonlinear wiggler model is a relatively new addition and should be benchmarked against other codes. Three separate pieces of simulation code are required to achieve the full nonlinear wiggler model, they are the codes to generate a discrete table of magnetic field values, then to create an analytic fit to the wiggler field, and ultimately to track a charged particle through the specified wiggler field.

The discrete table of magnetic field values comes from Radia or OPERA-3d and for benchmarking purposes every researcher uses the same field table. In the case of the Cornell wigglers, the OPERA-3d magnetic field table has been extensively compared with experimental measurements of the field in the existing wigglers and detailed agreement has been verified. With this good agreement, the OPERA-3d field table of a version of the Cornell wiggler was used for studies to benchmark the field fitting and wiggler tracking procedures used in the ILC damping ring design community.

Detailed comparisons were performed between the field fitting and wiggler tracking procedures used throughout the ILC damping ring community [53] and in greater detail for two codes, Bmad [21] and COSY [54]. For Bmad, the Cornell-developed Cartesian-based iterative fitting methods described in Section 5.4.3 was used. For COSY, the field fit is generated in cylindrical coordinates by combining the field data on the surface of a cylinder which encloses the magnetic volume with the requirements of Maxwell's equations [55]. The wiggler tracking procedures in Bmad and COSY are slightly different but based on the same integration method to generate the map, it is a symplectic method developed by E. Forest [56].

To verify that the two codes produce the same map and tracking results given identical analytic representation of the magnetic field, particle tracking studies were compared for a single-mode wiggler. A single-mode wiggler is equivalent to the infinitely wide and long wiggler given in Equation 5.9. In this analysis the wiggler parameters used were $B_0 = 1.67\,\mathrm{T}$ and $k_w = 2\pi/0.4$. The coefficients of the Taylor maps generated by Bmad and COSY show very good agreement for all coefficients except the ones which are below 10^8 in COSY (see Figure A.1). This small difference is likely indicative of a difference in precision between Bmad and COSY and does not impact the wiggler-related results.

After agreement was shown for Bmad and COSY with identical single-mode wigglers, results were computed for the two codes for multi-mode fits performed separately to the same field data. Using the Cornell wiggler magnetic field data extending over a transverse region of $x = \pm 48\,\mathrm{cm}, y = \pm 26\,\mathrm{cm}$, field fits were generated from Bmad and COSY and compared. The Cornell iterative fitting method achieved residuals at the level of $|B_{fit} - B_{data}|_{rms} = 47\,\mathrm{G}$ with 136 terms

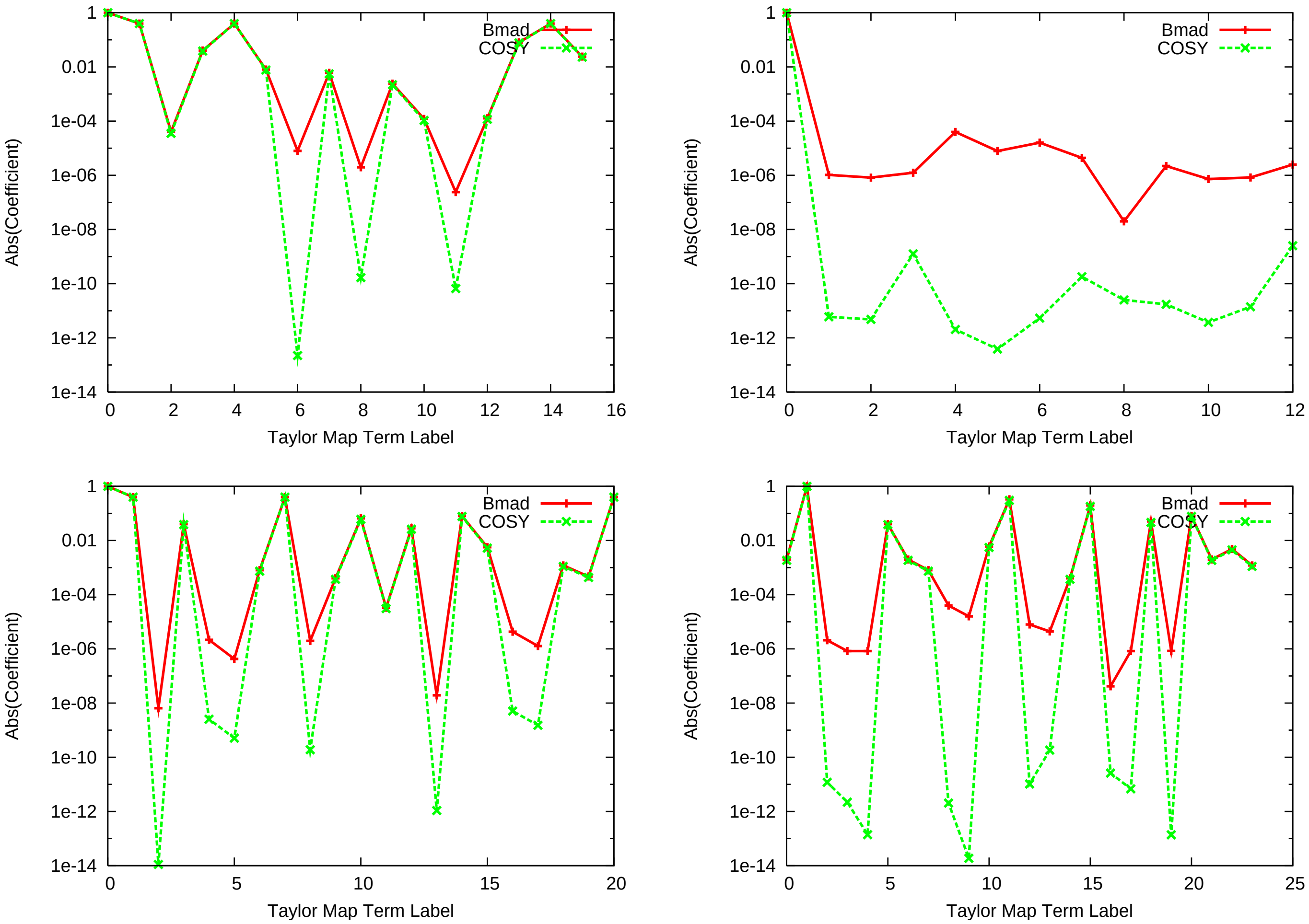

Figure A.1: Comparison of Bmad- and COSY-generated Taylor maps for a single-mode wiggler. Clockwise from top-left: x, p_x, p_y, y.

in the fit. The COSY method achieved lower residuals, reaching residuals below 1 G on-axis and up to only 10 G off-axis at $y = 26$ mm, which is the radius of the cylinder used for the field fit. Despite the significantly smaller residuals for the COSY-generated fit, the coefficients of the Taylor maps again show very good agreement (see Figure A.2) as do the on- and off-energy dynamic apertures results (see Figure A.3).

This reveals that the particle tracking results are not critically dependent on the precision of the magnetic field fit. Additionally, these results show reliable agreement between the wiggler field fitting algorithms and tracking procedures utilized in Bmad and COSY. Combined with results from other comparisons [53], there is high confidence in the wiggler simulation techniques utilized by the ILC damping ring design community.

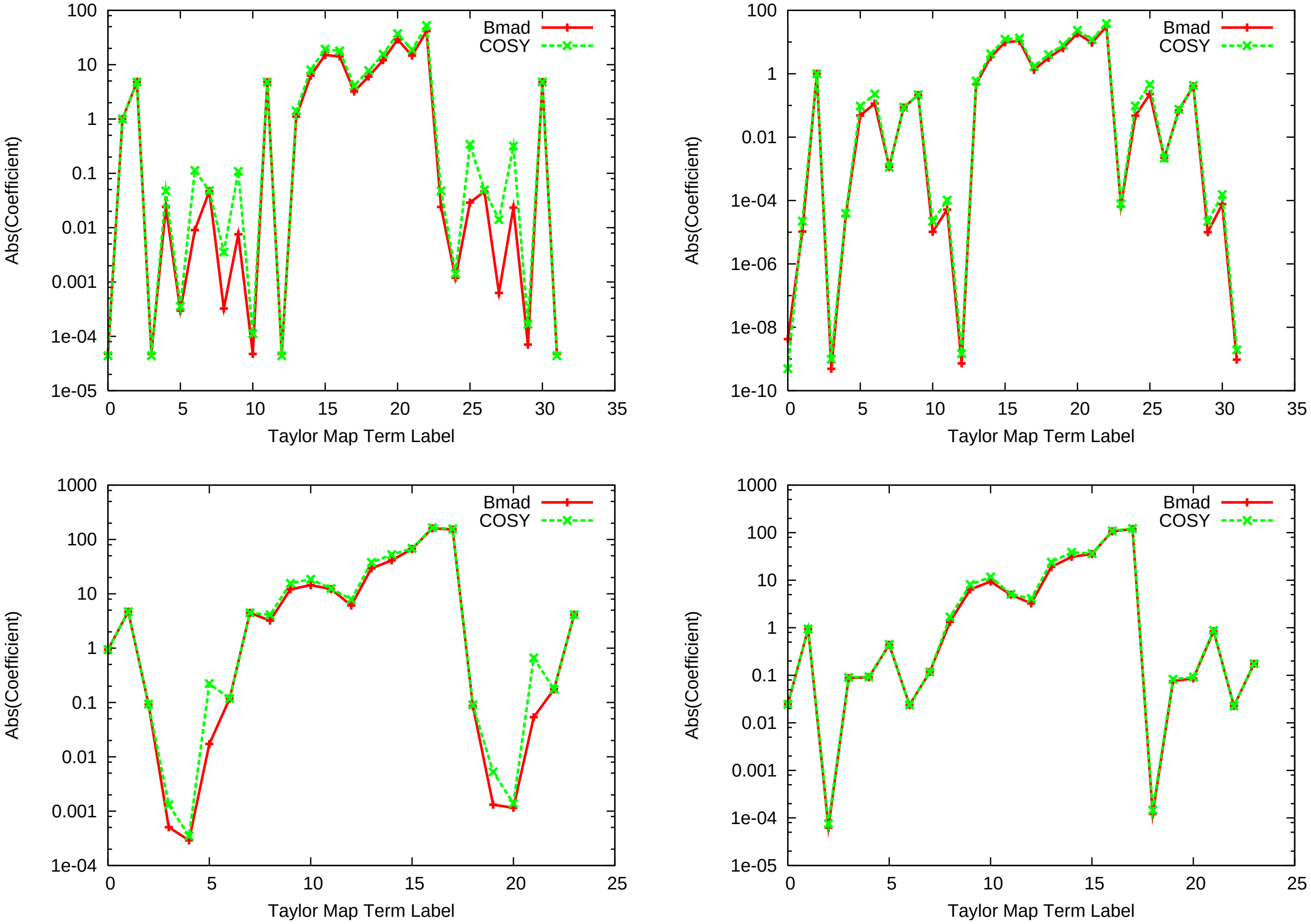

Figure A.2: Comparison of Bmad- and COSY-generated Taylor maps for a multi-mode wiggler. Clockwise from top-left: x, p_x, p_y, y.

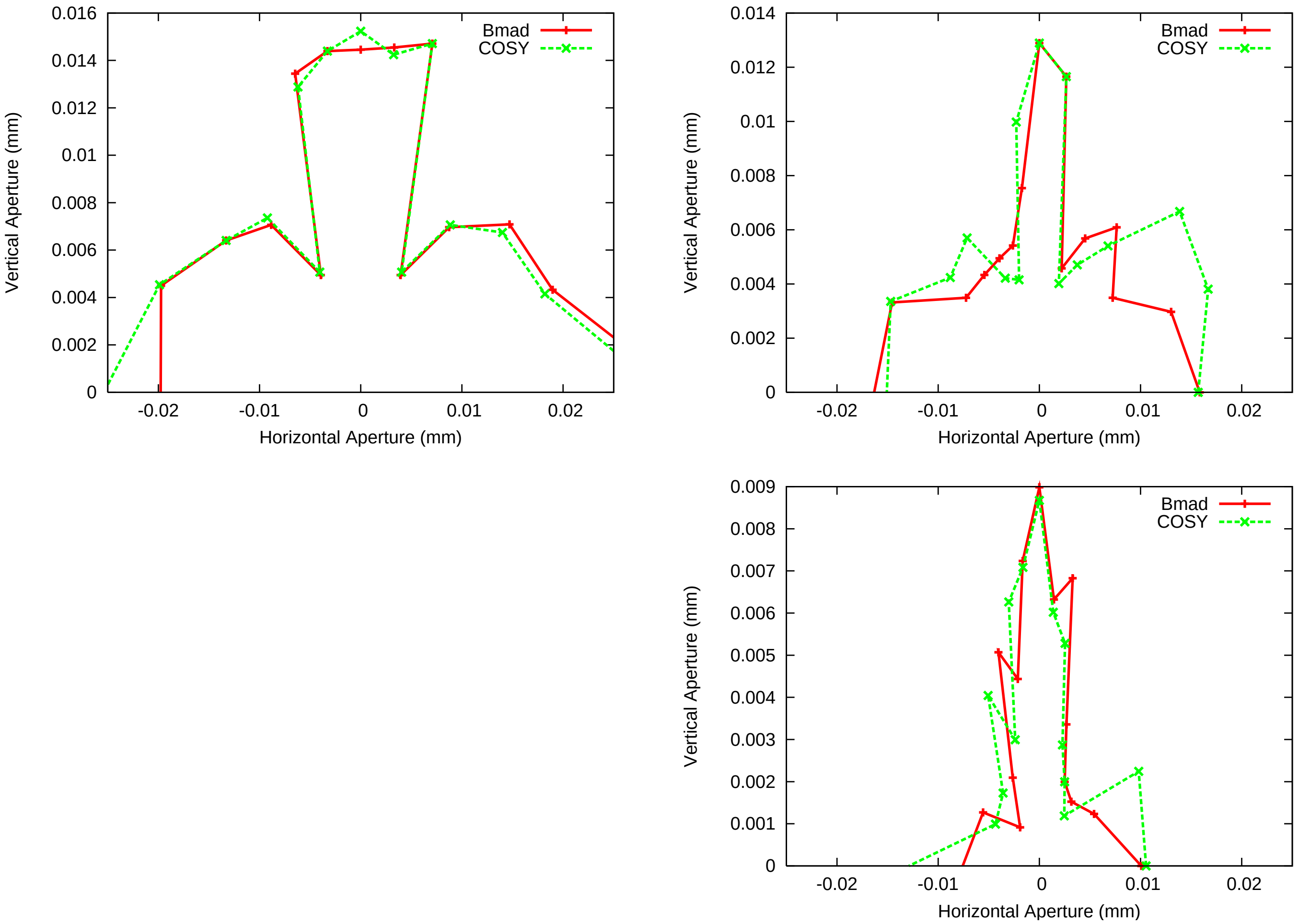

Figure A.3: Comparison of Bmad- and COSY-generated dynamic apertures for a multi-mode wiggler. Clockwise from top-left: $\Delta p/p = 0.0\,\%$, $\Delta p/p = 0.5\,\%$, $\Delta p/p = 1.0\,\%$.

Appendix B

Damping Ring Configuration Study

Dynamic aperture, dynamic aperture with multipole field errors, and frequency map analysis simulations were performed using the modified CESR-c wiggler in each of the seven damping ring configuration study lattices (see Table 4.4). Dynamic aperture results for the linear, ideal nonlinear, and full nonlinear models of the modified CESR-c wiggler in each of the seven lattices are given in Figure B.1. Dynamic aperture, with multipole field errors, results for the linear wiggler model are given in Figure B.2, and for the full nonlinear wiggler model in Figure B.3. Frequency map analysis results for the linear wiggler model are given in Figure B.4, and for the full nonlinear wiggler model in Figure B.5.

With the linear wiggler model and no multipole field errors all of the reference lattices achieve the aperture target of $3 \times \sigma_{e+,inj}$ (see Figure B.1). However, performances change as realities are added, including off-energy particles, nonlinear wiggler models, and multipole field errors on the dipoles, quadrupoles, and sextupoles. Frequency map analysis results reveal the tune resonances that are causing the dynamic aperture degradation with the linear (see Figure B.4) and full nonlinear (see Figure B.5) models of the modified CESR-c wiggler.

With the full nonlinear model of the modified CESR-c wiggler and multipole field errors on the main ring magnets, the BRU, MCH, OCS, and PPA lattices have a dynamic aperture larger than the 3σ target for particles off-energy by $\Delta p/p = 0.5\,\%$ (see Figure B.3). With even larger energy deviations ($\Delta p/p = 1.0\,\%$), only the OCS lattice has 99 % of the injected particles within the dynamic aperture. Very good agreement in all lattices between the ideal nonlinear and full nonlinear models confirms the initial result which came from the TESLA ring and determined the high quality of the CESR-c wiggler.

The nearly ideal performance of the modified CESR-c wiggler and the large dynamic aperture of the OCS lattice in all conditions was used as evidence to make some of the key decisions for the baseline configuration of the damping rings. Decisions included specifying a damping ring circumference of 6 km and a beam energy of 5 GeV, like the OCS ring, and using superferric technology for the damping wigglers, like the CESR-c wigglers. The complete analyses performed for the ILC damping ring baseline configuration study and the recommendations made by the collaboration are given elsewhere [12].

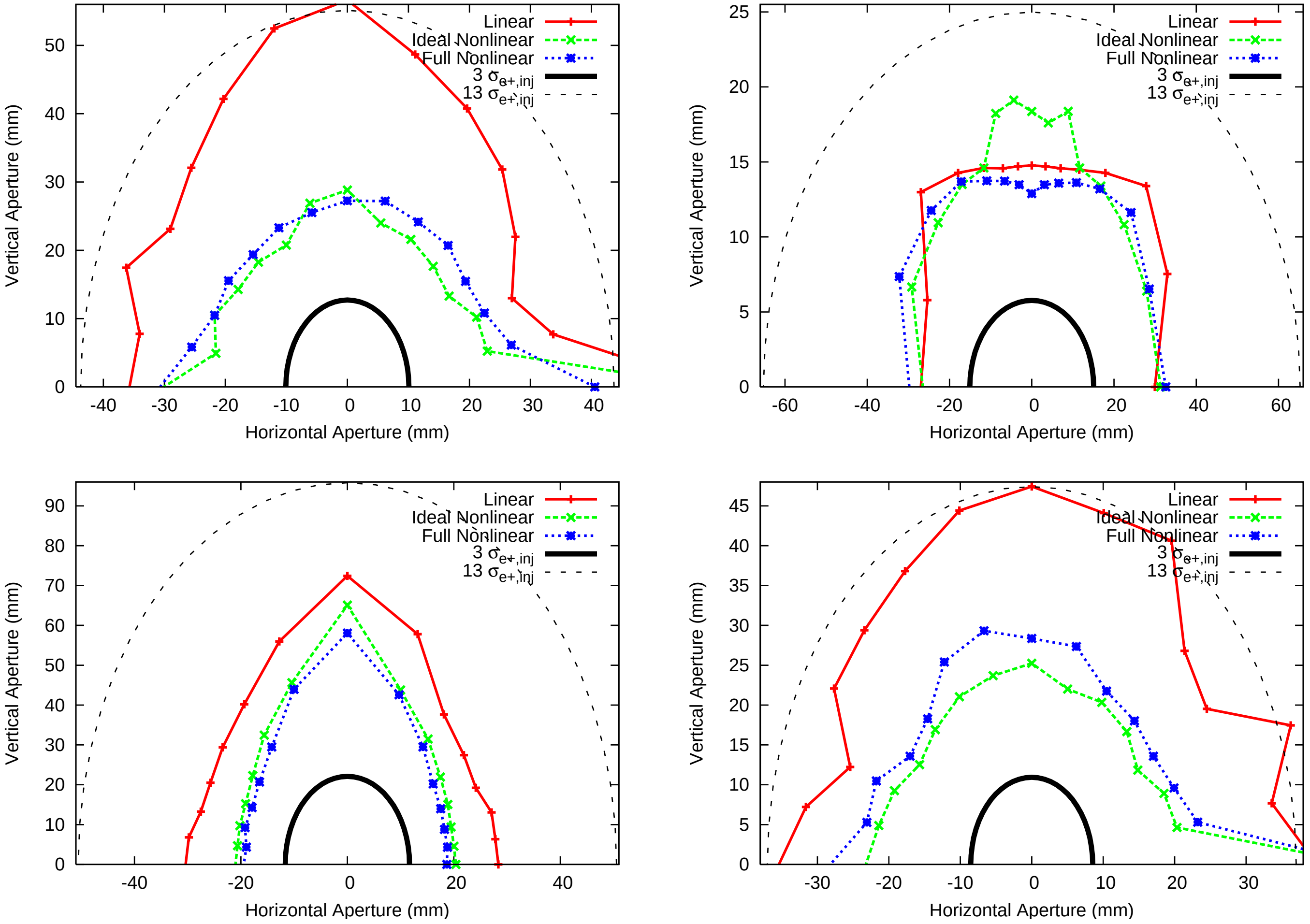

Figure B.1a: Dynamic aperture results for the linear, ideal nonlinear, and full nonlinear models of the modified CESR-c wiggler in lattices, clockwise from top-left: BRU, DAS, MCH, and OCS.

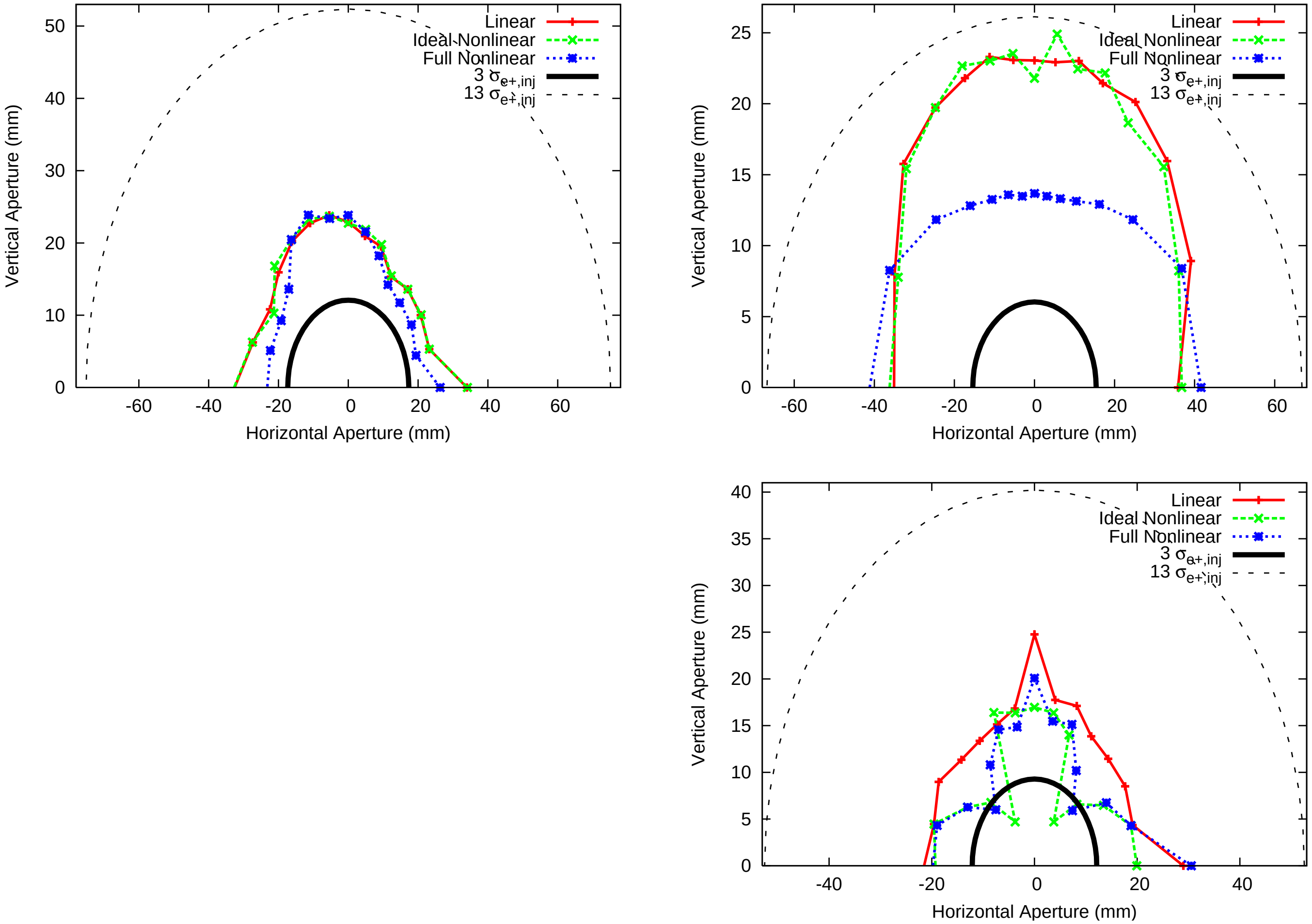

Figure B.1b: Dynamic aperture results for the linear, ideal nonlinear, and full nonlinear models of the modified CESR-c wiggler in lattices, clockwise from top-left: OTW, PPA, and TESLA.

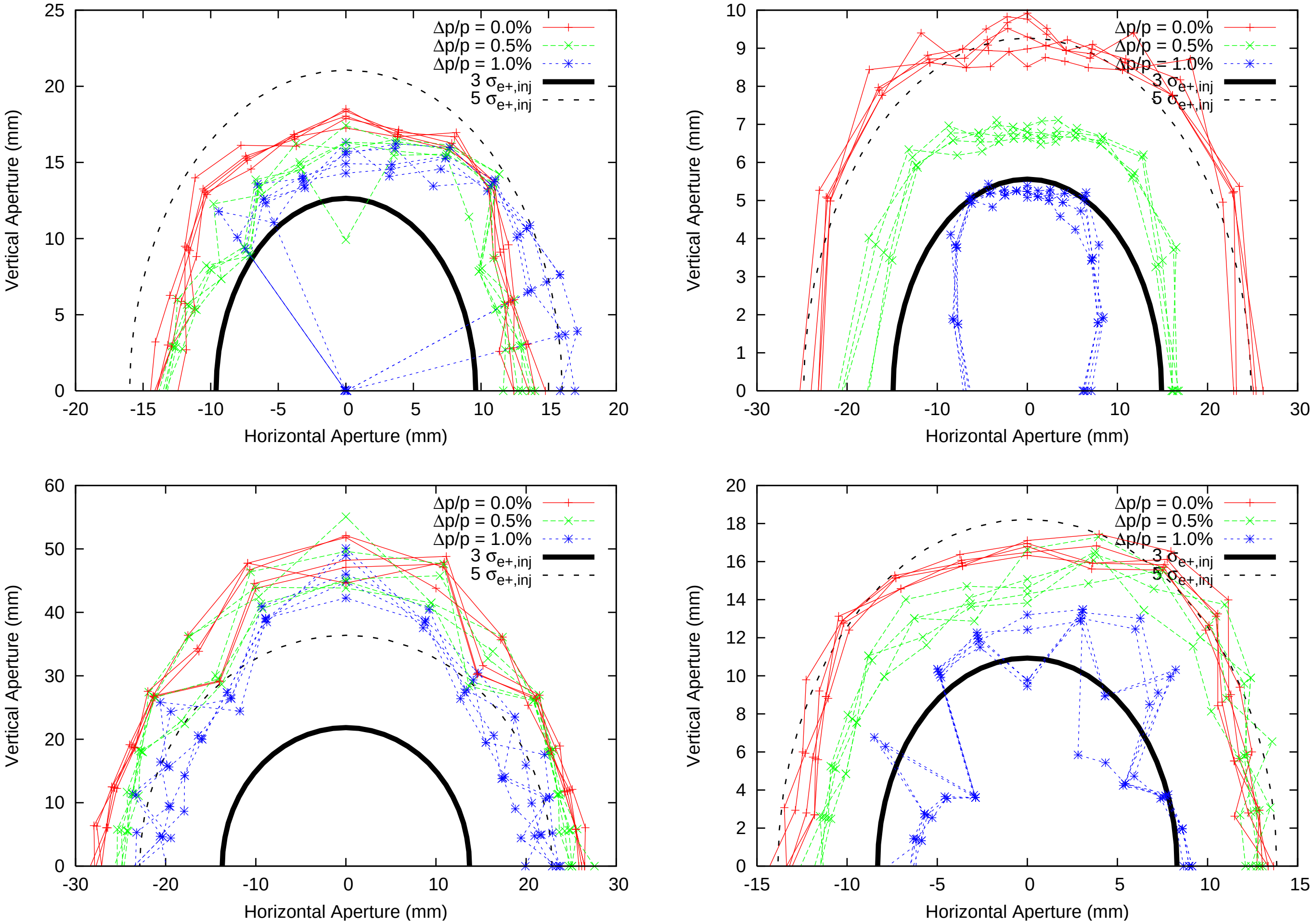

Figure B.2a: Dynamic aperture, with multipole field errors, results for the linear wiggler model of the modified CESR-c wiggler in lattices, clockwise from top-left: BRU, DAS, MCH, and OCS. Shown are results for five random error seeds.

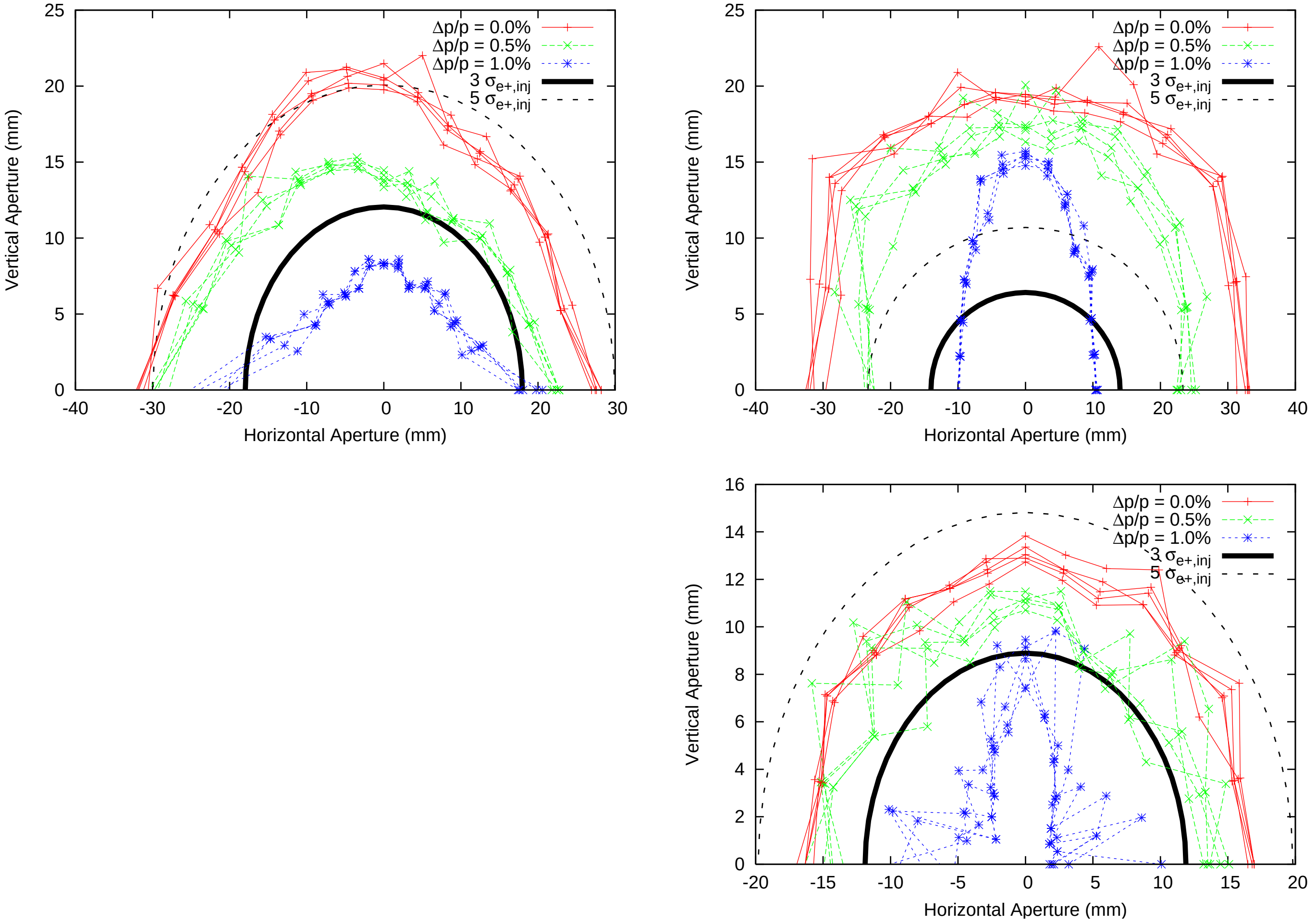

Figure B.2b: Dynamic aperture, with multipole field errors, results for the linear wiggler model of the modified CESR-c wiggler in lattices, clockwise from top-left: OTW, PPA, and TESLA. Shown are results for five random error seeds.

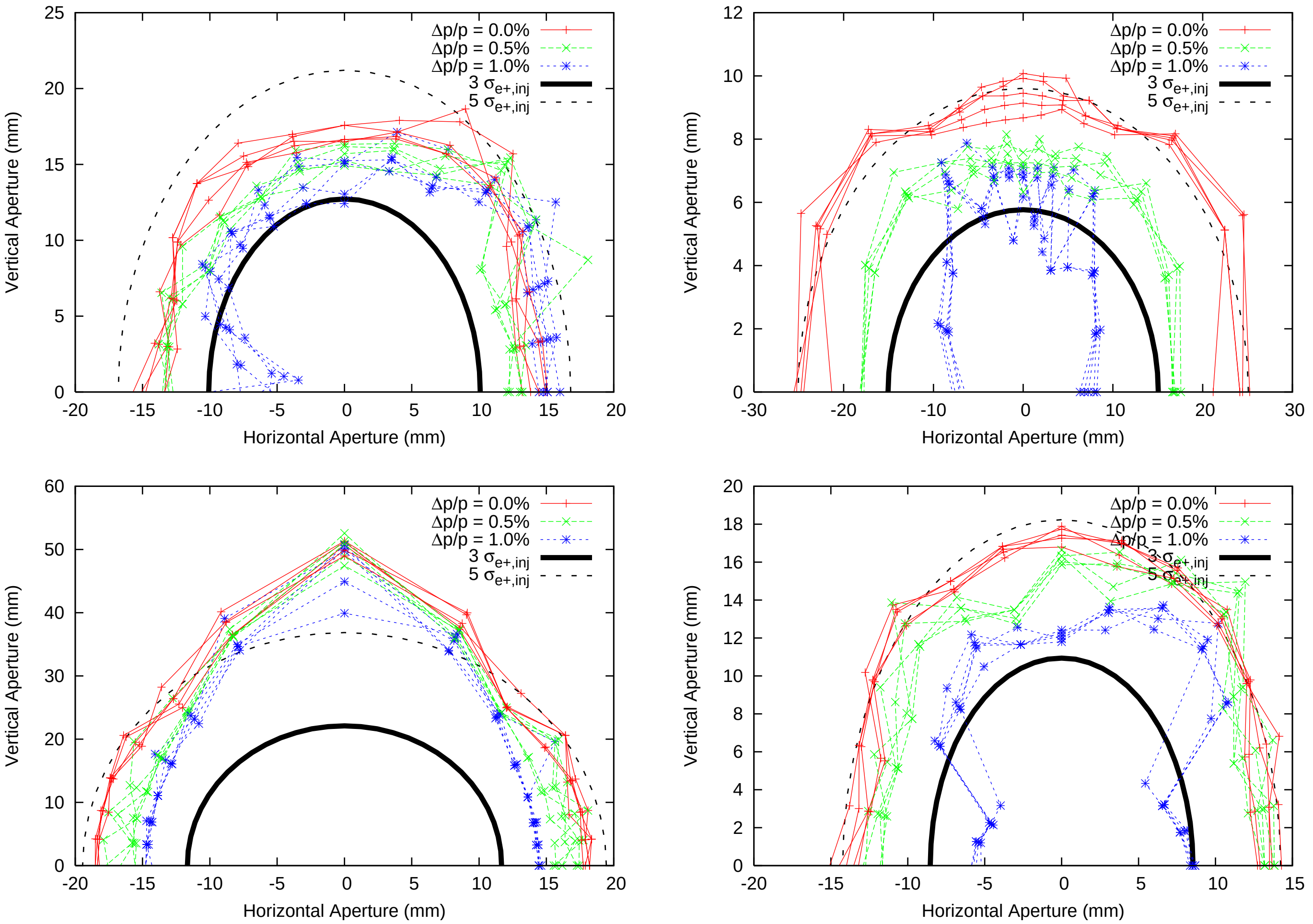

Figure B.3a: Dynamic aperture, with multipole field errors, results for the full nonlinear wiggler model of the modified CESR-c wiggler in lattices, clockwise from top-left: BRU, DAS, MCH, and OCS. Shown are results for five random error seeds.

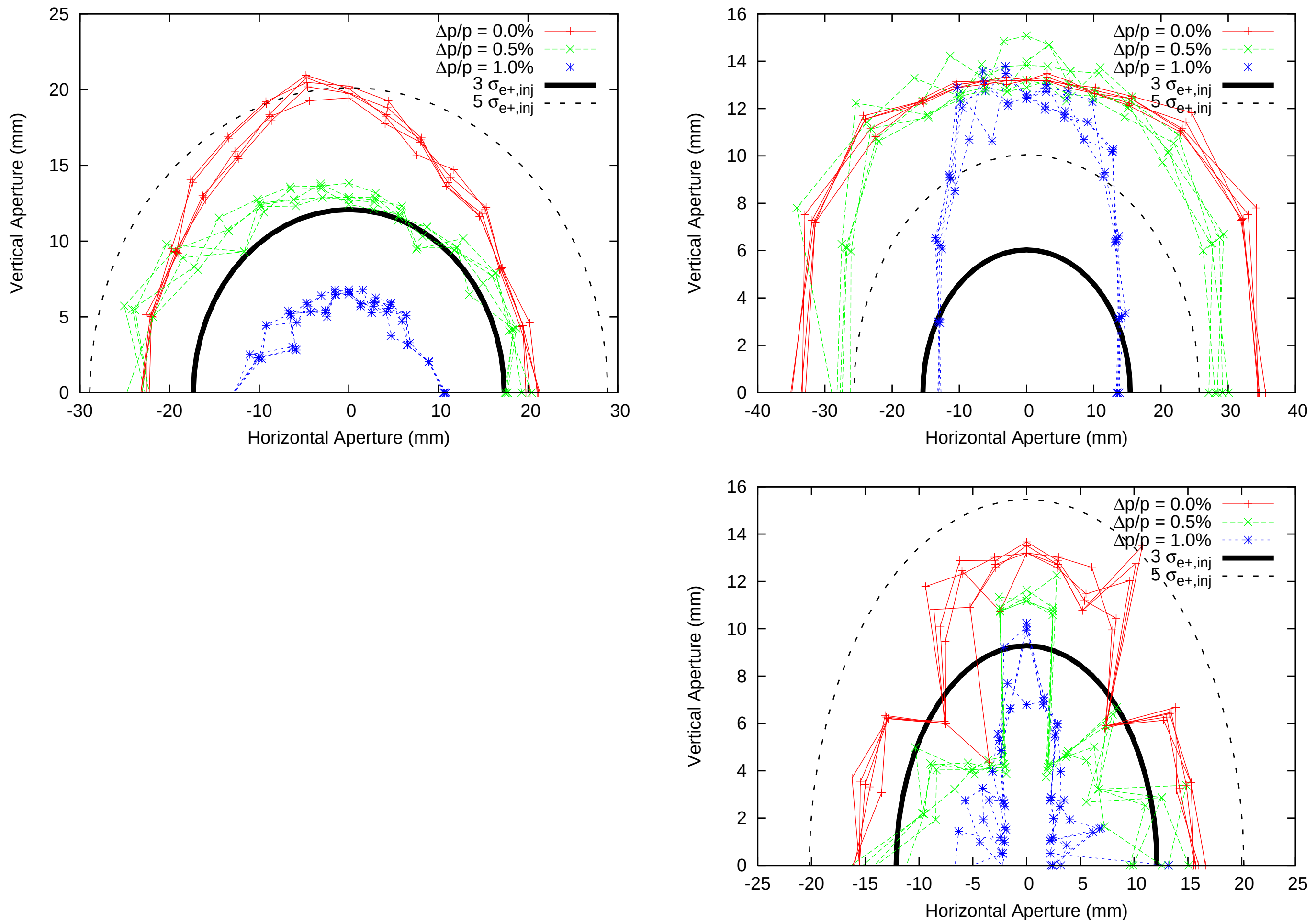

Figure B.3b: Dynamic aperture, with multipole field errors, results for the full nonlinear wiggler model of the modified CESR-c wiggler in lattices, clockwise from top-left: OTW, PPA, and TESLA. Shown are results for five random error seeds.

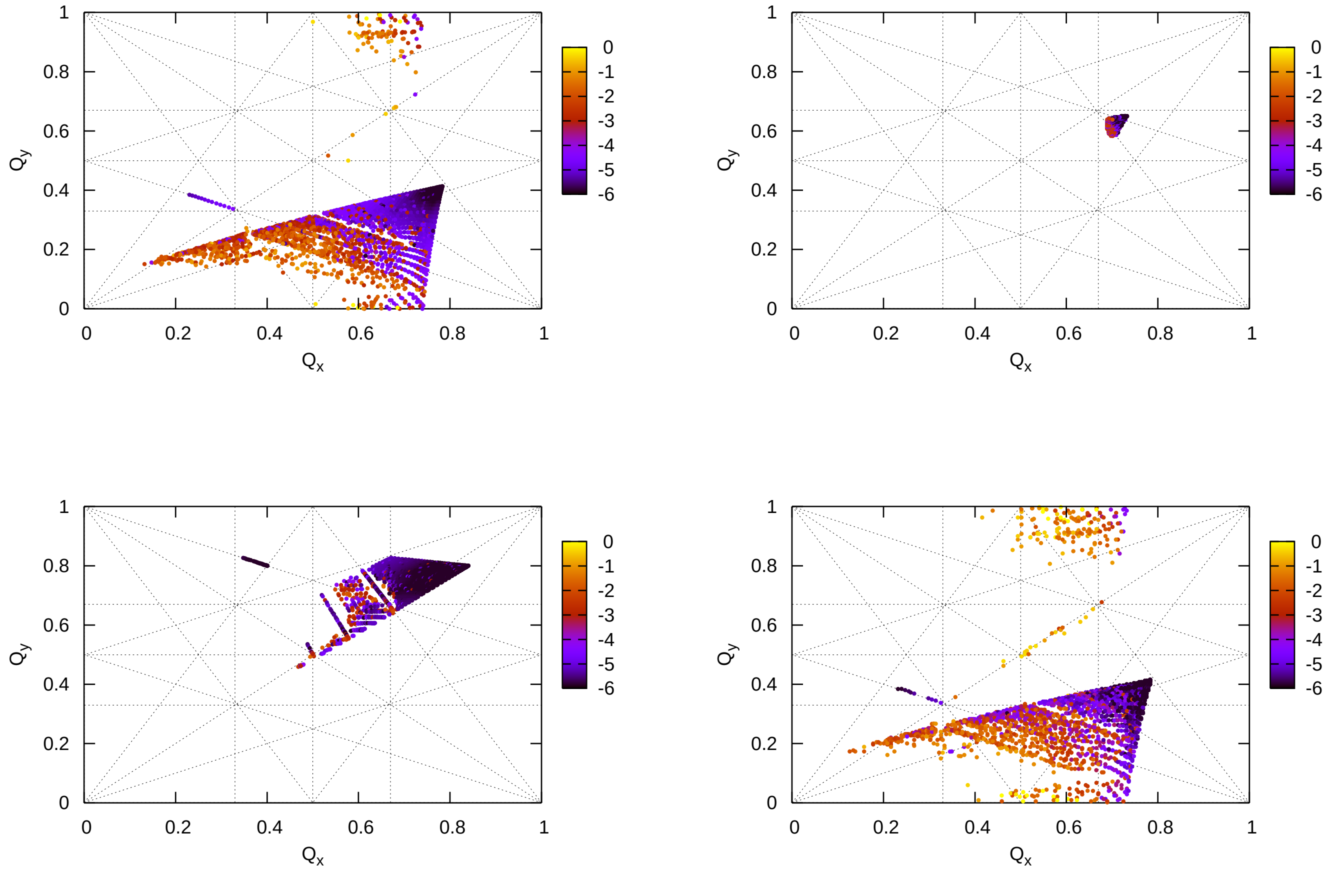

Figure B.4a: Frequency map analysis results for the linear wiggler model of the modified CESR-c wiggler in lattices, clockwise from top-left: BRU, DAS, MCH, and OCS.

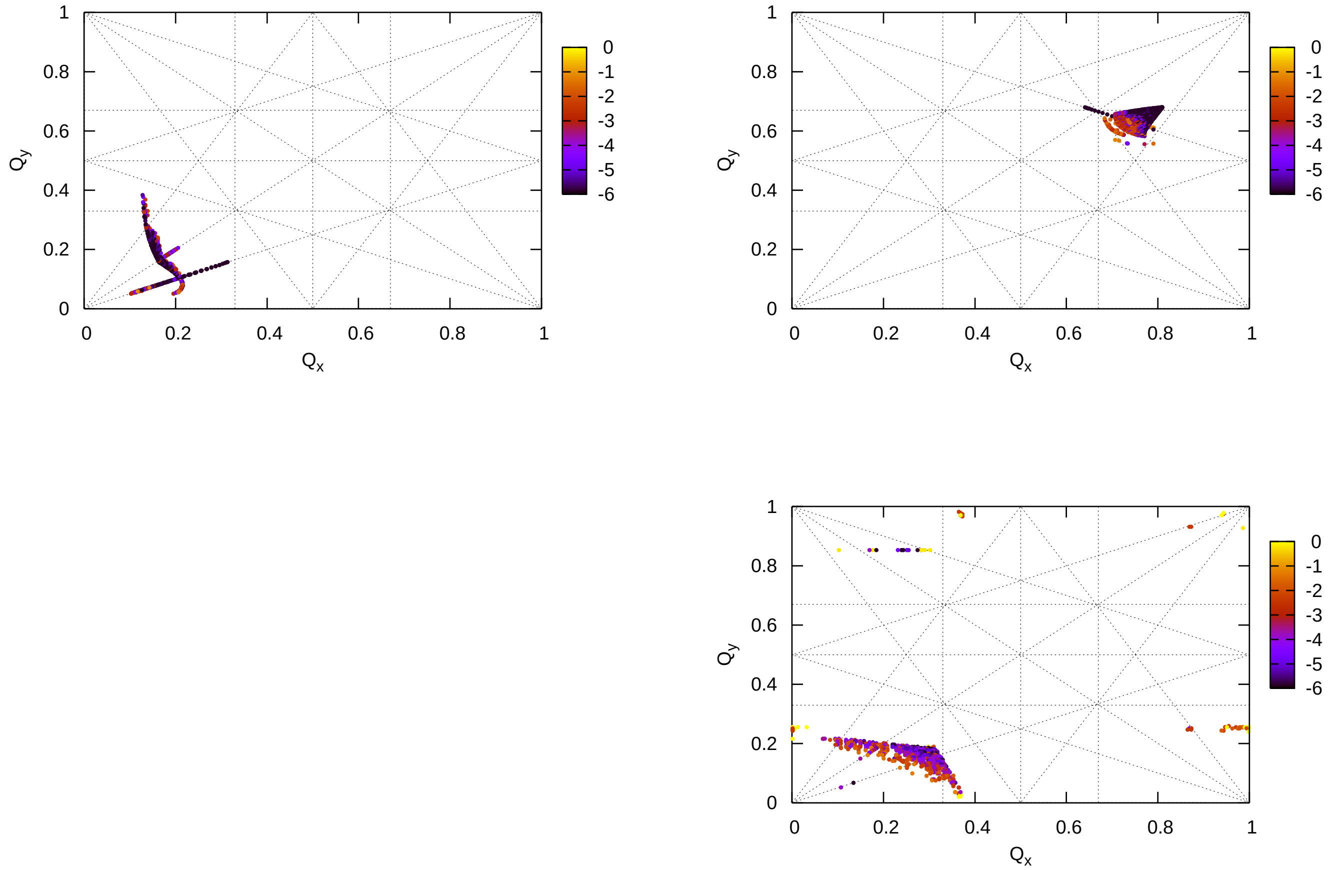

Figure B.4b: Frequency map analysis results for the linear wiggler model of the modified CESR-c wiggler in lattices, clockwise from top-left: OTW, PPA, and TESLA.

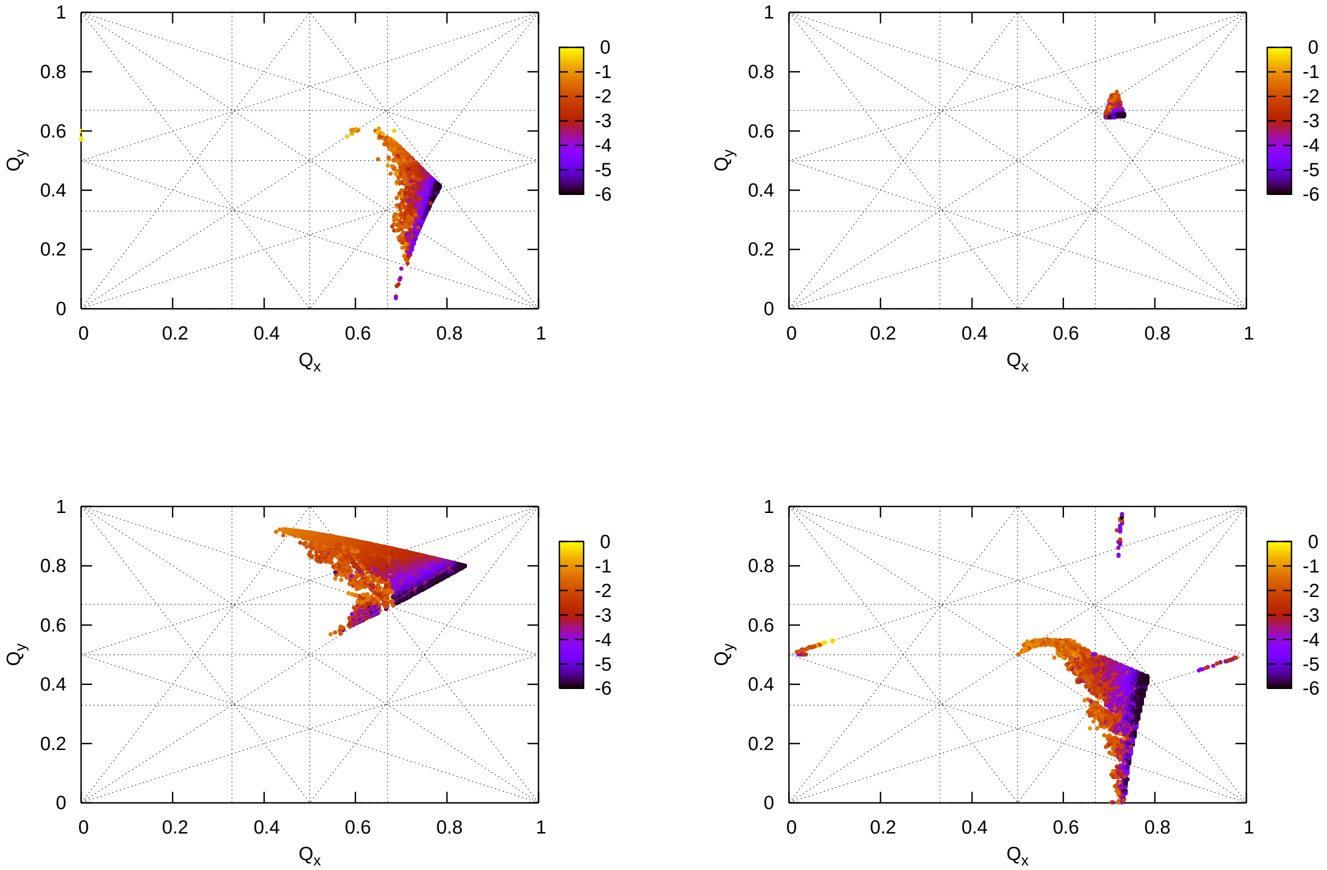

Figure B.5a: Frequency map analysis results for the full nonlinear wiggler model of the modified CESR-c wiggler in lattices, clockwise from top-left: BRU, DAS, MCH, and OCS.

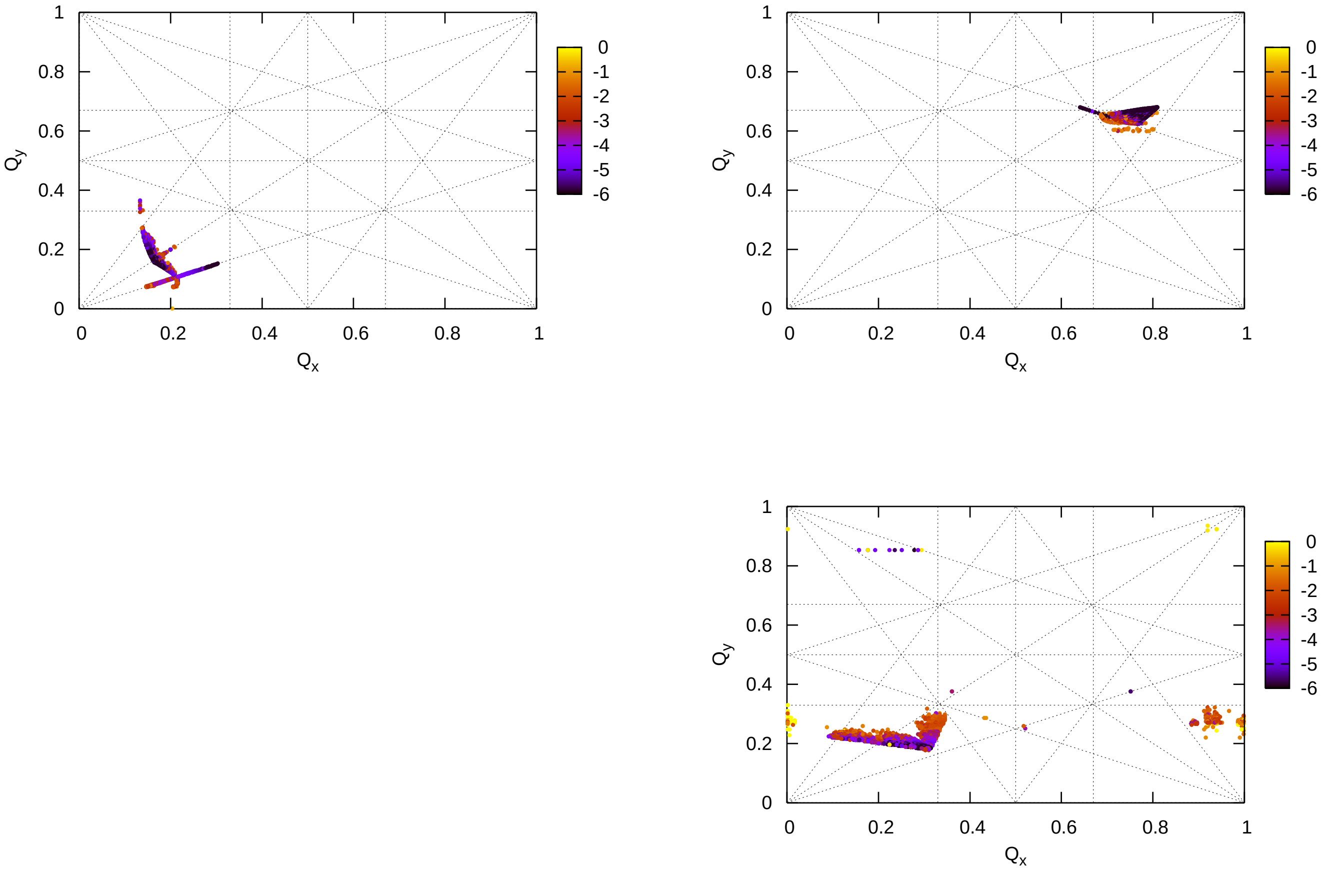

Figure B.5b: Frequency map analysis results for the full nonlinear wiggler model of the modified CESR-c wiggler in lattices, clockwise from top-left: OTW, PPA, and TESLA.

BIBLIOGRAPHY

[1] K. Wille. *The Physics of Particle Accelerators*. Oxford University Press, Oxford, 2000.

[2] N. Walker, A. Wolski, P. Tenenbaum, and A. Seryi. "Physics and Technology of Linear Collider Facilities". Presented as course lecture at US Particle Accelerator School, Santa Barbara, CA, June 2003.

[3] A. Chao and M. Tigner. *Handbook of Accelerator Physics and Engineering*. World Scientific Publishing, Singapore, 1999.

[4] "Report of the ILCSC Task Force for Establishment of the International Linear Collider Global Design Initiative". Technical report, International Linear Collider Steering Committee, March 2004.

[5] "The International Linear Collider Global Design Effort Baseline Configuration Document". `http://www.linearcollider.org/wiki/doku.php?id=bcd:bcd_home`, December 2005.

[6] "Parameters for the Linear Collider". Technical report, International Linear Collider Steering Committee, Parameters Subcommittee, September 2003.

[7] R. Erickson et al. "The SLC Design Handbook". Technical Report 714, SLAC, 1984.

[8] "Understanding Matter, Energy, Space and Time: The Case for the e^+e^- Linear Collider". `http://physics.uoregon.edu/~lc/wwstudy/lc_consensus.pdf`, April 2003.

[9] G. Hoffstaetter. "Introduction to Accelerator Physics and Technology". Presented as course lecture at Cornell University, Ithaca, NY, August 2003.

[10] "TESLA Technical Design Report". Technical Report 23, TESLA, 2001.

[11] T.O. Raubenheimer et al. "Zeroth order design report for the Next Linear Collider". Technical Report 5424, LBNL, 1996.

[12] A. Wolski, J. Gao, and S. Guidducci. "Configuration Studies and Recommendations for the ILC Damping Rings". Technical Report 59449, LBNL, 2006.

[13] A. Wolski, J. Gao, and S. Guiducci. "Choosing a Baseline Configuration for the ILC Damping Rings". In *Proceedings of European Particle Accelerator Conference 2006*, Edinburgh, Scotland, June 2006.

[14] P. Kuske, R. Görgen, and J. Kuszynski. "Investigation of Nonlinear Beam Dynamics with Apple II-Type Undulators at Bessy II". In *Proceedings of Particle Accelerator Conference 2001*, Chicago, IL, June 2001.

[15] C. Milardi et al. "Effects of Nonlinear Terms in the Wiggler Magnets at DAΦNE". In *Proceedings of Particle Accelerator Conference 2001*, Chicago, IL, June 2001.

[16] A. Wolski, J. Nelson, M.C. Ross, and M.D. Woodley. "Initial Studies of Nonlinear Dynamics in the KEK-ATF Wigglers". Technical Report 57047, LBNL, 2005.

[17] H. Wiedemann. *Particle Accelerator Physics II*. Springer-Verlag, Berlin, 1995.

[18] J. Corbett and Y. Nosochkov. "Effect of Insertion Devices in SPEAR-3". In *Proceedings of Particle Accelerator Conference 1999*, New York, NY, March 1999.

[19] J. Rogers. "A Damping Ring Primer". Presented at American Linear Collider Workshop at SLAC, Palo Alto, CA, January 2004.

[20] A. Temnykh. "Wiggler Optimization for Emittance Control: Experience at CESR-c". In *Proceedings of Workshop on Wiggler Optimization for Emittance Control*, Frascati, Italy, February 2005.

[21] D. Sagan. "The Bmad Reference Manual". `http://www.lepp.cornell.edu/~dcs/bmad`.

[22] D. Sagan and D. Rubin. "CESR Lattice Design". In *Proceedings of Particle Accelerator Conference 2001*, Chicago, IL, May 2001.

[23] D. Sagan, J.A. Crittenden, D. Rubin, and E. Forest. "A Magnetic Field Model for Wigglers and Undulators". In *Proceedings of Particle Accelerator Conference 2003*, Portland, OR, May 2003.

[24] Vector Fields. OPERA-3d. `http://www.vectorfields.com`.

[25] European Synchrotron Radiation Facility. Radia Manual. `http://www.esrf.fr/Accelerators/Groups/InsertionDevices/Software/Radia/`.

[26] K. Halbach. "Physical and Optical Properties of Rare Earth Cobalt Magnets". *Nuclear Instruments and Methods in Physics Research Section A*, 187:109–177, 1981.

[27] J. Laskar. "Frequency Map Analysis and Particle Accelerators". In *Proceedings of Particle Accelerator Conference 2003*, Portland, OR, May 2003.

[28] M. Tischer et al. "Damping Wigglers for the PETRA III Light Source". In *Proceedings of Particle Accelerator Conference 2005*, Knoxville, TN, May 2005.

[29] R.H.A. Farias et al. “Commissioning of the LNLS 2 T Hybrid Wiggler”. In *Proceedings of Particle Accelerator Conference 2005*, Knoxville, TN, May 2005.

[30] M. Tischer, J. Pfluger, and W. Decking. “A Permanent Magnet Wiggler Design for the TESLA Damping Ring”. Technical Report 20, TESLA, 2000.

[31] A. Mikhailichenko. “Optimized Wiggler Magnet for CESR”. In *Proceedings of Particle Accelerator Conference 2001*, Chicago, IL, June 2001.

[32] R. Brinkmann, J. Pflueger, V. Shiltsev, N. Vinokurov, and P. Volby. “Wiggler Options for TESLA Damping Ring”. Technical Report 24, TESLA, 1995.

[33] W. Decking. “Investigation of the Nonlinear Effects of Wiggler and Undulator Fields on the Beam Dynamics of Particle Storage Rings in the Case of DORIS III”. Technical Report 232, DESY, 1995.

[34] M. Tischer. “TESLA Damping Wiggler - Improved Field Roll-Off”. `http://www.desy.de/~wdecking/dog/pmdampwiggler/dampingwiggler_fldrolloff.pdf`, January 2002.

[35] M. Tischer. Private communication, May 2005.

[36] Y. Cai. “Dynamic Aperture in Damping Rings with Realistic Wigglers”. In *Proceedings of Workshop on Wiggler Optimization for Emittance Control*, Frascati, Italy, February 2005.

[37] M. Venturini. “Modeling of Wiggler Fields for Tracking”. In *Proceedings of Workshop on Wiggler Optimization for Emittance Control*, Frascati, Italy, February 2005.

[38] D. Rice et al. “Parameters for Low Energy Operation of CESR”. In *Proceedings of Particle Accelerator Conference 2001*, Chicago, IL, June 2001.

[39] D. Rice et al. “Production and Testing Considerations for CESR-c Wiggler Magnets”. In *Proceedings of Particle Accelerator Conference 2003*, Portland, OR, May 2003.

[40] Y. He et al. “Design and Operation of the Cryostat for the CESR-c Superconducting Wiggler Magnets”. In *Proceedings of Particle Accelerator Conference 2003*, Portland, OR, May 2003.

[41] J.A. Crittenden, A. Mikhailichenko, and A. Temnykh. “Design Considerations for the CESR-c Wiggler Magnets”. In *Proceedings of Particle Accelerator Conference 2003*, Portland, OR, May 2003.

[42] J.A. Crittenden, A. Mikhailichenko, E. Smith, K. Smolenski, and A. Temnykh. "Field Modeling for the CESR-c Superconducting Wiggler Magnets". In *Proceedings of Particle Accelerator Conference 2005*, Knoxville, TN, May 2005.

[43] A. Temnykh, J.A. Crittenden, D. Rice, and D. Rubin. "Beam Based Characterization of a New 7-Pole Superconducting Wiggler at CESR". In *Proceedings of Particle Accelerator Conference 2003*, Portland, OR, May 2003.

[44] A. Temnykh. "CESR-c: Performance of a Wiggler-Dominated Storage Ring". In *Proceedings of Particle Accelerator Conference 2005*, Knoxville, TN, May 2005.

[45] J. Urban and G. Dugan. "CESR-c Wiggler Studies in the Context of the International Linear Collider Damping Rings". In *Proceedings of Particle Accelerator Conference 2005*, Knoxville, TN, May 2005.

[46] I. Reichel and A. Wolski. "Tracking Studies to Determine the Required Wiggler Aperture for the ILC Damping Rings". In *Proceedings of European Particle Accelerator Conference 2006*, Edinburgh, Scotland, June 2006.

[47] M. Pivi et al. "Simulation of the Electron Cloud for Various Configurations of a Damping Ring for the ILC". In *Proceedings of European Particle Accelerator Conference 2006*, Edinburgh, Scotland, June 2006.

[48] M. Palmer. "ILC Damping Ring Wiggler Evaluation". Presented at ILC Damping Rings Meeting at CERN, Geneva, Switzerland, November 2005.

[49] A. Xiao and L. Emery. OCS lattice version 2.0. `https://wiki.lepp.cornell.edu/ilc/pub/Public/DampingRings/WebHome/ocs2.xsif`, March 2006.

[50] A. Xiao and L. Emery. OCS lattice version 6.0. `https://wiki.lepp.cornell.edu/ilc/pub/Public/DampingRings/WebHome/OCS6.xsif`, June 2006.

[51] "US Linear Collider Technology Options Study". Technical report, International Linear Collider Steering Committee, Accelerator Subcommittee, March 2004.

[52] E. Smith. Private communication, November 2006.

[53] M. Venturini. "Benchmarking of Codes/Methods Used to Model Wiggler Nonlinearities: A Short Summary". Presented at ILC Damping Rings Meeting at CERN, Geneva, Switzerland, November 2005.

[54] M. Berz and K. Makino. COSY. `http://www.cosyinfinity.org`.

[55] A. Wolski. “ILC Damping Rings”. Presented as a LEPP Accelerator Physics Brown Bag Seminar, November 2004.

[56] E. Forest. *Beam Dynamics: A New Attitude and Framework*. Harwood Academic Publishers, Amsterdam, 1998.